The copyright of this thesis vests in the author. No quotation from it or information derived from it is to be published without full acknowledgement of the source. The thesis is to be used for private study or non-commercial research purposes only.

Published by the University of Cape Town (UCT) in terms of the non-exclusive license granted to UCT by the author.

University of Cape Town

Microstructure and Residual Stress in Hydrogenated Amorphous Silicon (a-Si:H) Layers

BY
Fhatuwani Lawrence Ramukosi

University of Cape Town

Thesis submitted in fulfillment of the requirements for the degree of Master of Science in Physics

Department of Physics, University of Cape Town

June 2006

ABSTRACT

Hydrogenated amorphous silicon (*a*-Si:H) is known to be highly disordered. The disorder introduces a high amount of defects in the network, such as bond length and angle deviation, non-coordinated bonds or voids. In this work the microstructural characterization and a new approach for strain determination in hydrogenated amorphous silicon in the layers is determined by synchrotron diffraction. The a-Si:H layers were deposited by hotwire chemical vapour deposition (HW-CVD) on a glass substrate at a growth temperature of 300 °C and 500 °C, respectively. The microstructural state from the diffraction phase has been experimentally determined using the pair correlation function, calculated using Fourier transformation of the scattered intensity. Indication of the residual stress in the layers was obtained using the conventional $sin^2\psi$ method, normally used and especially developed for polycrystalline materials, but here applied to an amorphous structure. It is found that residual stress and microstructure of the layers are correlated. The pair distribution function (PDF) of the short range order reveals a significant shift in the nearest neighbour distance of Si-Si pairs leading to bond strain in the layers. The PDF reveals that the short-range bonding of a-Si:H is tetrahedral but it does not give much information about the intermediate region which relates to the structural topology. We observed a deviation in the nearest-neighbour and the second nearest-neighbour separation, independent of the growth temperature. The observed strain curves deviate from the linear prediction of the conventional $\sin^2\psi$ method. The layers were found to be generally under compressive stress, with strong gradients dominant in the interface region of the sample, and the resulting stress is highly dependent on the details of the deposition process.

University of Cape Town

ACKNOWLEDGEMENTS

First and the foremost, I would like to gratefully thank the almighty God for giving me continuous strength and courage during the course of this project.

A grateful acknowledgement and many thanks to my two supervisors, Prof. DT Britton and Prof. M Härting, who read my numerous revisions and helped, make some sense out of this thesis. There was a time were I got so frustrated with my work but they always assure me that there was nothing to worry about. Your leadership has taken me to a new level, and I have appreciated all your personal and professional advice over 3 years I spend with the group.

I wish to thank E. Minani, M Ukpong, G. Goro, S. Nsengiyumva and K. Hansingo for their useful and fruitful discussions. I cannot say enough wonderful things about this group, about all the people I have encountered in my years of service with the group, and all the other stuff members at the University of Cape Town.

I am also indebted to National Research Foundation (NRF) and the University of Cape Town Council bursary; this project would not have been possible without their financial support. And finally, many thanks to my parents, and numerous friends who endured this long process with me, always offering support and love.

University of Cape Town

TABLE OF CONTENTS

Abstract....................i

Acknowledgement....................ii

1 Introduction....................1

2 The Structure of Amorphous Materials....................5
 2.1 Amorphous Networks....................7
 2.2 a-Si:H compared to a perfect CRN....................10
 2.3 Statistical Description of Amorphous Structure....................11

3 Strain and Stress in Solids....................14
 3.1 Residual Stress....................19
 3.2 Residual Stress in Layered System....................20
 3.3 Stress in Hydrogenated Amorphous Silicon (a-Si:H)....................21

4 Techniques Used To Determine the Microstructure and Residual Stress....................23
 4.1 Diffraction Techniques....................23
 4.2 Basic Diffraction Theory....................24
 4.3 Diffraction from Amorphous Material....................26
 4.4 Calculation of Radial Distribution Function....................27
 4.5 Determination of Strain and Stress from X-Ray Diffraction....................31
 4.6 Effects of Strain in Diffraction Patterns....................33
 4.7 Determination of Strain from Diffraction....................35
 4.8 Strain-Stress Relation....................36
 4.9 Residual Stress Calculation....................41

5 Experimental Details....................42
 5.1 Sample Preparation....................42
 5.2 Diffraction Measurement....................42
 5.3 Background Subtraction....................44
 5.4 Peak diffraction....................47

6 Results and Discussion....................51
 6.1 Diffraction Patterns in q space....................51
 6.2 Diffraction in real-space....................55
 6.3 The variation of strain....................60
  6.3.1 Strain determine from 2Θ diffraction patterns.................... 62
  6.3.2 Strain determined from pair correlation function....................65
  6.3.3 Determination of residual stress....................67

7 Conclusion....................74

References....................77
Appendix....................82

University of Cape Town

LIST FIGURES

Figure 2. 1: Three-dimensional model illustrating the parameters used for describing the structural order of tetrahedral amorphous semiconductors (p6)

Figure 2. 2: Continuous random network structure of amorphous silicon. The magnification shows a small portion of silicon atoms bonded to form regular tetrahedron (p8)

Figure 2.3: Two-dimensional projection of a portion a continuous random network showing coordination shells (fourth bond out of plane of drawing) (p8)

Figure 2. 4: Schematic illustration showing first r_1 and second nearest-neighbor bond lengths r_2, and bond angle α, in radial distribution function (RDF) (p12)

Figure 3.1: Illustrate the definition of the axial and shear strains (p14)

Figure 3.2: Stress on a cubic volume in static equilibrium. Each surface has two types of forces, normal and shear (p17)

Figure 4.1: Electron diffraction patterns showing (a) a crystalline form and (b) amorphous form (p26)

Figure 4.2: Radial Distribution Function of a-Si:H in real space (plotted using RAD) (p31)

Figure 4.3. Illustration of uniform strain and non-uniform strain (p33)

Figure 4.4: Schematic representation of the laboratory coordinate system and the sample coordinate system for strain and stress components and Euler angles (ψ,ϕ) (p35)

Figure 5.1: Overview of the measurement procedure (p43)

Figure 5.2: Synchrotron diffraction patterns for an uncoated glass substrate and for an a-Si:H layer deposited on the glass substrate (p44)

Figure 5.3: Illustration of the background subtraction. An integrated pattern of X-ray scattering for Hydrogenated amorphous silicon is plotted after background subtraction (p46)

Figure 5.4: Gaussian fitting of the amorphous diffraction patterns (p48)

Figure 6.1: Diffraction pattern from layers deposited at 300 °C and 500 °C measured at $\psi = 0$ and $\phi = 0$ (p52)

University of Cape Town

Figure 6.2: Diffraction pattern showing the first two maxima in a-Si:H layer. First peak corresponding to the height of the $Si\text{-}Si_4$ and the second peak correspond to tetrahedron edge lengths of the $Si\text{-}Si_4$ tetrahedron, respectively (p53)

Figure 6.3: The diffraction peak shift with ψ tilting relative to (111) and (220) in a-Si:H for two samples grown at (a) 300°C and (b) 500 °C respectively. The displacement of the peaks as indicated by arrows in both samples is due to strain effect on layers (p54).

Figure 6.4: Pair distribution function for a-Si:H layer (a) samples grown at 300 °C and (b) samples grown at 500 °C (p56)

Figure 6.5: Comparison of the pair distribution function for a-Si:H layer deposited at temperature of 300 °C and 500 °C (p57)

Figure 6.6: The variation of the nearest-neighbour and second nearest neighbour separations for a-Si:H grown at 500° C growth at $\phi = 0$ for tilts of $\psi = 0°$, 20°, 40°. The pattern exhibits a peak shift in the height and the width of the peak as indicated by the arrows (p59)

Figure 6.7: The diffraction pattern after smoothing with a 7-point smoothed Savitzky-Golay algorithm. The bold red line represents a fitted Gaussian curve for peak position, and FWHM estimation. (p61)

Figure 6.8: Variation of the stain with $sin^2\psi$ for the a-Si:H layer deposited at 300 °C determined from diffraction pattern: (a) first diffraction peak corresponding to the height of the $Si\text{-}Si_4$ tetrahedron, equivalent to the *(111)* reflection in c-Si (b) the second diffraction peak, equivalent to the *(220)* reflection in c-Si, corresponding to the length of side of the $Si\text{-}Si_4$ tetrahedron (p63)

Figure 6.9: Variation of the linear $sin^2\psi$ obtain in a-Si:H layer at 500°C determined from diffraction pattern (a) first diffraction peak corresponding to the height of the $Si\text{-}Si_4$ tetrahedron, is equivalent to the *(111)* reflection in c-Si (b) the second diffraction peak, is equivalent to the *(220)* reflection in c-Si, and corresponding to the length of side of the $Si\text{-}Si_4$ (p64)

Figure 6.10: Variation of bond strain determined from nearest neighbour separation in the pair correlation function: (a) a-Si:H layer deposited at 300 °C and (b) a-Si:H layer deposited at 500°C (p66)

Figure 6.11: Linear fit of strain as a function of $sin^2\psi$ for sample 500°C (p68)

University of Cape Town

LIST OF TABLES

Table 6.1: Interatomic spacing r_1 and r_2 *in* $\AA$, and the bond angle for two samples at different ψ tilts and $\phi = 0$ (p58)

Table 6.2: Peak position parameters and information for the variation of strain from diffraction as a function of 2Θ in a-Si:H layer at 300 °C and 500°C (p62)

Table 6.3: Residual stress in *GPa* obtained from a-Si:H layer for samples deposited at 300 °C and 500 °C using direct diffraction peak shifts (p69)

Table 6.4: Residual stress in *GPa* obtained from a-Si:H layer for samples deposited at 300 °C and 500 °C using direct PDF peak shifts (p70)

Table 6.5: Biaxial stress state in *GPa* obtained from a-Si:H layer for samples deposited at 300 °C and 500 °C obtained using 2Θ data (p72)

Table 6.6: Biaxial stress state in *GPa* obtained from a-Si:H layer for samples grown at 300 °C and 500 °C obtained using pair correlation function (p72)

University of Cape Town

1 INTRODUCTION

The subject of this thesis is the study of the class of materials known as amorphous silicon. The basic property of amorphous materials is that they do not possess any long-range translational order. This means that an amorphous material does not have a regular or periodic arrangement of its component atoms, but there exists an element of randomness in the atomic positions. Of particular interest in this study are the structural characteristics exhibited by hydrogenated amorphous silicon (a-Si:H) and the length of scale over which order persists. Such interest is motivated by the widespread application of a-Si:H in microelectronic devices and thin film electronics [1-4]. Among these applications solar cells, large-area flat-panel displays, thin-film transistors, optical scanners, photosensors and electrophotographics are the areas where hydrogenated amorphous silicon may have a leading role. Many of the reasons for its common use in these applications are due to the properties generated by its amorphous structure as discussed in this work. One unique property of a-Si:H thin films is the high light absorption: it is 40 times higher than that of crystalline silicon (c-Si) [5]. In addition good quality material can even be achieved by deposition at low temperature, which allows the use of a low cost substrate [5]. These in turn provide the opportunity of cost efficiency device production.

Hydrogenated amorphous silicon can be produced by a variety of methods [6] such as hotwire chemical vapour deposition (HW-CVD), sputtering, glow discharge plasma (CVD), and plasma enhanced chemical vapour deposition (PECVD) in a form of a thin film. In all cases the substrate plays an important role in the thin film deposition process. It may strongly influence the properties and structure of the film deposited on [7]. Thin films

University of Cape Town

adherent to a substrate are in general in a state of tensile or compressive residual stress, which may also affect their physical properties [8]. There are two basic factors that define the kind of stress present in the layer, and the magnitude of residual stress in a-Si:H. Firstly, the difference in thermal expansion of substrate and the layer of the material, and secondly both thermal expansion of substrate and the layer are in a relationship determined by the growth mechanism [9]. In fact, residual stresses directly influence almost all properties of thin films, and thus are of great importance with respect to their usage [8]. For a-Si:H it has been supposed [10, 11] that the hydrogen incorporation into the silicon matrix induces compressive stress in the films, although no correlation between the total hydrogen concentration and the value of compressive stress has been established. However, it has been demonstrated [12] that the configuration of hydrogen bonding to silicon atoms plays an essential role. Hydrogen atoms in the monohydride configuration (Si-H) have a positive correlation with the compressive stress, whereas those in the dihydride configuration (Si-H_2) have the opposite correlation [13]. Nevertheless, hydrogen is often dismissed as a secondary or minor cause of stress in a-Si:H, and structural inhomogeneities are believed to play the dominant role in determining the observed stress [14]. However, the nature of intrinsic stress in hydrogenated amorphous silicon (a-Si:H) in thin films is to date elusive [15]. In order to understand such effects, or to establish reliable relationships, between the formation parameters and the characteristic properties of amorphous silicon layers, the analysis of the stress state in relation to the microstructure is absolutely necessary. One group of techniques that has generated considerable attention in the characterization of amorphous structure is diffraction methods [2, 6, 19]. Diffraction techniques have been used extensively to improve knowledge of local order in amorphous compounds [1-2, 19], and recently to study residual stress [15, 20].

University of Cape Town

One limitation on applications of a-Si:H is the presence of defects, which are influenced by mobile hydrogen [16]. The primary function of hydrogen in amorphous silicon is to passivate threefold-coordinated silicon sites or dangling bond defects, and thus reduce the density of gap-state defect levels [15]. However, since a-Si:H is grown at temperatures around 200°C and above, in technical applications to date, H diffuses during growth and affects the device quality [16, 17]. Also, light-induced degradation is influenced by hydrogen diffusion, and the formation of unterminated dangling bonds [18]. On the other hand, hydrogen incorporation is tightly controlled by the deposition process [18]. Therefore, an interesting aspect is the relationship between stress content in a-Si:H layer and the order of the amorphous structure and the hydrogen behavior.

In the framework of the above summary, the objective of this thesis therefore, is to provide a comprehensive insight into structural ordering and to characterize the residual strain/stress states in hydrogenated amorphous silicon introduced by the hotwire chemical vapour deposition techniques using synchrotron diffraction techniques. Furthermore, we need to acquire more knowledge, which might contribute directly to an improved manufacturing and design of the amorphous structures. The structural ordering in amorphous materials is theoretically, as well as experimentally, described by the radial distribution function (RDF), also known as the pair correlation function [1-2, 19, 21]. This function determines the probability of finding an atom at a distance r from any atom in the random network, and hence gives the average separations of the nearest and second nearest neighbors, and possibly the third nearest neighbors. The RDF is obtained by the Fourier transform of the scattering intensity [22, 23]. The strain and stress investigation is also based on diffraction techniques,

University of Cape Town

and relies on the conventional $\sin^2\psi$ method [8, 15, 20]. A detailed description of the radial distribution function (RDF) and strain and stress determination is covered in the subsequent chapters.

University of Cape Town

2 THE STRUCTURE OF AMORPHOUS MATERIAL

The forces linking atoms in an amorphous material are, in general, the same as those in crystalline material [24]. Therefore, amorphous structure must also form an extended three-dimensional structure similar to those of crystals, but lacks the periodicity and symmetry of crystalline materials and consequently are disordered. The unit cell in this case can, therefore, be said to be infinite in size. However, since one can neither recognize a unit cell nor a translational symmetry within the amorphous structure, other means of describing the structure must be defined [1]. Consequently, the amorphous structure is often described in terms of the degree of ordering which can be observed using experimental techniques, and by characterizing the structural units responsible for the ordering. In our case, one of the most important variables is a geometrical parameter, which allows us to discuss the distribution of atoms as a function of their spatial distance from a specified point. In SiO_2 glass for example, the basic structural building block is the same as that of crystalline silicates, the SiO_4 tetrahedron [2, 23]. A similar Si-Si_4 tetrahedral unit can be ascribed to amorphous silicon [24]. In fact, the structural order of amorphous solids has a definite hierarchy [1, 2], where the order is described increasingly as follows: Short-range order (SRO); intermediate-range (IRO); and long-range order (LRO). The definition of each of these types of order is somewhat arbitrary with different authors using different criteria to define them. Wright [27] defined four ranges of order: (I) the structural unit; (II) the interconnection of adjacent structural units; (III) the network topology (medium range order); (IV) long-range density fluctuations (long-range order). The parameters that define the first two ranges of order defined by Wright are often grouped under short-range order. However, subdivision of short-range order more clearly defines the boundary between the levels of ordering that differentiate a crystalline from

University of Cape Town

amorphous materials. Fig. 2.1 shows a three-dimensional model, which illustrates the geometrical parameters, which play a key role in describing the structural order of tetrahedral amorphous semiconductors.

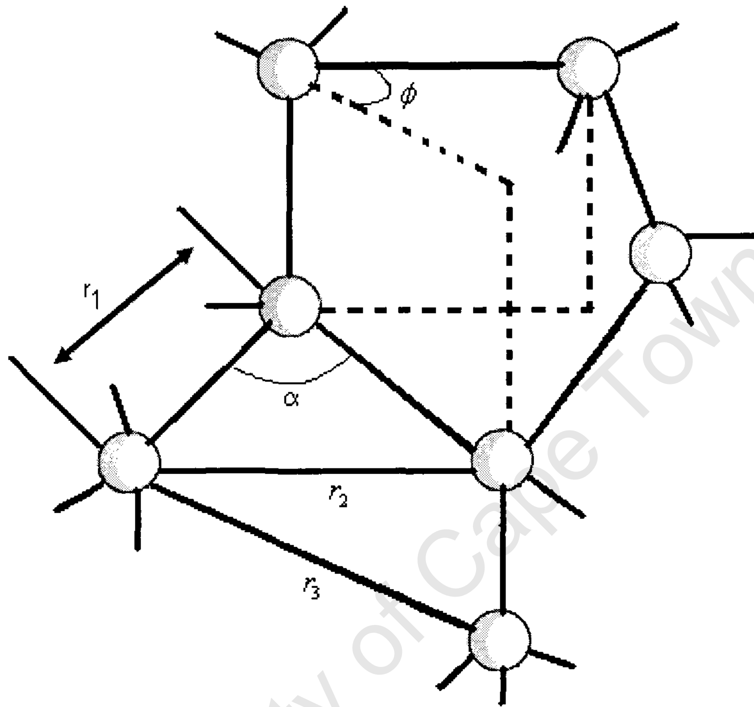

Fig. 2.1 Three-dimensional model illustrating the parameters used for describing the structural order of tetrahedral amorphous semiconductors (drawn from [1])

University of Cape Town

This model contains six geometrical parameters: the inter-atomic distance for nearest neighbors (bond length) r_1, the bond angle α (α = 109.28° for the sp^3 hybrid orbital), the inter-atomic distance for second nearest neighbors r_2, the dihedral angle ϕ (this is refers to the angle that is formed whenever two "planes" meet), the inter-atomic distance for third-nearest neighbors r_3 , and the ring structure 'parameter' (ring statistics for five-, six-, and seven-member rings). The statistical distributions of r_1, and α (consequently, r_2 and the coordination numbers of the nearest neighbors are also included) are used to index the short-

range order, while the statistical distributions of ϕ , r_3 and the ring structure are used to index the intermediate range order [28, 29]. There have been a number of attempts to build up amorphous structures theoretically by using these parameters. It is not easy, however, to take the process in the reverse order, *i.e.* to determine the statistical distribution of the various parameters from experimental data. The most useful techniques include X-ray and neutron diffraction, extended X-ray absorption fine structure spectroscopies (EXAFS) and Raman scattering [1, 2, 19].

2.1 AMORPHOUS NETWORK

University of Cape Town

Generally, the local structure of amorphous solids can be classified in terms of [30-32]:

(a) a continuous random network (CRN) appropriate to the structure of the materials ;

(b) a random close packing appropriate to the structure of the simple metallic glasses; and

(c) a random coil model appropriate to polymeric organic glasses.

However, this section will primarily focus on the continuous random network (*i.e.* the material of type-a), where a-Si:H falls within. This model is typical for an ideal amorphous structure and is regarded as a giant molecule (see Fig. 2.2) in which perfect connectivity is maintained, with all the atoms retaining their normal valence [2]. Therefore the CRN can be considered to be a hypothetical idealized structure of an amorphous covalent solid, in the same sense that the single crystal is for the crystalline state. In both cases, the structures can be regarded as perfect because bonding defects such as dangling bonds or voids are excluded, but in crystals this are always points defects. It is widely believed that the bulk atomic structure of amorphous silicon (a-Si) is such that each or in average Si atom has four (see Fig. 2.2) others around it at the same distance (as in a crystal) forming a regular tetrahedron.

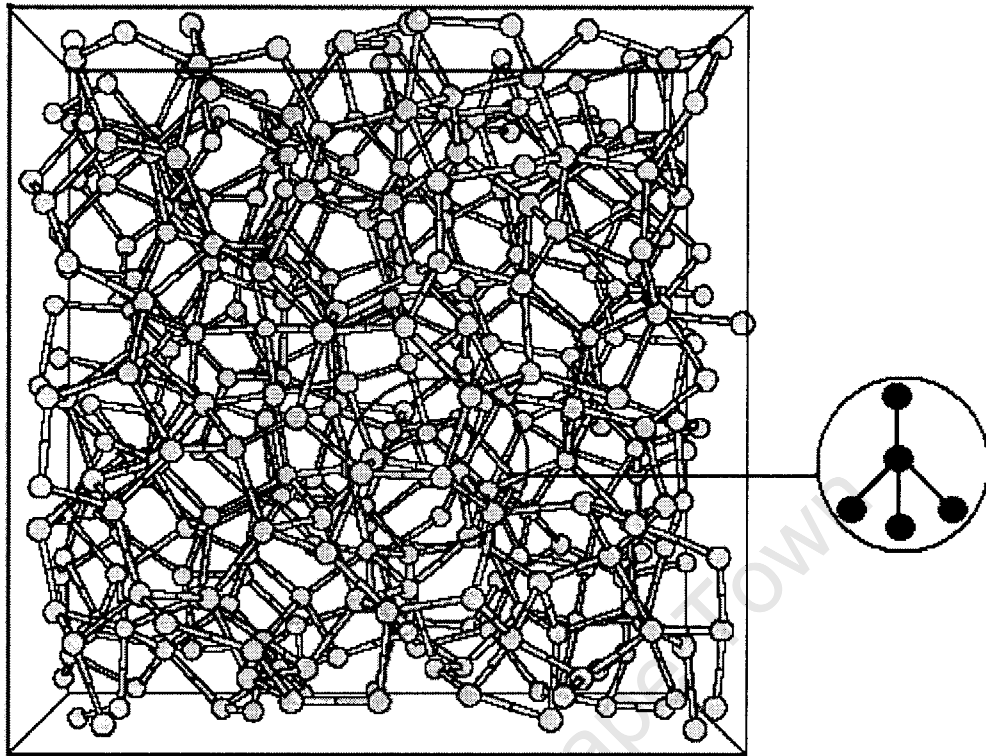

Fig. 2.2. Continuous random network structure of amorphous silicon. The magnification shows a small portion of silicon atoms bonded to form regular tetrahedron [34]

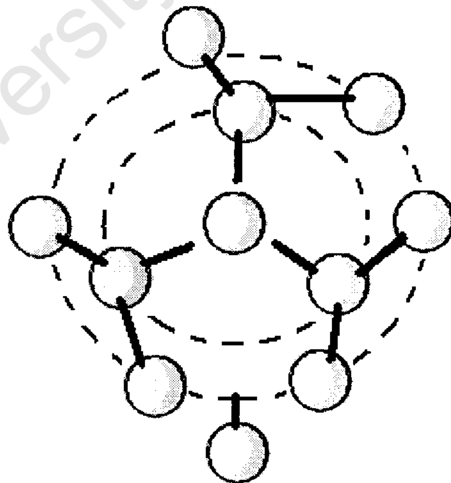

Fig. 2.3. Two-dimensional projection of a portion a continuous random network showing coordination shells (fourth bond out of plane of drawing)

University of Cape Town

Furthermore, each of these atoms in turn has three more neighbors, similarly arranged, giving rise to a well defined second shell of atoms, none of which is nearest neighbor to the central atom, and none of which are bonded to each other, as seen in Fig. 2.3. These structural features show that the resemblance of amorphous silicon to crystalline silicon ceases beyond the second shell. The continuous random network (CRN) was first proposed by Zachariasen [35], who applied it to oxide type glasses. Although the numbers of atoms associated with the nearest neighbors are the same, there is nevertheless a variation in the interbond angles that rapidly leads to a loss of local order and ultimately to the absence of long-range order [1, 2]. For a tetrahedrally bonded amorphous semiconductor, such as a-Si, a model built by Polk [1, 2, 19], demonstrated the possibility of building up an expanded *CRN* with the fourfold coordination without developing undue bond length strain, but allowing for a spread in bond angles ($\pm 10^{\circ}$), as shown in Fig. 2.2.

University of Cape Town

Polk [1] also showed that allowing a small spread in bond lengths ($\sim 1\%$) can lead to a smaller bond angle distortion ($\pm 7^{\circ}$), since a small increase in bond length distortion energy is compensated for by a larger decrease in bond angle distortion energy. A higher angular characteristic of tetrahedrally coordinated covalent material is the distribution of dihedral angles ϕ that describes the relative orientation of the adjacent tetrahedra. In the CRN model it was found that there is a continuous distribution of dihedral angles [34]. As can be seen in Fig. 2.1, the structure also possesses a substantial number of 5-, 6- and 7-membered rings. One additional property of this model, that was widely discussed, is the density of amorphous silicon. In the CRN model consisting of 440 atoms, introduced by Polk the highest density of amorphous silicon (a-Si) ρ_a is $0.97\rho_c$, where ρ_c is the density of crystalline silicon ($2.33 g/cm^3$) [33]. Subsequently, Polk, constructed another CRN model including 519 atoms,

using computer techniques, and obtained a density within 1% of that of c-Si. On the other hand, Brodsky *et al* [36] reported data for the systematic measurement of ρ_a and the electron spin resonance (ESR) density, N_S, showing lower concentrations of dangling bonds, with ρ_a as high as 0.97 ρ_c. In this context, the absence of the dangling bonds means the elimination of voids, since their presence within a-Si corresponds to the formation of dangling bonds within the material and point defects in c-Si.

2.2 a-Si:H COMPARED TO A PERFECT CRN

University of Cape Town

One of the enduring concepts of the network structure of a-Si:H is that each atom in the network tends to satisfy its local bonding requirement [37]. Atomic hydrogen in the network forms strong bonds to silicon, and the optimum structure is one, which minimizes the hydrogen that is not strongly bonded to silicon. Thus, an ideal a-Si:H material is a random covalent network of Si-Si, and Si-H bonds, but with no dangling silicon bonds or interstitial hydrogen [38], and the bond angles and bond-length disorder in the network structure causes a distribution of Si-Si bonds, and possibly Si-H bond length. Despite its amorphous character, a-Si:H has an optical gap. It shows photoconductivity and a-Si:H can be doped by means of boron and phosphorus properties which are similar to those of crystalline semiconductors [39].

The density of amorphous silicon varies markedly, if it contains hydrogen, depending upon both the content and the state of the hydrogen. As the hydrogen content is increased in *CRN*, the amorphous silicon density ρ_a decreases but with no clear trend. This indicate that the density depends on a number of factors, such as the state of the hydrogen within the films, the

presence of the voids of varying size, and the strain in the films. Samples of a-Si:H with densities higher than 90 % of that of crystalline silicon ($\rho_a > 0.9\rho_c$) are obtained only when prepared at a substrate temperature higher than 200 °C. The highest value ever achieved is $\rho_a = 0.97 - 0.98\rho_c$.The amorphous character of the material leads to open network structures, in which voids and unterminated bonds are present. Typical defect densities of high quality a-Si:H material are 10^{15}–10^{16} cm^{-3} [40]. In contrast, in a pure a-Si produced *e.g.* by sputtering, the defect density is as high as 10^{19}-10^{20} cm^{-3}. In a-Si:H the hydrogen is responsible for the lowering of the defect density by passivation of dangling bonds. This is essential for the material's opto-electronic properties, since the dangling bond can act as an efficient recombination center for electrons and holes. The CRN model demonstrated by Weaire *et al* [41] represents the calculated values of a-Si:H structure consisting of 397 silicon and 83 hydrogen atoms, constructed following the approach similar to Polk as described above. The model contains no dangling bonds within the structure except for those on the surface. The author pointed out that when a hydrogen atom is added to the structure, dangling bonds are readily formed around it [41], and thus attempting to make a CRN model without dangling bonds gives a network structure containing multiple hydrogen atoms which are closely packed. To date, several properties of a-Si:H have been studied and it is now well established that the amount of hydrogen required during preparation of a-Si:H depends on the type of material one is interested to obtain.

University of Cape Town

2.3 STATISTICAL DESCRIPTION OF AMORPHOUS STRUCTURE

While amorphous materials do not show the regular, periodic structure of crystals, they are by no means random CRN. For example, contrary to sharp peaks observed in diffraction

patterns of crystalline materials, amorphous solids yield diffuse diffraction patterns [19, 42]. These characteristic indicate the lack of long-range order in amorphous materials, and thus only short-range order hold. In many cases, the structure is governed by strict rules, especially on short length scales.

For example, amorphous silicon, as discussed above, consists mostly of four-fold coordinated silicon atoms, and the Si-Si bond length and the *Si-Si-Si* bond angle are close to the crystalline values of 2.35 Å and 109.47°, respectively. The presence of short-range order is best illustrated with the radial distribution function (RDF) [2, 19]. The RDF *is* the local number density of atoms at a distance *r* from a reference atom, averaged with respect to the choice of this atom [2]. Fig. 2.4 shows the RDF of amorphous silicon.

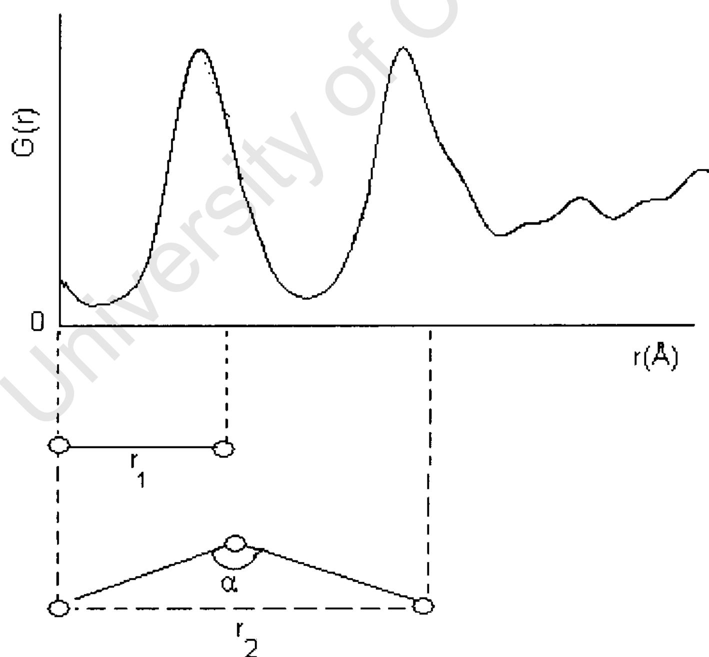

Fig. 2.4. Schematic illustration showing first r_1 and second nearest-neighbor bond lengths r_2, and bond angle α, in radial distribution function (RDF) - (drawn from [2]).

University of Cape Town

Its characteristic features are a number of peaks that become broader and less distinct with increasing separation. The position of the first peak is an estimate of the average first-neighbor distance r_1, the position of the second peak an estimate of the average second-nearest neighbor distance r_2 and so forth. Moreover, these estimates can also be used to estimate the mean Si-Si-Si bond angle:

$$\alpha = 2\arcsin\left(\frac{r_2}{2r_1}\right) \qquad 2.1$$

Also, from the width of the first- and second-neighbor peaks, the variation in the bond angle can be estimated under the assumption that there are no correlations between bond length variations in neighboring bonds. At larger distances, the RDF tends to a constant value, corresponding to the macroscopic density [2].

University of Cape Town

3 STRAIN AND STRESS IN SOLIDS

Under the action of applied forces solid bodies exhibit deformation to some extent, *i.e.* they change in shape or volume. When the body is deformed, every point in it is generally displaced [45]. Now let us consider the simplest case, in which translation and rotation of the body are excluded, and only its deformation is considered. Then the deformation can be quantified in terms of the displacement vector, ***u(x)***. To illustrate this, consider a region between positions x and $x+\Delta x$, in a body before and after deformation as shown by solid and broken lines respectively in Fig. 3.1(a).

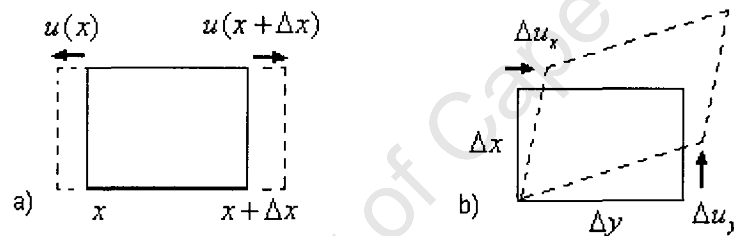

Fig. 3.1. (a) and (b) illustrate the definition of the axial and shear strains.

The vector ***u*** is called the displacement vector, and it can also be presented in its component form as $\boldsymbol{u} = (u_x, u_y, u_z)$. The displacement vector in any direction, say x, will vary from place to place in the material. In a general case we can define the strain ε_{xx} in terms of the partial derivatives of the displacement.

$$\varepsilon_{xx} = \frac{\partial u_x}{\partial x} \qquad 3.1$$

Similar equations will hold for the derivative of u_x with respect to y and z and for other components of the displacement (*i.e.* in total we will have nine components of the strain

University of Cape Town

tensors). Physically the strain is symmetrical; therefore mathematically it should have the form of symmetric second rank tensor:

$$\varepsilon_{ij} = \begin{pmatrix} \varepsilon_{xx} & \varepsilon_{xy} & \varepsilon_{xz} \\ \varepsilon_{xy} & \varepsilon_{yy} & \varepsilon_{yz} \\ \varepsilon_{xz} & \varepsilon_{yz} & \varepsilon_{zz} \end{pmatrix} \qquad 3.2$$

The definition of shear strains follows directly from the symmetric arguments of the strain tensor. For example the shear strain in *xy* components derived from Fig. 3.1(b) can be written in symmetric form as:

$$\varepsilon_{xy} = \frac{1}{2}\left(\frac{\partial u_x}{\partial y} + \frac{\partial u_y}{\partial x}\right) \qquad 3.3$$

Similarly the *yz* and *zx* components of the shear strain can readily be obtained using the same principle. This implies that the strain tensor has three independent variables; meaning that we can always find a coordinate system in which the strain tensor only has non-zero elements on its diagonal. This is the principal coordinate system.

In a body that is not deformed, all parts of the body are in mechanical equilibrium [45]. This implies that, if some portion of the body is considered, the resultant forces on that portion are zero. When deformed occur, the arrangement is changed, and the body ceases to be in its original state of equilibrium. Forces, therefore, arise which tend to return the body to equilibrium [45, 67]. These forces which occur, when the body, is deformed can be described as internal stress. The internal stresses, in elasticity theory, cause "near-action" forces, which act from any point only to the neighbouring points, *i.e.* the forces exerted on any part of the body by surrounding parts act only on the surfaces of that part. Consider the total force on some portion of the body. Firstly, this total force is equal to the sum of all the forces on all

University of Cape Town

the volume elements in that portion of the body, *i.e.* it can be written as the volume integral $\int f dV$, where f is the force per unit volume, and $dF = fdV$ the force on the volume element dV. Secondly, the forces with which various parts of the portion considered act on one another can not give anything but zero in the total resultant force, since they cancel out by Newton's 3rd law. For any portion of the body, each of the three components f of the resultant force can be transformed by Gauss theorem into an integral over the surface.

$$\int f_i dV = \int \nabla.\sigma_{ij} dA, \qquad 3.4$$

Hence the vector f_i must be the divergence of tensor of rank two

$$f_i = \sum_k \partial\sigma_{ik} / \partial x_k, \qquad 3.5$$

where i and k in Eq. 3.5 refers to any component in any of the x, y and z directions, and x_k to a particular direction, x, y or z. The tensor σ_{ik} in Eq. 3.5 is called the stress tensor. By taking elements of area in plane of *xy, yz, zx*, we find that the component σ_{ik} of the stress tensor is the ith component of the force per unit area perpendicular to the x_k-axis.

University of Cape Town

To illustrate this, consider a simpler case - a small cubic volume element (as seen in Fig. 3.2) in a solid. The total stress state can be described by the forces perpendicular and parallel to the faces of the cube.

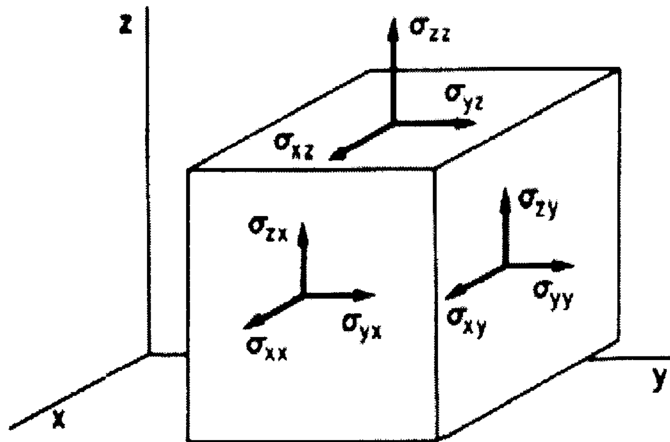

Fig. 3.2. Stress on a cubic volume in static equilibrium. Each surface has two types of forces, normal and shear [46].

University of Cape Town

For example as seen in Fig. 3.2, the force on a unit area perpendicular to x-axis, normal to the area (*i.e.* along the x-axis) is σ_{xx}. Similarly the forces per unit area along y and z axis are σ_{yx} and σ_{zx} respectively. The former is referred to as a normal stress, and the latter are called shear stresses. On each face in Fig. 3.2 there are three stresses, one normal stress σ_{ii}, and two shear stresses σ_{ij} ($i \neq j; i , j = x, y, z$), which all together give nine components of the stress tensor.

$$\sigma = \begin{pmatrix} \sigma_{xx} \, \sigma_{xy} & \sigma_{xz} \\ \sigma_{xy} \, \sigma_{yy} & \sigma_{yz} \\ \sigma_{zx} \, \sigma_{yz} & \sigma_{zz} \end{pmatrix} \qquad 3.5$$

Both stress and strain have at most six independent components, because of symmetry considerations as explained above. The strain tensor component of the deformation tensor is associated with the stress tensor as follows:

$$\sigma_{ij} = \sum_{k,l=1} C_{ijkl}\varepsilon_{kl}. \qquad 3.6$$

The constant C_{ijkl} in Eq. 3.5 is the fourth rank tensor of elastic constants (also known as the stiffness tensor). This expression is the generalized form of Hook's law. The inverse of the stiffness is called the compliance, and it is a fourth rank tensor defined by

$$\varepsilon_{ij} = \sum_{k,l=1} S_{ijkl}\sigma_{kl} \qquad 3.7$$

The stiffness and compliance tensors are both symmetric, and the number of their independent elements varies according to the material [46]. As the stress and strain tensors are symmetric, if the material can be assumed to be isotropic and homogeneous, the number of independent components of the tensor of elastic constants can be reduced significantly. For example, the stiffness and compliance matrixes for isotropic materials have only two independent elements, as compared to 21 independent elements in the case of triclinic crystals [46]. These two i.e. the stiffness and compliance tensors can be expressed in terms of Young's modulus (*E*) and Poisson ratio (*ν*), from which the shear modulus (*G*) can be derived. In general the principal strains for isotropic materials simplify to

$$\begin{aligned}
\varepsilon_x &= \frac{1}{E}[\sigma_x - \nu(\sigma_y + \sigma_z)], \\
\varepsilon_y &= \frac{1}{E}[\sigma_y - \nu(\sigma_z + \sigma_x)], \qquad 3.8 \\
\varepsilon_z &= \frac{1}{E}[\sigma_z - \nu(\sigma_x + \sigma_y)],
\end{aligned}$$

An amorphous solid has mechanical and structural properties that can be considered isotropic [2, 46], *i.e.* it has an identical compliance matrix to those of isotropic materials. We

University of Cape Town

can adopt this assumption in the present study for the determination of residual stress, as we will see in the nextchapte

3.1 RESIDUAL STRESS

Residual stress exists inside a material without application of an external load (applied force, displacement or thermal gradient) [43]. It may be categorized by cause (*e.g.* thermal or elastic mismatch), by the scale over which it self-equilibrates, or according to the method by which it is determined. However, averaged over the whole body, the net stress must be zero with all internal forces balanced. It is believed [8, 43, 44], that residual stresses originate from misfits between different regions of a material or composite materials. In many cases, these misfits span large distances, for example, those caused by the non-uniform plastic deformation of polycrystalline materials [6]. The basic principle [44] for the genesis of these stresses is simple: any transformation leading to a modification of the material dimensions creates internal stresses. Depending on the scale at which the stress is analyzed, different types of stress are conventionally defined. Two types of residual stress are therefore usually defined [6]: macro-residual stress extends over distances that are large relative to the characteristic size of the material, typically extending over many grains in polycrystalline materials. Macro-stresses, like all stresses are tensor quantities, with magnitudes varying with direction at a single point in the body. In contrast to tensor quantity micro-residual stresses are associated with structural defects, such as vacancies, dislocations. The resulting strains within the crystal lattice traverse distances on the order of, or less, than the dimensions of the grains in polycrystalline materials.

University of Cape Town

3.2 RESIDUAL STRESS IN LAYERED SYSTEMS

There are two principal types of stress in a layered structure, thermal stress and intrinsic stress [8, 12, 46, 47]. The former is due to the differences in the thermal expansion coefficient of the layer and the substrate. Temperature differences cause stress in the layer, *e.g.* upon cooling from the deposition temperature to room temperature, if the layer has a higher coefficient of thermal expansion than the substrate, then a tensile stress will result. This is because the constrained size of the layer at the final temperature is smaller than that of the substrate. Therefore it is stretched when constrained by substrate material. The formation of intrinsic stress, on the other hand, depends on the deposition process [46, 49, 56], but may also be caused by physical, chemical and structural transformations of the film during and after deposition. The more usual transformations may be (a) a film densification during deposition due to high energetic particle bombardment; (b) vacuum collapse between grain boundaries resulting in tensile stresses; (c) vacancy, interstitial, impurity or doping particle diffusion [8]. Interactions between the deposited layer and its environment may contribute to extrinsic stresses. These are often due to impurity adsorption in porous layers after deposition [8]. In other words, extrinsic stress is not the result of the growth process but usually arises when an external parameter is changed, after the film deposition, causing a stress without affecting its microstructure. Furthermore, intrinsic stress can occur during post-deposition treatment (for example, annealing, light-induced defect creation, plastic deformation *etc*). Besides theoretical models [50, 51], there are a number of experimental methods to determine stress in thin-film/ layers e.g. X-ray [15, 20, 43] and neutron diffraction, curvature methods [12, 15, 20, 43, 52], strain gauge [15, 44], material removal methods and their modifications. Each method has specific requirements on the specimens, instruments, measurement and

University of Cape Town

evaluation procedures, and they also differ in the richness and nature of provided information.

3.3 STRESS IN HYDROGENATED AMORPHOUS SILICON (a-Si:H)

For amorphous silicon to exist, the continuous random network (CRN) of atoms needs to be highly strained. Furthermore, the structure can be expected to be isotropic in real a-Si:H, because it exist as thin film constrained in the surface. As discussed above, the stress in layers constrained by a substrate may contain contributions due to thermal as well as an intrinsic stress due to the microstructure in the bulk of the film [12]. The intrinsic stress in *a*-Si:H films is compressive in nature [13, 15], and is generally correlated to the structural properties [12, 13].This compressive intrinsic stress may result from the so called atomic peening effect which causes the layer to become over-dense [54], and a further cause may be implantation of working gas atoms [55], though conclusive evidence for this latter effect has not been reported. However, the origin of the intrinsic stress in a-Si:H films for many deposition processes is related to the presence of hydrogen [53], although its correlation is not completely understood [12, 15, 20]. In the case of hot-wire chemical vapour deposition produced films; intrinsic stresses are related to the presence of defects [49]. Part of the strain in the CRN is relaxed by hydrogen termination of dangling bonds, but these hydrogen related defects are responsible for the subsequent degradation of the material [53]. An extreme case of the network relaxation is the transition from the amorphous to the crystalline state. Furthermore, the reaction of hydrogen with a growing amorphous silicon layer plays a crucial role - there is strong evidence [57] that during plasma deposition SiH-radicals are directly inserted into strained Si-Si bonds. Other studies suggest that, in high quality void free materials, hydrogen forms platelets (macro-voids) characterized by a strong interaction between the opposite sides

University of Cape Town

of the platelets and by net compressive stress [58, 61, 63]. This work agrees well with the work reported in [13], which suggested that the amount of hydrogen atoms in a monohydride (Si-H) configuration has a positive correlation with compressive stress, and that in a dihidride (Si-H_2) bonding configuration has an opposite correlation.

Stress in the film, can also arise from interface reactions leading to, e.g., density and/or bond configuration changes resulting from the formation of the secondary phases [47], finally, so-called growth zone or deposition stresses in a-Si:H can result from the non-equilibrium growth conditions associated with various deposition techniques [1, 47, 59]. In other words, non-equilibrium growth conditions may lead to density changes, the formation of voids, gas incorporation, *etc.*, and these aspects of the microstructure and composition influence the stress state. In this last case, the resulting stress is highly dependent on the details of the deposition process. Shimuzu [59], in his work on the three-dimensional growth zone model, established that hydrogen diffuses in the surface atomic layer to relax the network structure in *a*-Si:H. More recently Levi *et al* [60], showed the exceptional ability of real time spectroscopy ellipsometry (RTSE) to probe the growth mechanisms of a-Si:H in HW-CVD .

University of Cape Town

4 TECHNIQUES USED TO DETERMINE THE MICROSTRUCTURE AND RESIDUAL STRESS

Two approaches are commonly used to study the structure and residual stress in *a*-Si:H films, which include:

(i) The techniques that determine the film stress, from microscopic changes in the substrate (example of this is curvature method or microscopically by the determination of Raman peak shifts [64, 65],

(ii) Diffraction methods, which actually measure strain, such as X-ray diffraction [15, 20, 60].

In the latter case the film stress is calculated by Hookes law and this requires the knowledge of the elastic constants, which are not usually available for thin films. This section begins with a discussion of the technique, which can be employed to obtain structural information for amorphous silicon. In doing so, we introduce a variety of concepts and mathematical functions that will help us to describe the structure of (a-Si:H). In addition, we first consider those methods which give information on short-range order, that which extends over a few Angstroms. Consequently, the determination of residual stress and strain will be discussed, which complements the microstructure characterisation of a-Si:H.

University of Cape Town

4.1 DIFFRACTION TECHNIQUES

Two techniques employing synchrotron radiation have gained wide application to the study of amorphous materials namely, X-ray scattering or diffraction, and X-ray absorption spectroscopy. The latter can subdivide further as X-ray absorption fine structure (EXAFS) and X-ray absorption near-edge structure (XANES) spectroscopy [66]. In this work we

consider the X-ray diffraction technique as a means to study the short-range and possibly median-range structure of amorphous silicon. In this method the amorphous sample is bombarded with high energy X-rays as in a single crystal structure determination. However, since the amorphous solid lacks any long-range structure, coherent diffraction of the X-rays does not occur [2, 19, 66]. Rather, the X-rays are scattered and the manner in which they are scattered is observed. The scattering gives information about the position of the atoms relative to each other. For crystalline samples, this usually leads to the identification of a unit cell, from which the entire structure is known due to the presence of long-range periodicity and symmetry. However, in amorphous materials, the lack of periodicity and symmetry makes it impossible to identify a unit cell, which can be considered to be infinite in size. Every atom would have to be identified in order to accurately determine the structure as a whole [66].

4.2 BASIC DIFFRACTION THEORY

The diffraction of X-rays by matter is the basis of a unique scientific tool. It is most powerful when applied to crystalline materials, but it can yield fundamental and important structural information when applied to amorphous materials. This section seeks to present briefly certain aspects of X-ray diffraction necessary in determining the structure amorphous materials. A more extensive and authoritative discussion on this subject, can be found in the following references [6, 19, 67, 68].

It is a fundamental property of all waves that they scatter on meeting an obstacle, and this effect is most pronounced when the size of the obstacle is comparable to the wavelength of the wave [2, 19]. This is true for electrons and neutrons as it is for X-rays, and since all can

University of Cape Town

have wavelengths comparable to atomic dimensions, it is expected that the diffraction from atoms in the condensed state will occur [6, 19]. If the wavelength of these scattered X-rays does not change (meaning that X-ray photons do not lose any energy), the process is called elastic scattering (Thompson Scattering), because only momentum has been transferred in the scattering process. These are the X-rays that we measure in diffraction experiments, as the scattered X-rays carry information about the electron distribution in materials. On the other hand, in the inelastic scattering process (Compton Scattering), X-rays transfer some of their energy to the electrons and the scattered X-rays will have different wavelength than the incident X-rays [2, 6, 19]. Diffracted waves from different atoms can interfere with each other and the resultant intensity distribution is strongly modulated by this interaction. Measuring the diffraction pattern therefore allows us to deduce the distribution of atoms in a material. The peaks in the X-ray diffraction pattern are directly related to the atomic distances according to the well-known Bragg equation

$$n\lambda = 2d\sin\theta \ . \qquad 4.1$$

Here λ is the incident X-ray beam wavelength (typically measured in angstroms), d is the atomic spacing for a particular set of planes (also in angstroms), θ is the angle to the surface and n is the order of diffraction. When these conditions are satisfied, a peak in the X-ray intensity will occur. A typical powder diffraction pattern consists of a plot of diffracted intensities (peaks), that are caused by layers of atoms in the material, versus the diffraction angle 2θ. The diffraction angle, 2θ, is the angle between the incoming X-ray beam and the diffracted intensity. Furthermore, the areas under the peaks are relative to the amount of each phase present in the spectrum [19]. For a single crystal, the diffraction pattern consists of a number of sharp peaks [2]. An example of such a pattern is shown in Fig. 4.1(a). From

University of Cape Town

the positions and the intensities of the peaks, the atomic positions in the unit cell can be determined.

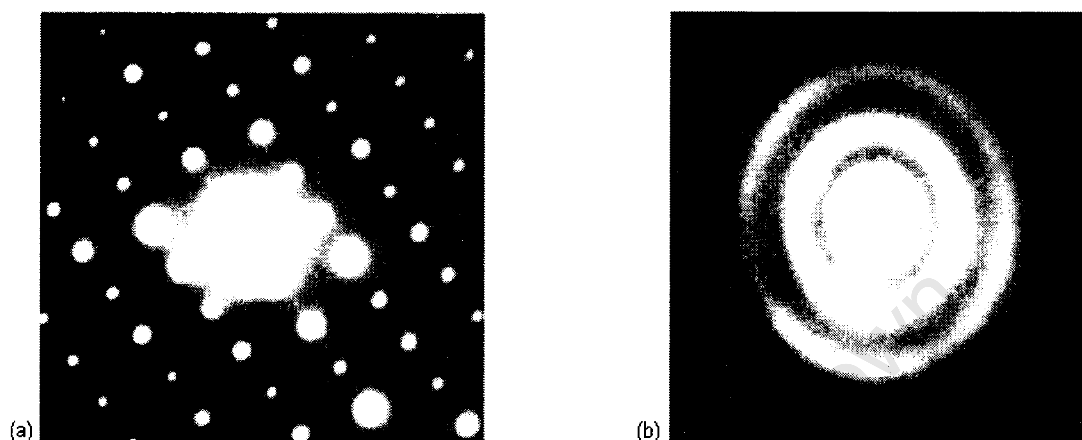

Fig. 4.1. Electron diffraction patterns showing: (a) a crystalline form and (b) amorphous form [26, 50].

The diffraction pattern of an amorphous material is strikingly different. The pattern in this case consists of broad diffuse rings [2] as can be seen Fig. 4.1(b). This result indicates that the structure does not contain a repeating unit cell. The only quantity which can be determined from the diffraction pattern, in this case is the RDF [2], which is the subject of the next section.

4.3 DIFFRACTION FROM AMORPHOUS MATERIALS

The expression 'diffraction method' here refers to the techniques using X-ray diffraction as means to study structural characteristics of amorphous materials. The total scattering intensity (I_{tot}) from an amorphous material, after correction for polarization and absorption effects, is composed of the interatomic interference scattering

University of Cape Town

$$I_{\text{int}} = \sum f^2{}_i(q), \qquad 4.2$$

The coherent scattering

$$I_{coh} = \sum_{i \neq j} \sum f_i(q) f_j(q) \frac{\sin qr_{ij}}{qr_{ij}} \qquad 4.3$$

and the incoherent scattering (I_{inc} = Inelastic electron-photon interaction) such that:

$$NI_{tot}(q) = I_{\text{int}}(q) + I_{coh}(q) + I_{inc}(q) \qquad 4.4$$

where N is the number of formula units in the scattering volume, $q = (4\pi/\lambda)\sin\theta$ is the scattering vector , and $f_i(q)$ is the scattering factor for atom i, which is proportional to the total number of electrons in atom i, and r_{ij} is the distance between atoms i and j. An intensity function $i(q)$, which is the coherent scattering intensity ($I_{coh}(q)$), and which corresponds approximately to the scattering intensity from point atoms obtained from

$$i(q) = I_{tot}(q) - (I_{\text{int}}(q) + I_{inc}(q)). \qquad 4.5$$

The resulting diffraction data are usually given in the form of radial distribution function (RDF) [2, 19, 21, 69].

4.4 CALCULATION OF RADIAL DISTRIBUTION FUNCTIONS

All materials scatter X-rays, even if they are not crystalline. Deviation from perfect periodicity spreads the scattering out through reciprocal space, but there is still some information about interatomic distances [2]. The intensity in electron units scattered by a non-crystalline array of atoms at an angle θ is given by Debye's equation, and can be used to extract information for all materials:

$$I(q) = \sum_{i \neq j} \sum f_i(q) f_j(q) \frac{\sin(qr_{ij})}{qr_{ij}} \qquad 4.6$$

University of Cape Town

where f_i, f_j are the respective atomic scattering factors of the ith *and* j^{th} atoms, and r_{ij} is the distance separating these two atoms as described above. In the present investigation, since the amorphous structure is observed over a range of compositions for different systems, it is assumed that the two kinds of atoms in each sample occupy random positions in the amorphous structure. An average scattering factor and atomic number are then introduced in the computations. In other words, it is considered that in an amorphous phase consisting of two elements, the atoms are distributed at random so that the phase is regarded as being made of one kind of average atoms. Hence

$$f_i = f_j = f, \quad f_i f_j = f^2. \qquad 4.7$$

In performing the summation, it is necessary to consider one atom as the origin and to carry out the summation over all distances to all atoms of the specimen. Thus for N atoms in all,

$$I(q) = Nf^2(q)\left[1 + \sum_i \frac{\sin(qr_{ij})}{qr_{ij}}\right] \qquad 4.8$$

The summation of this expression excludes the atom at origin. Furthermore, it is assumed that in amorphous phases the distribution of atoms is continuous; then the above summation may be replaced by an integral, *i.e.*

$$I(q) = Nf^2\left[1 + \int_0^R 4\pi r^2 \rho(r) \frac{\sin(qr)}{qr} dr\right]. \qquad 4.9$$

In this expression, $\rho(r)$ is the density of atoms at distance r from the origin. Hence $4\pi r^2 \rho(r) dr$ is the number of atoms in a spherical shell of radius r and thickness dr. The upper limits of integration R is a measure of dimension of the amorphous specimen which is very large compared with the microscopic value r. Rewriting the above equation by introducing ρ_o as the constant average density of atoms,

University of Cape Town

$$I(q) = Nf^2\left[1+\int_0^R 4\pi r^2(\rho(r)-\rho_o)\frac{\sin(qr)}{qr}dr+\int_0^R 4\pi r^2\rho_o\frac{\sin(qr)}{qr}dr\right]. \quad 4.10$$

The second integral corresponds to the small-angle scattering intensity of uniformly dense material which is usually unobservable because of the presence of the main beam. Hence, if attention is limited to experimentally observable intensities, this integral can be taken as zero [2, 3, 19]. It can be expected that within the a-Si:H system, $\rho(r)$ rapidly approaches ρ_o when r exceeds several atomic diameters; thus R is safely taken as infinity. Two further functions can now be defined in order to simplify the expression [22]. The 'reduced scattering intensity' $qi(q)$, is defined as

$$qi(q) = \int_0^\infty 4\pi r[\rho(r)-\rho_o]\sin(qr)dr. \quad 4.11$$

Here the function $i(q) = \frac{I(q)}{Nf^2(q)} - 1$, is called reduced interference function and the 'reduced radial distribution function', G(r), is defined as:

$$G(r) = 4\pi r[\rho(r)-\rho_0]. \quad 4.12$$

Thus Eq. 4.11 can be written in the form:

$$qi(q) = \int_0^\infty G(r)\sin(qr)dr. \quad 4.13$$

The reduced RDF Eq. 4.12, is associated by a Fourier transformation with the interference function (or reduced scattering intensity) $qi(q)$, which is the structure-dependent part of the experimental X-ray data [69]. By the Fourier integral theorem, the above equation is transformed into

$$r[\rho(r)-\rho_o] = \frac{1}{2\pi^2}\int_0^\infty qi(q)\sin(qr)dq. \quad 4.14a$$

University of Cape Town

This can also be rewritten as

$$4\pi r^2 \rho(r) = 4\pi r^2 \rho_o + \frac{2r}{\pi} \int_0^\infty q i(q) \sin(qr) dq. \quad 4.14b$$

These functions are a one-dimensional representation of the three dimensional structure of the amorphous material. The radial distribution and the correlation functions can be thought of as probability functions that give the chances that the surface of a sphere of radius, r, from some central atom, will intersect other atoms. The former function i.e. RDF is equivalent to $4\pi r^2 \rho(r)$. These functions are averages over the entire system. This is analogous to choosing every atom in the system as the central atom and calculating an RDF for each. Taking the average of the calculated RDF's of every atom in the system would give the radial distribution function derived by experiment. Therefore, diffraction experiments give information about the average structure of amorphous materials, and not the absolute structure [2, 19, 66]. It is important to note that though RDF represents real-space structural information, it can only yield a limited amount of information by inspection, restricted essentially to the local structure around a given atom, namely bond length and bond angles. The radial distribution function (RDF) is one of the common forms of representing real-space structural information, and it has a typical form shown schematically in Fig. 4.2. The characteristics features are a series of peaks becoming broader and less well defined with increasing r. This reflects the common property of all covalent amorphous semiconductors, that there is a degree of short-range order at the first and second order neighbor distance, but the spatial correlations decrease rapidly. The importance of the correlation function lies principally in the fact that the area under a given peak gives the effective coordination number of the particular shell, or simply put, the peaks in RDF(r) indicate frequently occurring atom-

University of Cape Town

atom distances, and the area under a peak is equal to the average number of atom pairs within a particular range of distances [19, 69].

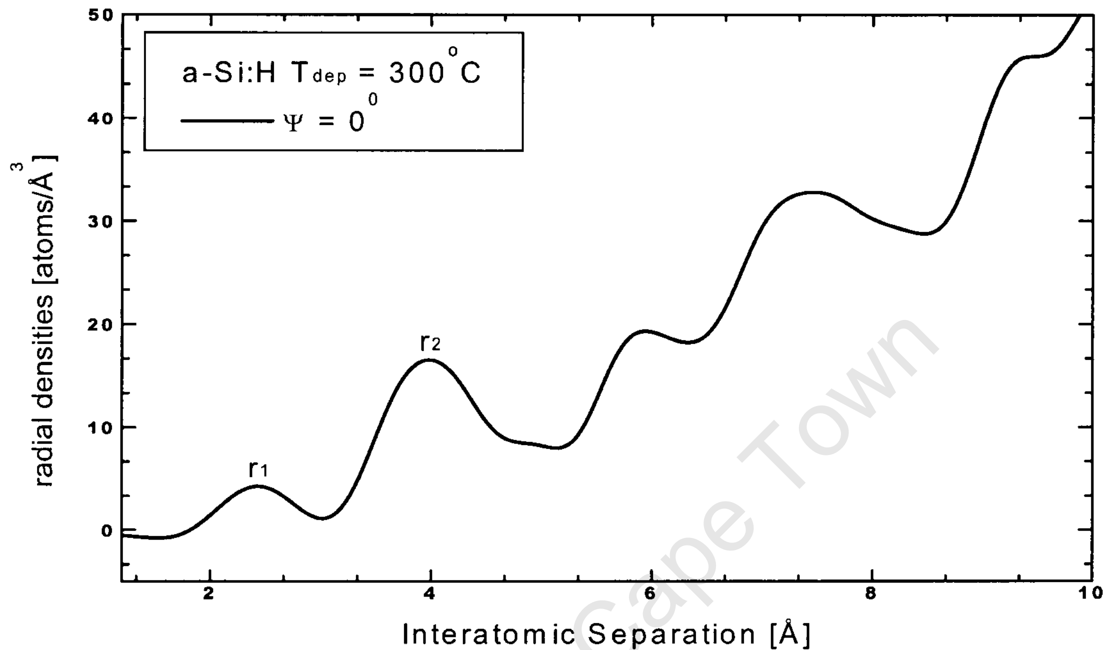

Fig. 4.2. Radial Distribution Function of a-Si:H in real space (plotted using RAD [69])

The position of the first peak gives a value for the nearest-neighbor bond length, r_1 and similarly the position of the second peak gives a value of next-nearest-neighbor distance r_2. This value arises from a second neighbor atom at a distance $2r_1 \sin\left(\frac{\alpha}{2}\right)$, where α is the bond angle.

4.5 DETERMINATION OF STRAINS AND STRESS FROM X-RAY DIFFRACTION

Since early 1930s, X-ray diffraction has been established as a method that can be applied for stress determination [19, 67]. Using this method, the stress in a material is calculated from the change in the spacing of crystal lattice planes *d*, under the assumption that the relation between

University of Cape Town

the change in d and the stress follows Hooke's law. Therefore, this method is essentially different from the method of mechanical methods of stress determination as a microscopic gauge length is used. In [67] the following three characteristics of the X-ray stress determination are described:

(i). **Non-destructive measurement**

In the X-ray method, the reflecting angle of the X-ray beam is the only quantity to be measured. Therefore, the measurement procedure is entirely non-destructive, which is basically different from the mechanical method. In the mechanical method of residual stress determination, the strain due to the stress release on removing a part of material must be measured. It is therefore, the intrinsically destructive.

(ii). **Near surface sensitivity**

Since the X-ray penetration is at most on the order of ten microns, stress is determined only in a thin surface layer of the sample. This can be an advantage in some cases, for example in thin films and coatings. On the other hand, it is almost impossible to determine the stress in a thin surface layer by a mechanical method. If the stress distribution varies sharply in the surface layer, for example, it is possible to determine the stress distribution easily by removing the surface layer little by little. Such procedures are, however, no longer non-destructive.

(iii). **Lateral resolution**

Depending upon the sample geometry or grain size, the area illuminated by X-rays can be reduced to less than a millimeter (mm) in diameter if a decrease in accuracy is allowed. It is therefore, possible to probe stress distributions that vary locally.

University of Cape Town

X-ray determination naturally has some problems as well as some restrictions in its application. Problems include: uncertainty in the elastic modulus that is required when strain measured by X-ray diffraction is converted to stress; restrictions caused by grain size, texture, surface roughness, *etc*; and the difference between the local stress and the mechanical mean stress. In the determination of applied stress or residual stress in a polycrystalline material that is elastically homogeneous and does not have texture, it is well known that the X-ray method yields accurate values. If we understand the advantages and disadvantages of this method, apply it to an appropriate procedure, and analyze the results correctly, we will be able to obtain much useful information.

4.6 EFFECT OF STRAIN ON DIFFRACTION PATTERNS

In recent years, there has been considerable interest in understanding the origin of residual stresses and relating them to the microstructure in thin films. One example is that of a polycrystalline thin-film material with significant disorder.

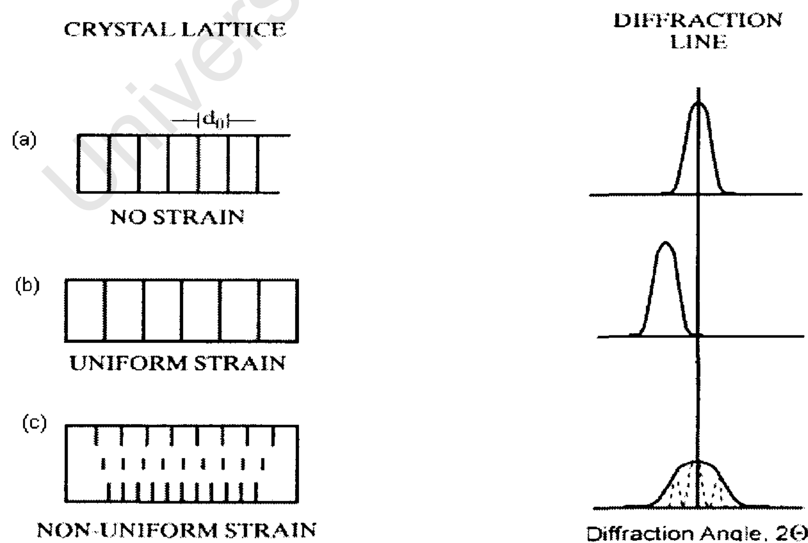

Fig. 4.3. Illustration of uniform strain and non-uniform strain [6]

In this case, if the stress varies from grain to grain the stress, or within the grain, it is referred to as micro-residual stress. On the other hand, the stress may be uniform over large distances, and this is referred to as macros-stress. To see the effects of both kinds of strain on the diffraction patterns, consider the unstrained crystals and the corresponding diffraction line as shown in Fig. 4.3.a-c. When the lattice is given a uniform tensile strain, normal to the lattice planes, their lattice spacing becomes smaller and the corresponding diffraction line shifts to a lower angles. This uniform strain, as illustrated in Fig. 4.3, produces a peak shift of the diffraction line to a new 2θ position.

On the other hand, if the material is deformed, the lattice planes become distorted, such that the spacing of any particular (*hkl*) set varies from one grain to another or from one part of a grain to another. This non-uniform micro-strain produces a peak broadening of the corresponding diffraction line as indicated in Fig. 4.3c. The elastic behaviour of polycrystals depends on the crystal elastic constants of its constituents and the microstructure. We may imagine this as a grain to be composed of small regions, each having the same plane spacing constant, but changed from the spacing in the adjoining regions. All regions contribute equally to the diffraction pattern with different diffraction lines (dotted line Fig. 4.3c), and the result is the sum of sharp lines generated by non-uniform strains.

In order to address the residual stress question related to atomic arrangement in the present work, we need to follow the procedure proposed by Härting *et al* [15, 20]. In this work, they suggested that the stress responsible for strain in a-Si:H can be evaluated assuming linear elastic deformation, leading to shift of the first two diffraction peaks. Since in a-Si:H, the

University of Cape Town

height of the basic tetrahedron is not the same for each tetrahedron (bond length and interatomic distance can change), it can be compared to a different part of itself.

4.7 DETERMINATION OF STRAIN FROM DIFFRACTION

The procedure followed is diffraction-based strain measurement. This technique relies on the use of the interatomic spacing in the material as an internal strain gauge. To properly describe the results of a diffraction strain measurement, we have to worry about a coordinate system for the instrument and the sample. These two coordinate systems are related by two rotation angles ψ and ϕ, as illustrated in Fig. 4.4.

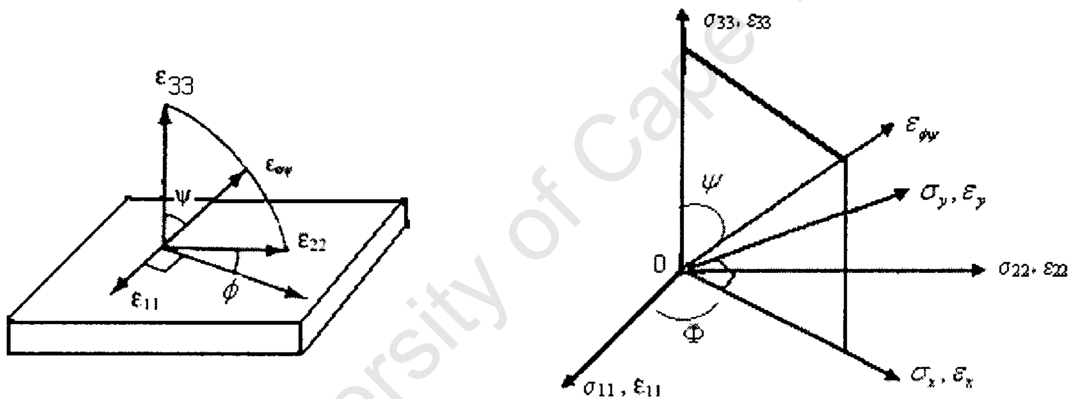

Fig. 4.4. Schematic representation of the laboratory coordinate system and the sample coordinate system for strain and stress components and Euler angles (ϕ,ψ) (Drawn from [67, 85])

The procedure is based on measurements of variation of the diffraction peak position for a (*hkl*) family of planes as a function of the two Euler angles, the azimuth ϕ and the tilt angle ψ [70]. If the characteristic radiation of wavelength λ is irradiated into a material, it is diffracted only from the lattice planes satisfying Braggs' diffraction condition as formulated in Eq. 4.1 [19, 67, 71]. If the grains are small enough, and there are enough grains in the area

University of Cape Town

illuminated, and the orientation of the grains is random, then diffraction should take place uniformly along the surface of the sample [19].

If the small changes Δd in spacing of the lattice planes d are created by a stress imposed on the materials, the reflecting angle θ is changed as a result, and by differentiating Eq. 4.1 we obtain

$$\frac{\Delta d}{d} = -\cot\theta\Delta\theta. \qquad 4.15$$

This equation indicates that the change in θ can be converted to the change in the spacing of the lattice planes. If the unstrained lattice spacing and the corresponding diffraction angle d_0 and θ_0, respectively, then the measured strain in the direction of the normal to the reflecting plane $\varepsilon_{\phi\psi}$ is approximated by the following equation [6, 67]:

$$\varepsilon_{\phi\psi} = \left(\frac{\Delta d}{d}\right)_{\phi\psi} = \frac{d_{\phi\psi} - d_0}{d_0} = -\cot\theta_0(\theta_{\phi\psi} - \theta_0). \qquad 4.16$$

4.8 STRAIN-STRESS RELATION

If it is assumed [19, 67] that the strain ε was produced by stress σ acting in a single direction, Hooke's law requires that

$$\varepsilon = \frac{\sigma}{E} \ , \qquad 4.17$$

where E is Young's modulus. If a tension σ_z is applied along the Z axis of the body, the body will elongate in Z direction and the strain becomes

$$\varepsilon_z = \frac{\sigma_z}{E}. \qquad 4.18$$

University of Cape Town

At the same time, the body contracts equally along its X and Y axes, and these strains are related to ε_z through Poisson's ratio ν as follows:

$$-\varepsilon_x = -\varepsilon_y = \nu\varepsilon_z = \frac{\nu\sigma_z}{E} \qquad 4.19$$

The negative sign here denotes the contraction [6, 19]. This simple stress system is one-dimensional with respect to the direction of stress. The strains in three-dimensional stress system, however, are readily obtained from expressions 4.18 and 4.19 by the principle of superposition, giving

$$\varepsilon_x = \frac{1}{E}[\sigma_x - \nu(\sigma_y + \sigma_z)],$$

$$\varepsilon_y = \frac{1}{E}[\sigma_y - \nu(\sigma_z + \sigma_x)], \qquad 4.20$$

$$\varepsilon_z = \frac{1}{E}[\sigma_z - \nu(\sigma_x + \sigma_y)].$$

The strains considered above are designated normal strains since they are produced by stress normal to a surface. Usually, such normal strains are accompanied by additional shear strains, in a plane normal to the stress direction.

In our case, since X-ray diffraction takes place only in a shallow surface layer. It is assumed, that the stress component σ_{33} in the direction normal to the surface is zero [19, 20, 85]. Therefore, if the other principal stresses σ_{11} and σ_{22} are taken parallel to the sample surface, then the relationship between stresses and strains are

$$\varepsilon_{11}E = \sigma_{11} - \nu\sigma_{22} \qquad 4.21a$$

$$\varepsilon_{22}E = \sigma_{22} - \nu\sigma_{11} \qquad 4.21b$$

University of Cape Town

$$\varepsilon_{33} = -\nu(\varepsilon_{11} + \varepsilon_{22}) = \frac{-\nu}{E}(\sigma_{11} + \sigma_{22}) \qquad 4.21c$$

Because stress is a tensor entity, the complete stress tensor has to be calculated [73]. This is achieved by transforming the strain in the sample coordinate system ε_{ij} following the transformation tensor [71, 72] defined by:

$$(\varepsilon_{33})_{\Phi\Psi} = a_{3k} a_{3l} \varepsilon_{kl}, \qquad i,k,l = 1,2,3 \qquad 4.22$$

where a_{ik} and a_{il} are the direction cosines between the laboratory system and the sample coordinate system, respectively. In terms of the experimental angles ψ and ϕ, the transformation matrix can be written as

$$a = \begin{bmatrix} \cos\phi\cos\psi & \sin\phi\cos\psi & -\sin\psi \\ -\sin\phi & \cos\phi & 0 \\ \cos\phi\sin\psi & \sin\phi\cos\psi & \cos\psi \end{bmatrix} \qquad 4.23$$

For diffraction, it is only possible to determine the lattice strain, for a given (*hkl*) plane spacing, in the direction of the bisector of the incident and diffracted beams. In order to calculate the stress (or strain) tensor at a sampling gauge location, at least six independent measurements of strain in different directions $\varepsilon_{\phi\psi}$ are required [20, 43, 73-77, 84].

The strain vector, $\varepsilon_{\phi\psi}$ in the direction (ϕ, ψ) is related to the other Cartesian strain tensor components ε_{ij} by [20, 84]:

$$\varepsilon_{\phi\psi} = \varepsilon_{11}\cos^2\phi\sin^2\psi + \varepsilon_{22}\sin^2\phi\sin^2\psi + \varepsilon_{33}\cos^2\psi + \varepsilon_{12}\sin 2\phi\sin^2\psi$$

$$+\varepsilon_{13}\cos\phi\sin 2\psi + \varepsilon_{23}\sin\phi\sin 2\psi = \frac{d_{\phi\psi} - d_0}{d_0}. \qquad 4.24a$$

University of Cape Town

ε_{ij} are strain tensor components in the sample coordinate system, and the measurement at six or more different $\phi\psi$ can give all of the strain tensor components. Eq. 4.20 can also be rewritten in the following form [83]:

$$\varepsilon_{\phi\psi} = \frac{d_{\phi\psi} - d_0}{d_0} = (\varepsilon_{\phi} - \varepsilon_{33} + \varepsilon_{12}\sin 2\phi)\sin^2\psi + (\varepsilon_{13}\cos\phi + \varepsilon_{23}\sin\phi)\sin 2\psi + \varepsilon_{33} \qquad 4.24b$$

with

$$\varepsilon_{\phi} = \varepsilon_{11}\cos^2\phi + \varepsilon_{22}\sin^2\phi .$$

The strain tensor component can then be used to determine the stress tensor components, and the general strain–stress relationship is described by Hooke's law tensor equation

$$\sigma_{ij} = C_{ijkl}\varepsilon_{kl}, \qquad 4.25a$$

where ε_{ij} and σ_{ij} are the strain and stress components in the sample, and C_{ijkl} is the stiffness tensor [84]. The elastic strain produced by an applied stress is given by a set of equations similar to Eq. 4.25 (a)

$$\varepsilon_{ij} = S_{ijkl}\sigma_{kl}. \qquad 4.25b$$

The constant S_{ijkl} are called compliances, and Eq. 4.25b shows that one component of stress can produce non-zero values of all of the strain components [14]. The indices mark the three different directions in space [14, 78].

By recording the peak shift as a function of the sample tilt angle ψ, the residual stress can be determined using elasticity theory. According to the elasticity theory, for a linear isotropic medium, strain is related to stress via Hooke's law and can be expressed as follows [70, 76]:

$$\varepsilon_{ij} = \frac{1+\nu}{E}\sigma_{ij} - \delta_{ij}\frac{\nu}{E}\sigma_{kk} \qquad 4.26$$

University of Cape Town

where k is the dummy suffix summing over all k (i.e. $\sigma_{kk} = \sigma_{11} + \sigma_{22} + \sigma_{33}$). The dependence of elastic stress and strains on the direction scattering vector given by (ϕ, ψ), is achieved by using Eq.4.22 and Eq. 4.26, and this leads to

$$\varepsilon_{\phi\psi} = \frac{1}{2} S_1[\sigma_{11} \cos^2 \phi \sin^2 \psi + \sigma_{22} \sin^2 \phi \sin^2 \psi + \sigma_{33} \cos^2 \psi + \sigma_{12} \sin 2\phi \sin^2 \psi + \sigma_{13} \cos\phi \sin 2\psi + \sigma_{23} \sin\phi \sin 2\psi] + S_2[\sigma_{11} + \sigma_{22} + \sigma_{33}]. \quad 4.27$$

S_1 and S_2 in Eq. 4.27 are the X-ray elastic constants for a particular set of lattice planes. If these are unknown, approximate values can be expressed in terms of Young modulus, and the Poisson ratio, namely $\frac{1}{2} S_2 = (1+\nu)/E$ and $S_1 = -\nu / E$[70]. In our case, The stress tensor $\varepsilon_{\phi\psi}$ is at an angle ψ, to the surface normal (as illustrated in Fig. 4.4). Therefore, the observed stress state is effectively along the surface of the layer [70], and it can be assumed to be biaxial. This requires that the following condition must hold, $\sigma_{13} = \sigma_{23} = \sigma_{33} = 0$. with this assumption, Eq.4.27 can be expressed as

$$\varepsilon_{\phi\psi} = \frac{1+\nu}{E} \sigma_\phi \sin^2 \psi - \frac{\nu}{E}(\sigma_{11} + \sigma_{22}) \quad 4.28$$

σ_ϕ is the stress component in the ϕ direction, as illustrated in Fig. 4.2, and is given by

$$\sigma_\phi = \sigma_{11} \cos^2 \phi + \sigma_{12} \sin 2\phi + \sigma_{22} \sin^2 \phi \ . \quad 4.29$$

When the bulk elastic constants are not well known, it is more appropriate to eliminate them, and work directly in terms of strain [6, 20, 79]. This can be achieved directly using the fact that, although the stress σ_{33} is zero, the strain ε_{33} is not zero. This means that, it has a finite value given by the Poisson contractions due to σ_{11} and σ_{22} leading to equation 4.21c. Now using 4.21c and the strain equation derived in equation 4.28 we have:

$$\varepsilon_{\phi\psi} = (\varepsilon_{11} - \varepsilon_{33}) \sin^2 \psi + \varepsilon_{33}. \quad 4.30$$

University of Cape Town

Eq.30 requires that the rotational symmetry of the strain state be assumed, with $\varepsilon_{11} = \varepsilon_{22} = \varepsilon_{12} = 0$. Only then the strain state can be deduced and with the knowledge of the elastic constant the stresses can be determined using equation 4.21c. The method of X-ray stress determination based on Eq. 4.28 or Eq. 4.30 is generally called the $\sin^2\psi$ method [67, 70].

4.9 RESIDUAL STRESS CALCULATION

The stress in the ϕ coordinate system can be calculated directly from the slope of the least square line fitted to the experimental data, measured at various ψ, if the elastic constants *E*, ν and the unstressed plane spacing, d_0 are known [80]. This can be achieved by using the following equation

$$\frac{1}{2}S_2 = \frac{\nu + 1}{E} \quad . \tag{4.31}$$

Equating the slope of the $\varepsilon_{\phi\psi}$ - $\sin^2\psi$ curve to

$$\frac{\partial(\varepsilon_{\varphi\psi})}{\partial(Sin^2\psi)} = \frac{1}{2}S_2\sigma_\phi, \tag{4.32}$$

the residual stress can be obtained from

$$\sigma_\phi = \frac{\partial(\varepsilon_{\varphi\psi})}{\partial(Sin^2\psi)}\frac{E}{\nu + 1}. \tag{4.33}$$

In this case Bragg's condition, as defined by Eq.4.1, does not indicate the angular relation between the X-ray beam and the sample, but that between the X-ray beam and the orientation of a grain in the sample.

University of Cape Town

5 EXPERIMENTAL DETAILS

In this chapter the sample preparation, measurements and data manipulation necessary for this work are presented.

5.1. SAMPLE PREPARATION

The hydrogenated amorphous silicon (a-Si:H) layers were provided by Evarist Minani of UCT's solid state group, produced using the hot-wire chemical vapor deposition (HWCVD) system at the University of the Western Cape. In this process pure silane (SiH_4) at a pressure of 40 μbar is catalytically decomposed by tantalum filaments, maintained at 1600 °C. In all cases the gas flow rate was 60 sccm. For the production of uncoated substrate materials, as a reference, the silane was replaced by hydrogen in the deposition system, with the other parameters kept constant. The layers were deposited on corning 7059 glass substrates at the temperature of 300 °C and 500 °C respectively. The thicknesses of the deposited layers were estimated by UV absorption spectroscopy and ranged from 1.3 μm to 1.7 μm. More details on the procedure carried out to measure these thicknesses and other microstructure evaluation can be found in ref [20].

5.2 DIFFRACTION MEASUREMENT

The synchrotron radiation diffraction measurements were performed using the 3-axis XPD difractometer on beamline 10B at the Laboratório Nacional de Luz Sìncrotron (LNLS), Brazil. As described in chapter 4 the usual procedure to determine the residual stress state in the sample requires measuring the lattice spacing d as a function of measurement directions ψ

University of Cape Town

(angle between the normal to the reflecting planes and the specimen surface) and ϕ (azimuth angle). By varying the sample tilt ψ at constant direction ϕ (see Fig. 5.1) the diffracted intensity of several lattice planes is measured, and the strain $\varepsilon_{\varphi\psi}$ can be determined according to Eq. 4.20. For stress determination in amorphous materials, in which the distinct sets of lattice planes indicated in Fig. 5.1 are replaced by approximate distances it is necessary to record a full diffraction pattern at each ψ tilt.

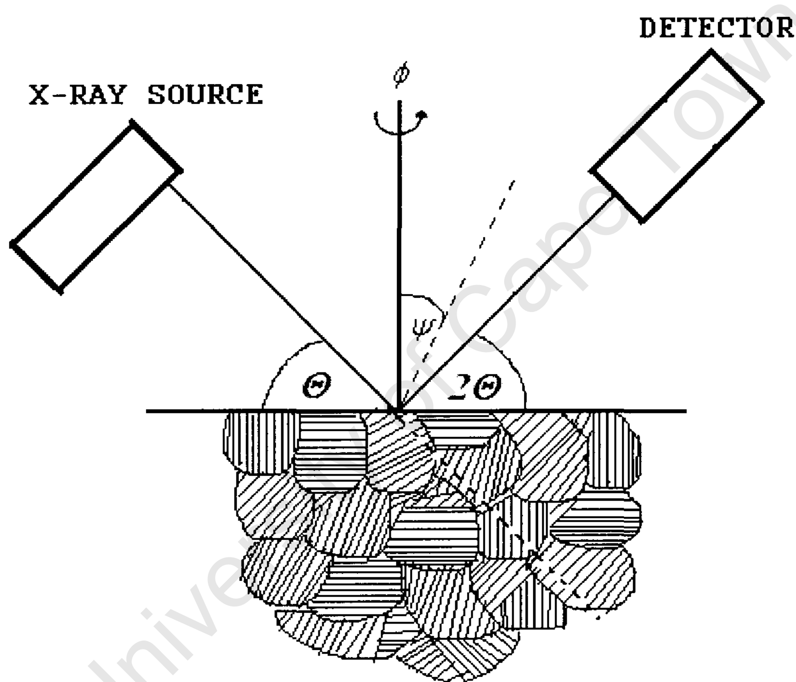

Fig. 5.1 Overview of the measurement procedure (Fig drawn from [84])

These intensity profiles were measured using 11 ke$V$ radiation, corresponding to a wavelength of 1.125 Å over a 2θ range of 4° to 129° in steps of 0.025°. Under these conditions, the maximum scattering vector ($q = (4\pi/\lambda)\sin\theta$) is 10 $Å^{-1}$. This q-value is crucial to resolve the small differences in the bond lengths. As an internal strain gauge the positions of the first and second amorphous scattering peaks corresponding to the (111) and

(220) Bragg reflections in crystalline silicon, were used in the $\sin^2\psi$ analysis. Beyond this, the radial distribution function was calculated to provide real space distances given by the first and second nearest neighbour separations. The specific ψ tilt angles considered for these reflections are 0°, 20°, 40°, 60°, $80^\circ$and 85°, respectively.

5.3 BACKGROUND SUBTRACTION

The complete experiments as described above comprised the measurement of the diffraction patterns for the glass substrate with the amorphous layer and the additional uncoated glass substrate, both of which were subjected to the same conditions. This was done to separate the contribution of the glass substrate from a-Si:H layer in the experimental data. The synchrotron radiation can penetrate through the *a*-Si:H layer, therefore the diffraction pattern has contribution from both the film and the substrate. Fig 5.2 shows the contribution of the layer and that of the glass plotted together.

University of Cape Town

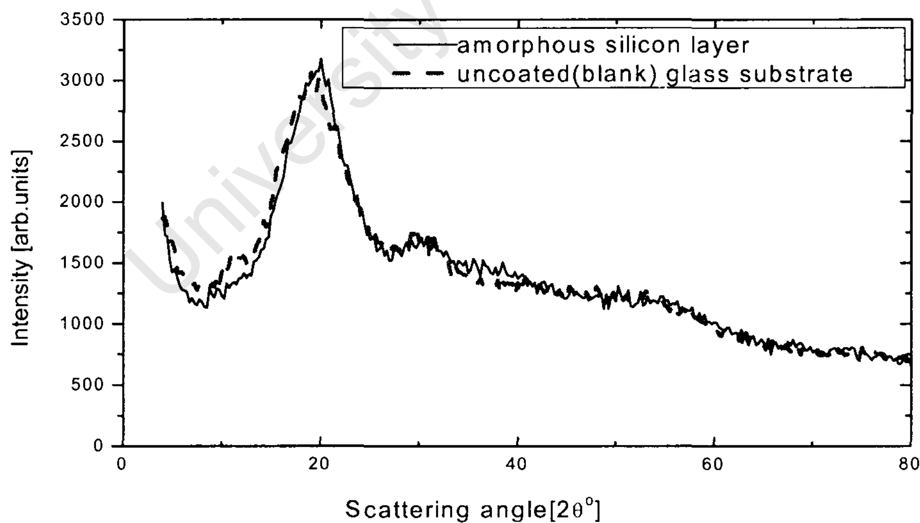

Fig. 5.2 Synchrotron diffraction patterns for an uncoated glass substrate and for an a-Si:H layer deposited on the glass substrate.

A glass was chosen as a substrate because it has an amorphous structure and as such, it should contribute a smooth slowly varying background to the diffraction patterns. We should expect the observed X-ray scattering intensity to be the combination of a-Si:H layer and background contributions which can be represented by the following equation:

$$I^{Obser} = I^{a-Si:H} + I^{Blan.Subst}. \qquad 5.1$$

I^{Obser} in Eq. 5.1 is the observed X-ray scattering intensity, $I^{a-Si:H}$ represents the hydrogenated amorphous silicon layer, and $I^{Blan.Subst}$ is the substrate contribution. As can be seen in Fig. 5.2, the substrate contribution dominates the measured diffraction pattern. The procedure followed for the substrate background subtraction uses the weighted intensities of the layer and substrate contributions. To illustrate this procedure, let the diffracted intensity of an uncoated substrate be $I^{unc}(\theta)$, and that of a coated substrate be $I^{coat}(\theta)$. The X-ray scattering intensity from the coating can then be estimated from the following relationship:

$$I^{Corr}(\theta) = I^{coat}(\theta) - \beta I^{Unc}(\theta) \qquad 5.2$$

Where θ is the scattering angle and β is the scale factor for background correction determined following the path length through the layer, which in this measurement is dependent on the angles θ and ψ. In this procedure, a separate pattern for each tilt angle ψ of the glass is recorded first and then used for background subtraction. If this was not the case, an additional factor containing cosψ would have to be considered in Eq.5.2. Since the surface layer contributes the fraction β of the total diffracted intensity, it can be estimated from the absorption law:

$$\beta = \frac{I}{I_0} = \exp[-(\mu / \rho)\rho t] \qquad 5.3$$

University of Cape Town

The factor I in Eq. 5.3 defines the intensity of the primary beam after traveling a distance t; I_0 is the intensity of the incident beam, μ is the X-ray linear absorption coefficient, and ρ is the density of the sample [40].

The path length is expressed in terms of the layer thickness and also takes the scattering angle θ and the tilting angle ψ into consideration. In mathematical terms this can be expressed as

$$t = \frac{x}{\sin\theta \cos\psi}. \qquad 5.4$$

Combining equations 5.3 and 5.4, the absorption law can be expressed as

$$\beta = \exp\left(-\frac{2\mu x}{\sin\theta \cos\psi} \right). \qquad 5.5$$

The factor β in Eq. 5.5 considers that the radiation has to pass through the layer twice, namely, before and after the reflection.

University of Cape Town

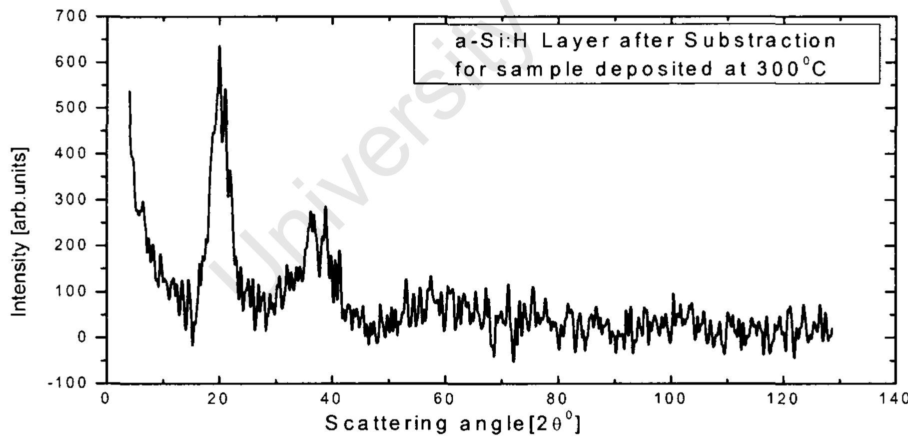

Fig. 5.3. Illustration of the background subtraction. An integrated pattern of X-ray scattering for hydrogenated amorphous silicon is plotted after background subtraction.

A typical example of the substrate subtracted diffraction pattern for a-Si:H deposited at 300 °C for a single ψ tilt is shown in Fig. 5.3.

5.4 PEAK DIFFRACTION

After background subtraction, the data were analyzed using two procedures to study the full local structure of hydrogenated amorphous silicon. Firstly, the pair distribution functions were calculated as follows. The subtracted data was first converted to scattering interference function, *I(q)*, where the scattering vector, q, is related to the observed scattering angle, θ by $q=(4\pi/\lambda)\sin\theta$. The analysis of the data starts [19, 88, 89] with reduced scattering intensity

$$i(q)=\frac{I(q)}{Nf^2(q)}-1, \qquad 5.6$$

where f is the atomic form factor and N is the number of atoms in the samples. Next we normalize the data following the procedure described in [19]. A damping factor $\exp(-\gamma q^2)$ is introduced to reduce the errors in the high-q region due to the factor q^2. Using a Fourier transform of the function $qi(q)$, the pair distribution function (PDF) is estimated using the method discussed in chapter 4. The use of the term PDF is preferred here, instead of RDF, because it can longer be assumed that the structure is strictly isotropic. This function as explained earlier contains integral information about the amorphous structures [19, 83], namely preferred neighbour distances and means bond angles [1]. The peaks in the plot of PDF *vs* r correspond to the frequently occurring inter-atomic distances, and the area under the peaks is equal to the average number of atom pairs within the particular range of distance. Two distances were extended from the PDF*:* the position of the first peak which gives an estimate of the average first-neighbor distance r_1; and the position of the second peak estimates the average second-nearest neighbor distance r_2. In a-Si:H the nearest neighbour distance r_1 is directly equivalent to the Si-Si bond length. All the above

University of Cape Town

steps can be done using a numerical sine transform applied directly to the substrate subtracted data [20] or by fast Fourier transform as used in RAD program [69].

Secondly, using the same background subtracted XRD patterns, the strains along ψ directions were obtained directly from the first and second diffraction peaks of the hydrogenated amorphous silicon (a-Si:H) layers. To reduce the effect of random noise, the background subtracted XRD patterns were smoothed using a seven-point Savitzky-Golay algorithm using the Origin program. The diffraction peak shapes were approximated by Gaussian functions, and the fitted peaks positions were used to determine the interatomic separation *d*. In this procedure the diffraction peak positions were determined for the weighted centre of intensity of the reflections. Furthermore, the full widths at half maximum (*FWHM*) for the first two diffraction peaks were estimated from the diffraction patterns.

University of Cape Town

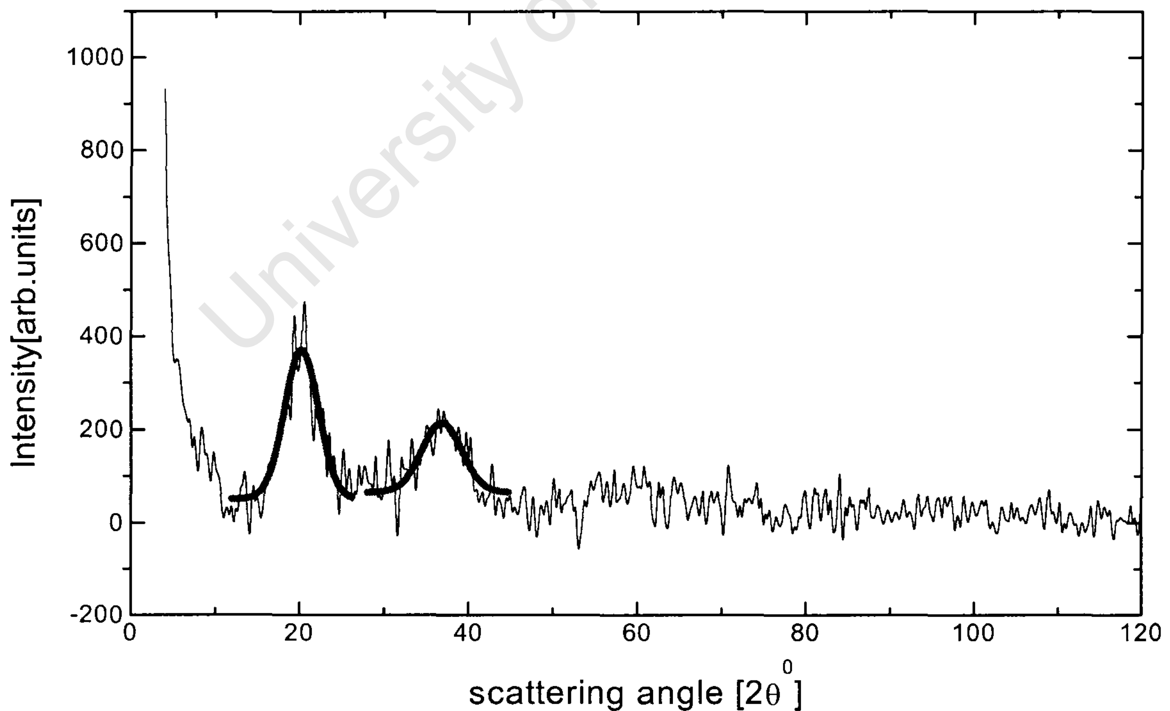

Fig. 5.4. Gaussian fitting of the amorphous diffraction patterns

Each diffraction peak is therefore described by Gaussian curve with variable FWHM and the intensity as shown in Fig. 5.4. Peak fitting was performed over a region of interest around the respective peak, in which the intensity had reduced to a background level without introducing any additional structures. The errors in the peak position were estimated using the FWHM by determining the error in the mean of the distribution [80]. From the counting statistics, the error is given by

$$\Delta(2\theta) = \frac{\sigma}{\sqrt{N}}. \qquad 5.7$$

This can also be rewritten as

$$\Delta\theta = \frac{\sigma}{2\sqrt{N}}. \qquad 5.8$$

Here σ is the standard deviation and N the integral intensity. This use of the integral intensity as N in the Breit-wegner formula makes the assumption that the background subtracted data really is Gaussian in form, and hence normally distributed. If this were not the case the counting statistics of the two measurements would have to be included in the same way. If we use the Breit-Wigner statistical distribution relationship, between the full width at half maximum (*FWHM*) and the standard deviation σ, defined by FWHM = $2\sigma\sqrt{2\ln 2}$, then the standard deviation σ can be expressed in terms of the full width at half maximum (*FWHM*), defined as

$$\sigma = \frac{FWHM}{2\sqrt{2ln2}}. \qquad 5.9$$

Substituting for σ back in Eq. 5.8 leads to

$$\Delta\theta = \left(\frac{FWHM}{4\sqrt{2Nl\,\mathrm{n}\,2}}\right), \qquad 5.10a$$

University of Cape Town

or $$\Delta\theta = 0.212\left(\frac{FWHM}{\sqrt{N}}\right) \qquad 5.10b$$

To find the error in the inter-atomic spacing *d*, Bragg's Eq. 5.1 is differentiated with respect to θ as described in chapter 4 and then the following equation is obtained:

$$\varepsilon = \cot\theta\Delta\theta \qquad 5.11$$

This equation indicates that the broadening of the diffraction peak depends on both strain and $\cot\theta$. Combining Eq. 5.10 and Eq. 5.11 leads to

$$\varepsilon = \left(\frac{\Delta d}{d}\right)_{\phi\psi} = 0.212\left(\frac{FWHM}{\sqrt{N}}\right)\cot\theta. \qquad 5.12$$

In determining the strain from the direct diffraction data the diffraction angles for the unstrained (111) and (220) crystalline silicon reflections were used, similarly in determining the strains from PDF's the crystalline silicon bond length and angles were used as a references.

University of Cape Town

6 RESULTS AND DISCUSSION

The overall aspects of structural features of a-Si:H layers in the present work were obtained using synchrotron radiation diffraction. The diffraction data have been analyzed using two distinct approaches. Firstly, a direct determination of the positions of the diffraction peaks [20], using a Gaussian fit to the data, was used to determine the interatomic separations. These were then converted to strain, which can be interpreted in terms of residual stress. Secondly, the microstructural characterization was performed using the radial distribution functions, for each ψ tilt, which were calculated using the substrate subtracted diffraction patterns. The details of the analysis procedures have been described in the earlier chapters.

University of Cape Town

6.1 DIFFRACTION PATTERNS IN q SPACE

Fig. 6.1 shows synchrotron diffraction patterns, taken for samples deposited at 300 $^{\circ}$C and 500 $^{\circ}$C, respectively. These spectra were measured at an arbitrary azimuth angle $\phi = 0$, and at zero ψ tilt. The results presented in Fig. 6.1 were generated after eliminating the contribution of the glass substrate following the procedure explained earlier in section 5.3. The subtracted data then converted to a scattering interference function, $I(q)$, where q is the magnitude of the scattering vector [19], which is related to the observed scattering angle, θ by $q = (4\pi / \lambda)\sin\theta$. This was performed using the following relation $I(\theta)d\theta = I(q)dq$. The diffraction patterns shown in Fig. 6.1 reveal the wave vector dependence of scattering intensity $I(q)$. It can be seen, that in both patterns, there are two clearly pronounced diffuse diffraction peaks at approximately 2 and 3.5 inverse angstroms. There is an indication of a third weak peak at 5.5 Å^{-1} but the scattering intensity is low at high q values. Practically

everywhere up to the measured maximum of 10 Å^{-1} there is a notable oscillating, diffuse and weak background.

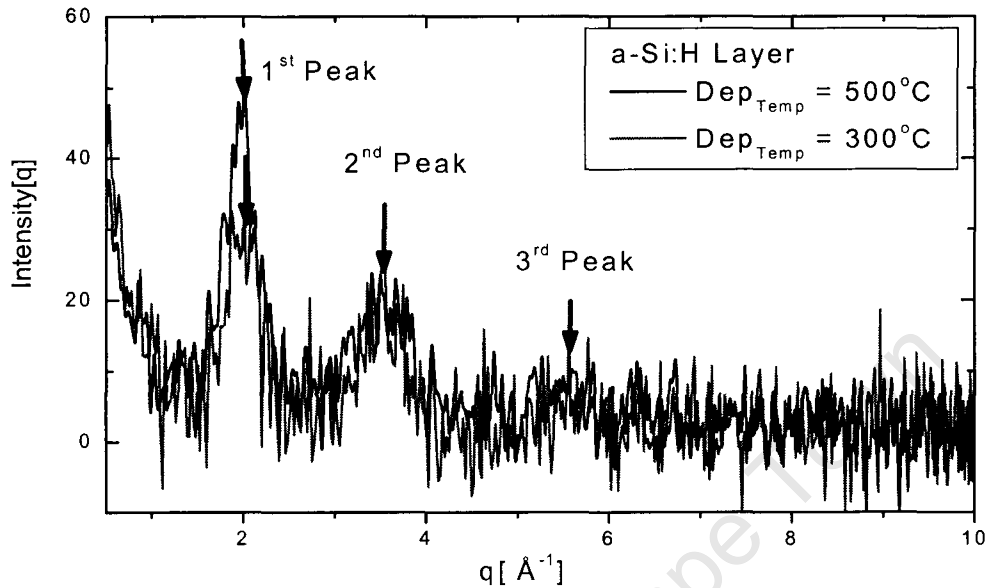

Fig. 6.1. Diffraction pattern from layers deposited at 300 °C and 500 °C measured at ψ = 0 and ϕ = 0.

The fact that the diffracted intensity is reduced at a high q value is a strong indication of short-range order, as opposed to long-range order, and thus presents evidence that the film structure is amorphous. As indicated by the insert in Fig. 6.2, for the sample deposited at 500 °C, the diffracted peak is equivalent to the (111) reflection in crystalline silicon (c-Si). The corresponding lattice spacing is equal to the height of the Si-Si_4 tetrahedron [26]. Similarly, the second diffraction peak is equivalent to the (220) reflection in c-Si, and corresponds to the length of side of the Si-Si_4 tetrahedron, as indicated in the insert of Fig. 6.2.

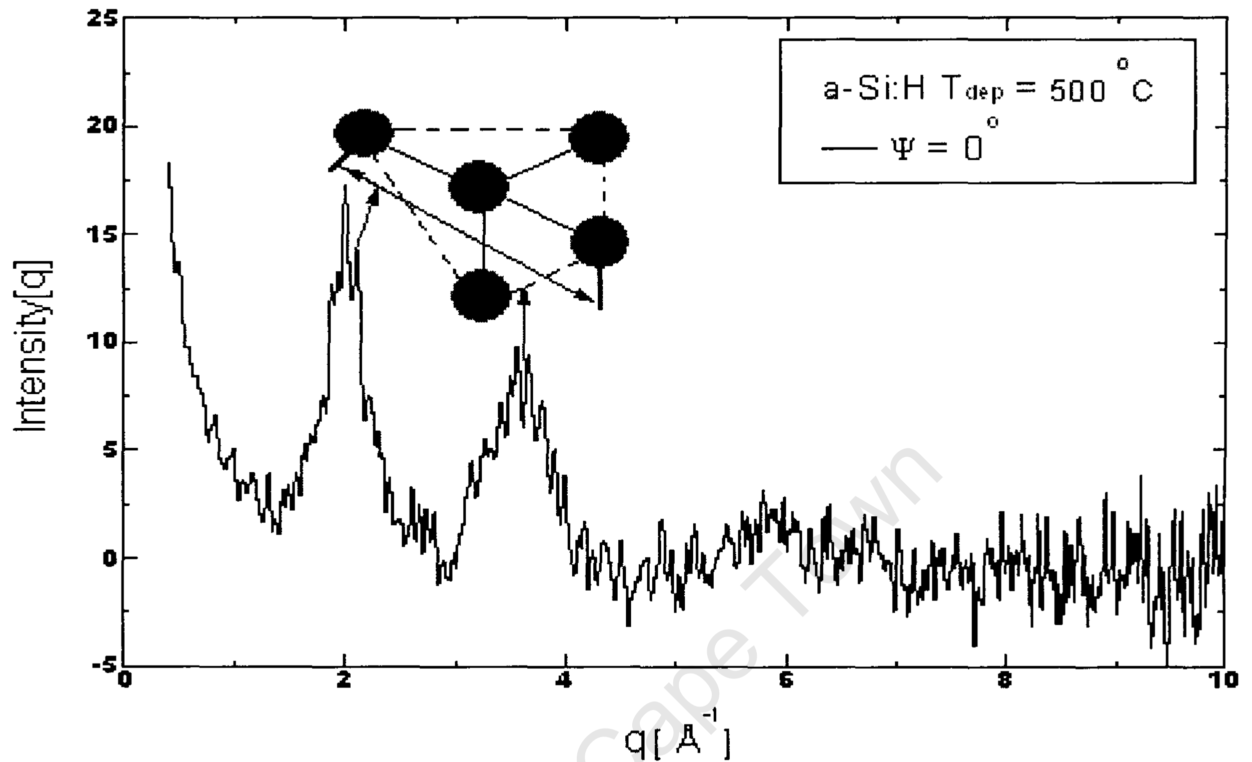

Fig. 6.2. Diffraction pattern showing the first two maxima in a-Si:H layer. The first peak corresponds to the height of the Si-Si_4 and the second peak corresponds to tetrahedron edge lengths of the Si-Si_4 tetrahedron, respectively.

University of Cape Town

Fig. 6.3 shows the diffraction peak shift for different ψ tilts for samples deposited at 300 °C and 500 °C, respectively. The first and the second peak positions shift towards a higher scattering vector *q*, for both samples. The relative intensity decreases as the ψ tilting increases. Each diffraction peak is directly related to the atomic distances through the diffraction condition, and the observed peak shift indicates a variation of interatomic spacing with direction ψ. As discussed in the previous chapters, any changes in the interatomic separations can be expressed as a strain $\varepsilon = \frac{\Delta d}{d}$ in the material.

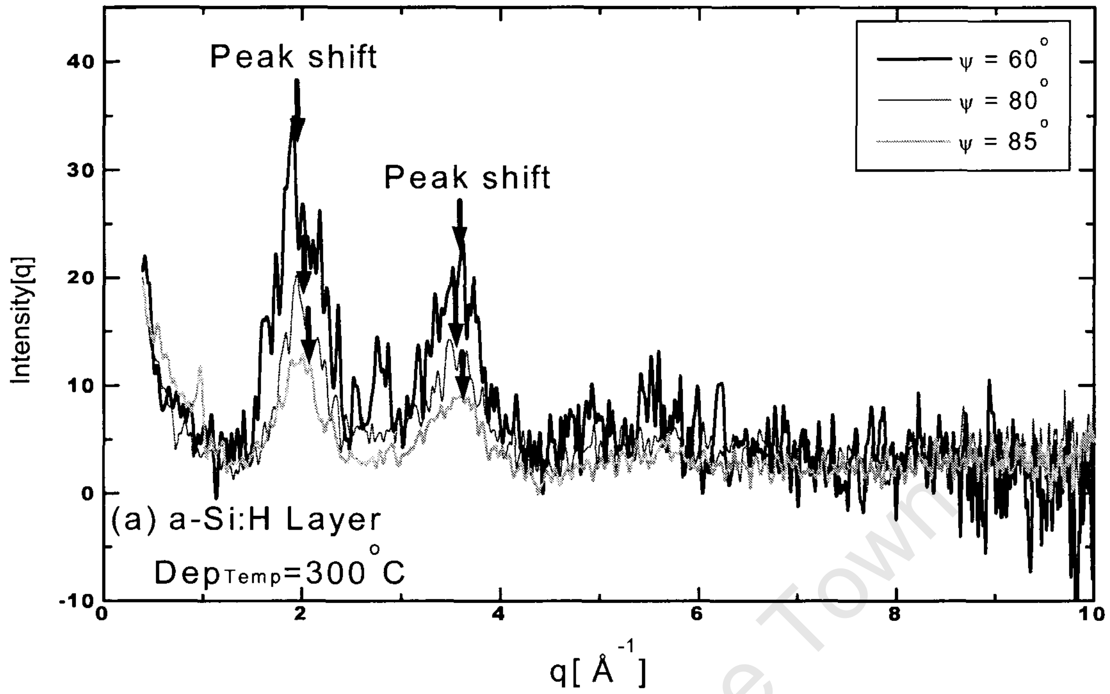

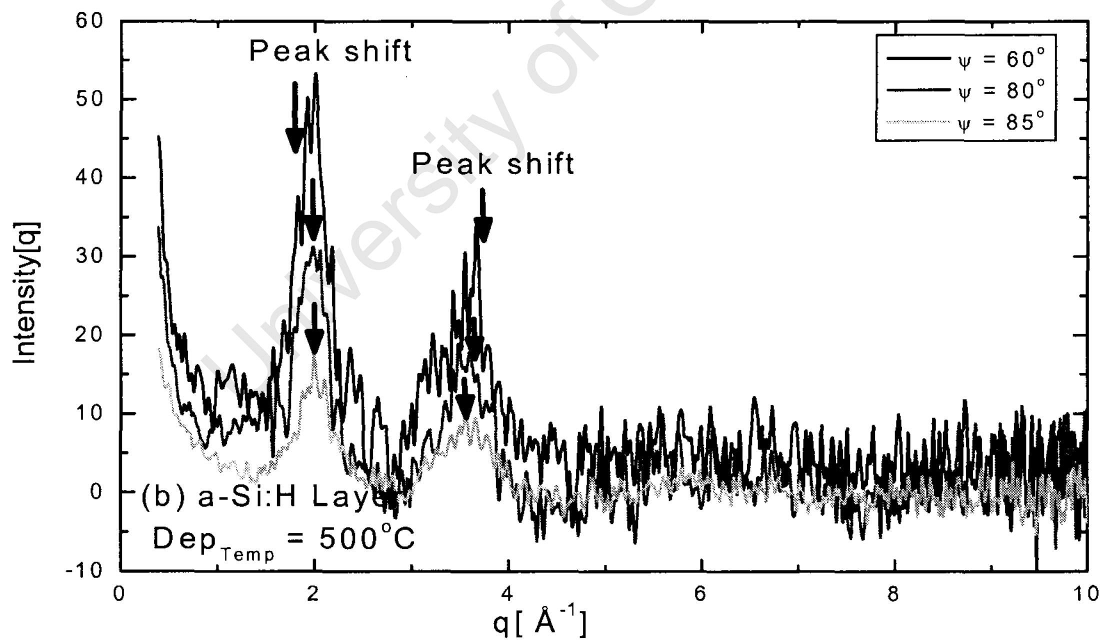

University of Cape Town

Fig. 6.3. The diffraction peak shift with ψ tilting in a-Si:H for two samples grown at (a) 300 °C and (b) 500 °C respectively. The displacement of the peaks, as indicated by arrows in both samples, is due to strain effect on layers.

6.2 DIFFRACTION IN REAL SPACE

In synchrotron diffraction, all we need to measure is the total structure function [19, 88, 89]. From this we obtain the real-space pair distribution functions (PDF) through Fourier transformation [89] according to the procedure described in section 5.4. This is also known as radial distribution function (RDF) and this function is equivalent to $4\pi r^2 \rho(r)$ as explained in chapter 4. The corresponding peaks of this function simply represent characteristic distances separating pairs of atoms, and thus reflect the atomic arrangement. As described in chapter 4, by analyzing its peaks and their shape information about the short and intermediate-range order in the material under study can be obtained.

Fig. 6.4 shows the corresponding pair distribution functions for the two growth temperatures as a function of correlation distance r from an arbitrary atom at its origin. It can be seen in the figure, that the pair distribution function for samples deposited at 300 $^{\circ}$C and 500 $^{\circ}$C both have two pronounced broad peaks. In both cases the peaks terminate with a ripple at larger correlation distances.

University of Cape Town

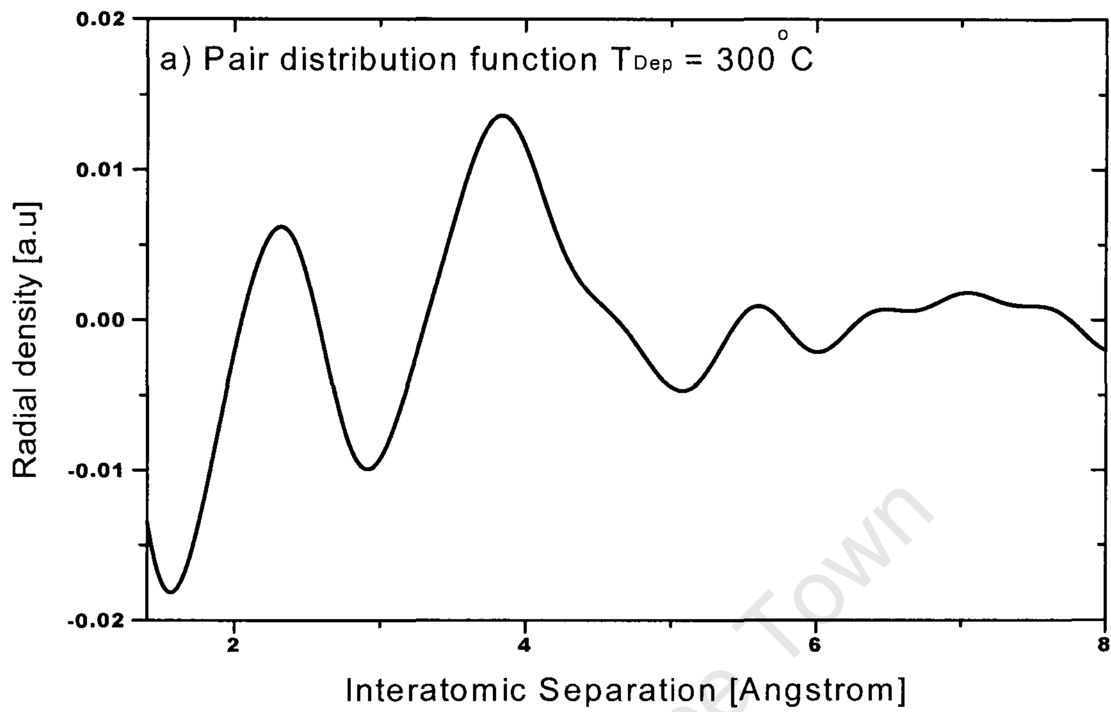

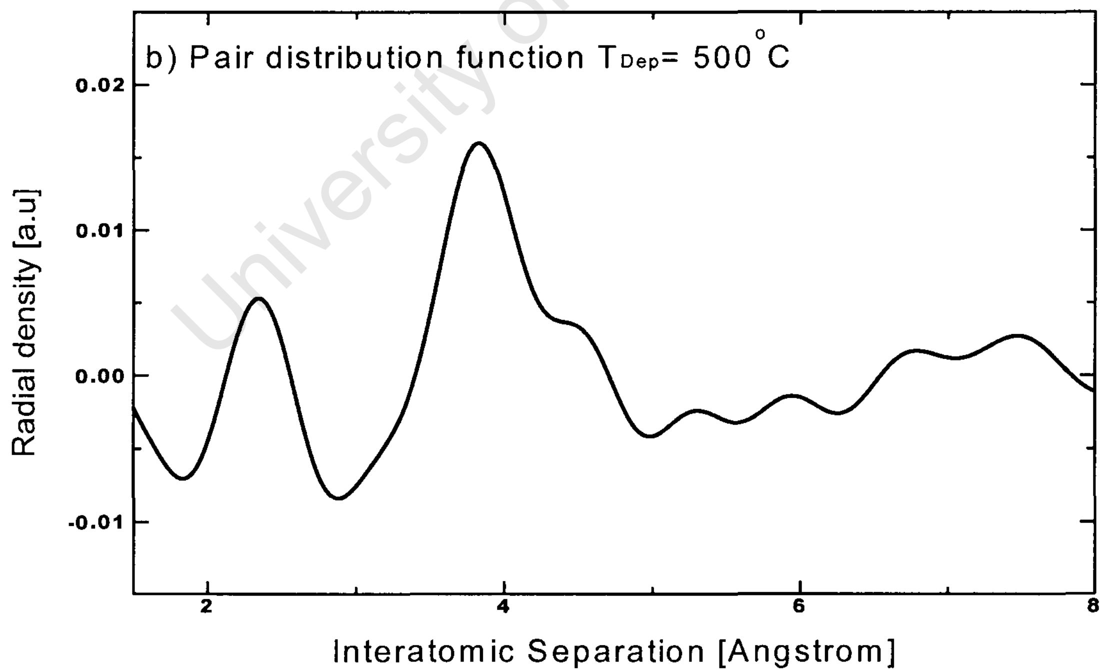

Fig. 6.4. Pair distribution function for a-Si:H layer (a) sample grown at 300 °C and (b) sample grown at 500 °C.

University of Cape Town

As described in chapter 4, the first peak corresponds to the first nearest-neighbour separation, and the second peak corresponds to the second nearest-neighbour separation. The first two peaks therefore correspond to the distances between the central tetrahedral atom and tetrahedron corners, and the tetrahedron edge length, respectively.

Fig. 6.5 shows, for comparison, the two curves for the samples deposited at 300 °C and 500 °C overlaid on each other.

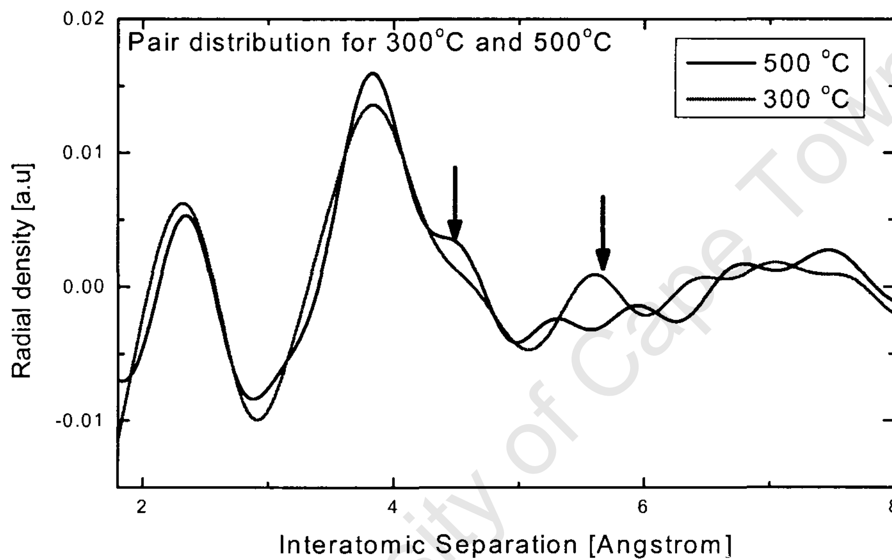

Fig. 6.5. Comparison of the pair distribution function for a-Si:H layers deposited at temperature of 300 °C and 500 °C.

University of Cape Town

The differences between the 300 °C and 500 °C films are most apparent within the first nearest neighbour distance, but are also apparent within the second nearest neighbour distance, as shown in Fig. 6.4 and Fig. 6.5. It can be seen that the corresponding patterns exhibit clear differences in the height and the width of the first peak, and the second peak. The most notable difference can also be seen in the form of a shoulder in the second peak for the sample deposited at 500 °C, as indicated by an arrow in Fig. 6.5. This shoulder could be due to a poorly resolved peak in the second maximum, or possibly the presence of hydrogen. It

may also indicate an increase in the short-range order in the layer for this sample. Further small differences are observed beyond the second peak for the sample deposited at 300 °C. There is a pronounced hump that looks like a third peak at a higher value of interatomic separation. This shows that most of the changes in atomic configurations result from ordering in the short range.

Further analyses on the PDF's for the first and second peaks were conducted on all curves for these samples at the respective growth temperature. These were then used to obtain the interatomic distances or bond length in different directions for each PDFs. Results obtained for both 300 °C and 500 °C samples measured at $\phi = 0$ are summarized in table 6.1. A more complete set of these data is included in appendix A.

Table. 6.1 An interatomic spacing r_1 and r_2 in Å, and the bond angle for two samples at different ψ tilts and $\phi = 0$.

	Deposition temperature 300 °C			Deposition temperature 500 °C		
ψ - tilt	r_1(Å)	r_2(Å)	α (°)	r_1(Å)	r_2(Å)	α (°)
0 °	2.29 ± 0.009	3.89 ± 0.02	116.3 ± 1.0	2.38 ± 0.01	3.92 ± 0.03	110.9 ± 1.0
20 °	2.24 ± 0.006	3.98 ± 0.02	125.3 ± 0.9	2.34 ± 0.01	3.90 ± 0.02	113.1 ± 0.8
40 °	2.39 ± 0.004	3.84 ± 0.02	106.9 ± 0.8	2.20 ± 0.01	3.96 ± 0.01	128.5 ± 0.9
60 °	2.41 ± 0.006	3.94 ± 0.02	109.7 ± 1.1	2.25 ± 0.01	3.93 ± 0.02	121.2 ± 0.8
80 °	2.39 ± 0.04	3.92 ± 0.01	110.2 ± 1.0	2.23 ± 0.02	3.85 ± 0.01	119.4 ± 0.9
85 °	2.35 ± 0.01	3.91 ± 0.02	112.6 ± 0.9	2.29 ± 0.02	3.88 ± 0.02	116.1 ± 1.2

It is clear from the tabulated data that there are several trends observed for both samples. The tabulated values for samples deposited at 300 °C and 500 °C reveal that the bond length ranges from 2.2 Å to 2.41 Å for the first nearest neighbour. Similarly, the second nearest neighbour distance ranges from 3.84 Å to 3.98 Å. These values are close to the Si-Si bond length of 2.34 Å and second nearest neighbour distance of 3.85 Å found in the crystalline structure [1, 19, 88]. The angles between the bonds for the amorphous sample deposited at 300 °C are between

University of Cape Town

106.9°and 125.3° and that of the sample deposited at 500 °C are between 110.9° and 128.5°. This indicates that the structural parameters are not that different from the crystalline material. Further observation reveals that there is a general increase in the nearest-neighbour separation perpendicular to the surface, and a decrease in second-nearest neighbour separation, with deposition temperature. These characteristics indicate the bond distortion as result of strain. The evidence of peak shifts due to strain in both peaks can be seen in Fig. 6.6, indicated by the three arrows at various ψ tilts. Similar behaviors are apparent for other ϕ angles as can be seen in the curves included in appendix C for both samples.

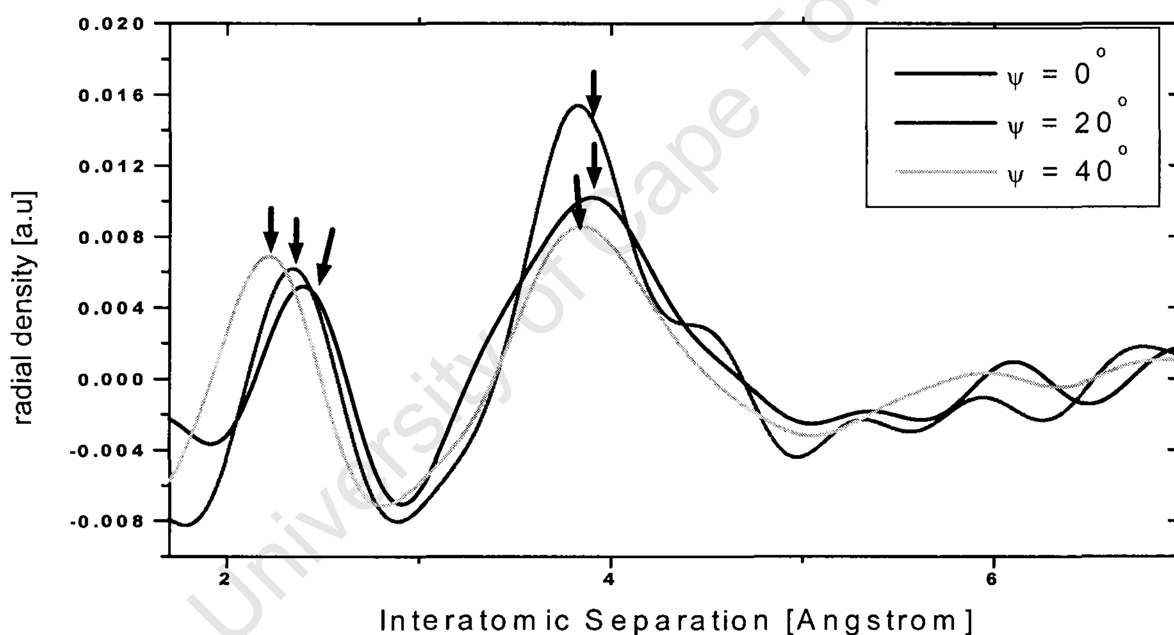

Fig. 6.6. The variation of the nearest-neighbour and second nearest neighbour separations for a-Si:H grown at 500 °C growth at $\phi = 0$ for tilts of $\psi = 0°, 20°, 40°$. The pattern exhibits a peak shift as indicated by the arrows.

Similar observations were noticed in a study done earlier in ref [23]. In this study the authors concluded that this is an indication of a widening of the average bond angles and a shortening of the bond length, but no clear justification of the cause was given. However, Street [88],

attributes this to bond strains, and hence the disorder in a-Si:H network, and more recently the same argument was confirmed in the study by Härting *et al* [20].

6.3 THE VARIATION OF STRAIN

The synchrotron diffraction patterns presented in Fig. 6.1 and the PDF curves in Fig. 6.4, were used to extract information on the strain in the a-Si:H layers of the samples deposited at 300 °C and 500 °C. To reduce the effect of random noise and at the same time to get the best estimate of the peak maxima from the distorted data, the substrate-subtracted 2Θ diffraction data were first smoothed using a seven-point Savitzky-Golay algorithm as described in section 5.4. For this purpose, the position of the peaks is determined as the centre of a Gaussian distribution fitted to the smoothed diffraction peaks as shown in Fig. 6.7. Similarly, in order to obtain peak information from the PDF, such as peak widths and peak positions, the real-space functions, are fitted with Gaussian distributions but no further smoothing procedure was applied. The Gaussian fit was chosen over other common peak fitting methods, such as centre of gravity, because the diffraction peaks in this work are broad and almost Gaussian in shape. Fig. 6.7 shows an example of the typical diffraction peaks used for strain measurement. To convert from peak positions to strain, we have used the fact that the first diffraction peak, corresponding to the height of the Si-Si_4 tetrahedron, is equivalent to the (111) reflection in c-Si [2, 56, 62]. Similarly, the second diffraction peak, corresponding to the length of side of the Si-Si_4 tetrahedron is equivalent to the (220) reflection in c-Si.

University of Cape Town

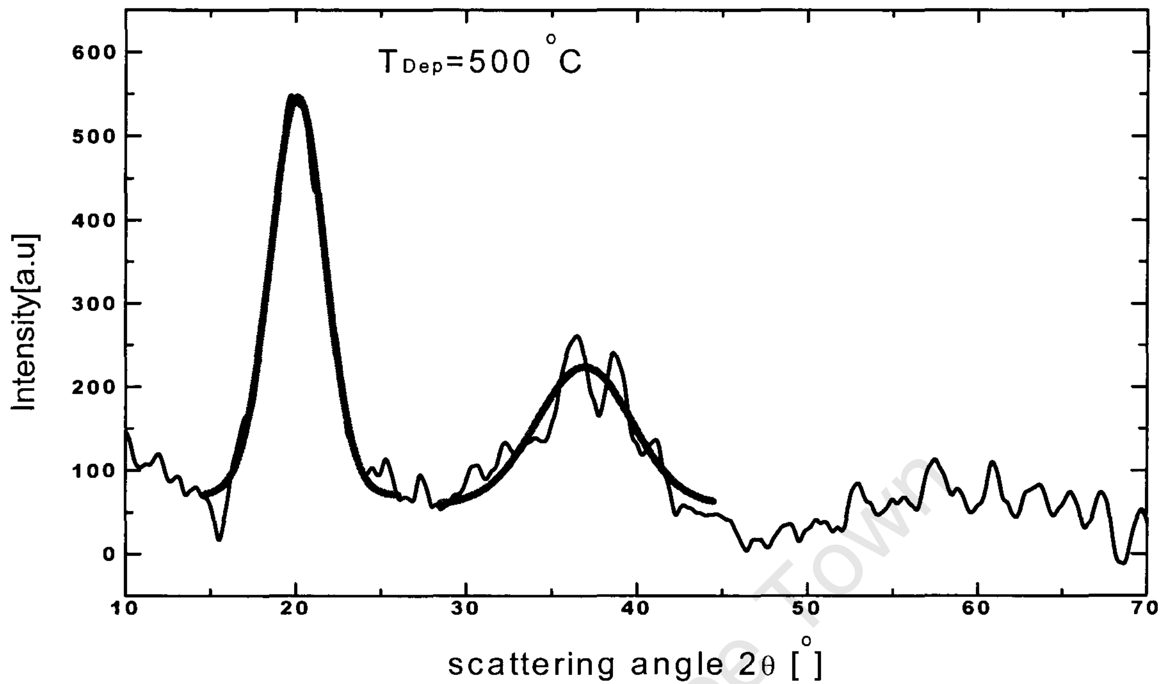

Fig. 6.7. The diffraction pattern after smoothing with a 7-point smoothed Savitzky-Golay algorithm. The bold line represents a fitted Gaussian curve for peak position, and FWHM estimation.

Crystalline silicon has been used as a reference to obtain strain from diffraction and pair distribution function (PDF) peak positions. To perform this calculation, we have used the lattice spacing of 3.1355 Å, and 1.9102 Å for the (111) and (220) planes of c-Si as reference values for the 2Θ diffraction data. Similarly crystalline values of 2.34 Å and 3.85 Å were used as reference values to determine bond strain from the pair distribution function. The strain conversion was then carried out according to the procedure outlined in section 4.8.

University of Cape Town

6.3.1 STRAIN DETERMINED FROM 2Θ DIFFRACTION PATTERN

The detailed information extracted from the first two diffraction peaks for samples grown at 300 °C and 500 °C are summarized in table 6.2(a) and (b) .

Table. 6.2. (a) and (b). Peak position parameters and information for variation of strain from diffraction as a function of 2Θ in a-Si:H layer at 300 and 500 °C

Strain for a-Si:H deposited at 300 °C determined from diffraction patterns					
First diffraction peak *(111)*			Second diffraction peak *(220)*		
2θ [°]	*FWHM*	Integral intensity	2θ [°]	FWHM	Integral intensity
20.364	3.9172	1331	36.729	4.6787	1042
20	7	2231.744	36.526	8.844	2378.9
20.25	5	2120.1734	36.603	5.9924	1346.5
20.234	5.1407	1600	36.913	5.5137	1159.8
20.547	3.8071	613.79	36.913	3.9173	360.89
20.339	4.2217	504.89	36.872	5.1908	409.09

Strain for a-Si:H deposited at 500 °C determined from diffraction patterns					
First diffraction peak *(111)*			Second diffraction peak *(220)*		
2θ [°]	*FWHM*	Integral intensity	2θ [°]	FWHM	Integral intensity
20.251	3.4029	1620.2	36.448	7.409	1613.3
20.097	3.145	1859.7	36.925	5.3427	1073.8
20.3	2.9364	1460.2	36.947	6.532	1713.7
20.292	2.6823	842.27	37.07	5.1689	1115.9
20.608	3.46	570.62	37.161	6.8488	843.66
20.503	3.2017	247.01	36.816	6.7336	486.94

University of Cape Town

This information was converted to strains using the linear $\varepsilon_{\varphi\psi}$-$\sin^2\psi$ relationship, using the procedure outlined in chapter 4. Typical results for the variation of strain with $\sin^2\psi$ in the *a*-Si:H layer are presented in Fig. 6.8 (a) and (b) for the sample grown at 300°C.

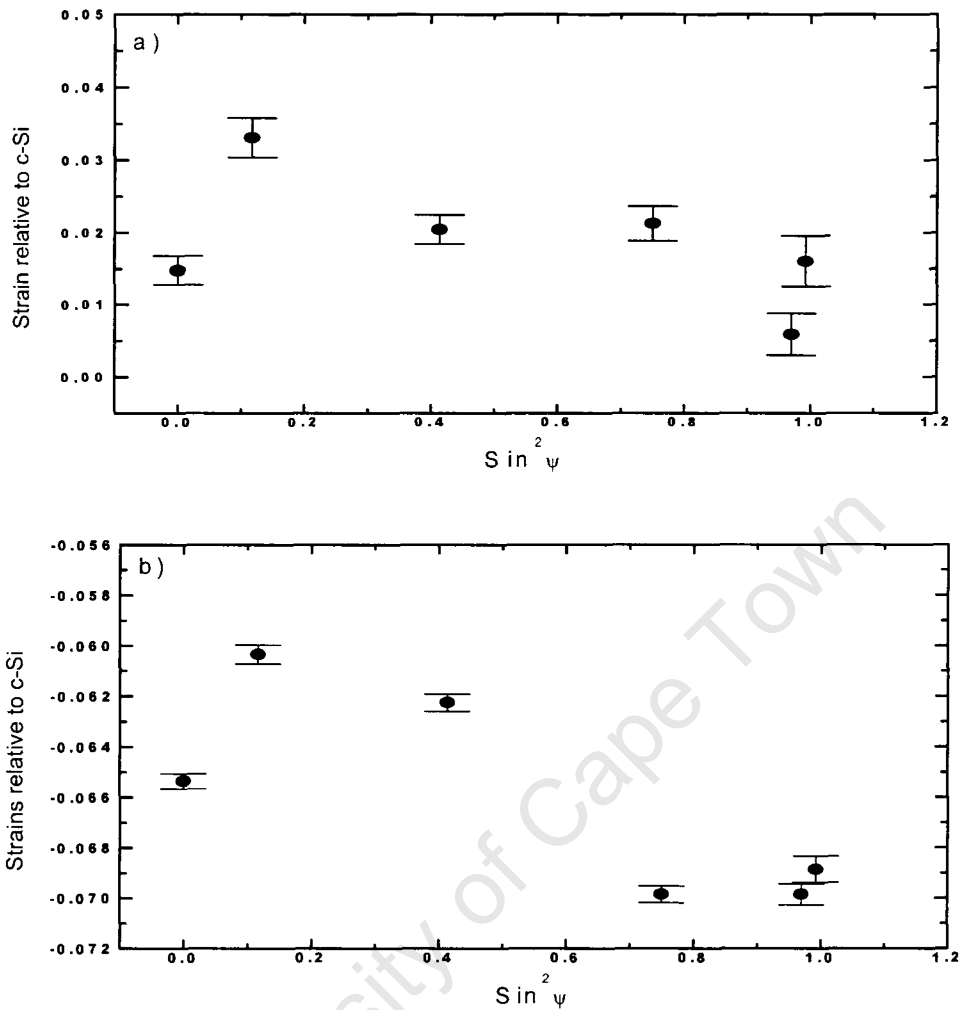

University of Cape Town

Fig. 6.8. Variation of the strain with $\sin^2\psi$ for the a-Si:H layer deposited at 300°C determined from diffraction pattern: (a) first diffraction peak corresponding to the height of the Si-Si_4 tetrahedron, equivalent to the (111) reflection in c-Si (b) the second diffraction peak, equivalent to the (220) reflection in c-Si, corresponding to the length of side of the Si-Si_4 tetrahedron.

Similarly, the results for the variation of strain with $\sin^2\psi$, as determined from the positions of the first and second diffraction peaks, for the sample grown at 500 °C are presented in Fig. 6.9 (a) and (b). It is very clear from the curves shown in Fig. 6.8 and Fig. 6.9 that for both samples, the curves deviate from the linear prediction of the conventional $\sin^2\psi$ method. This indicates the presence of a stress gradient, and hence shear components, which are also evident in the difference between $\sin^2\psi$ curves taken for ϕ angles 180° apart, as seen in the appendix.

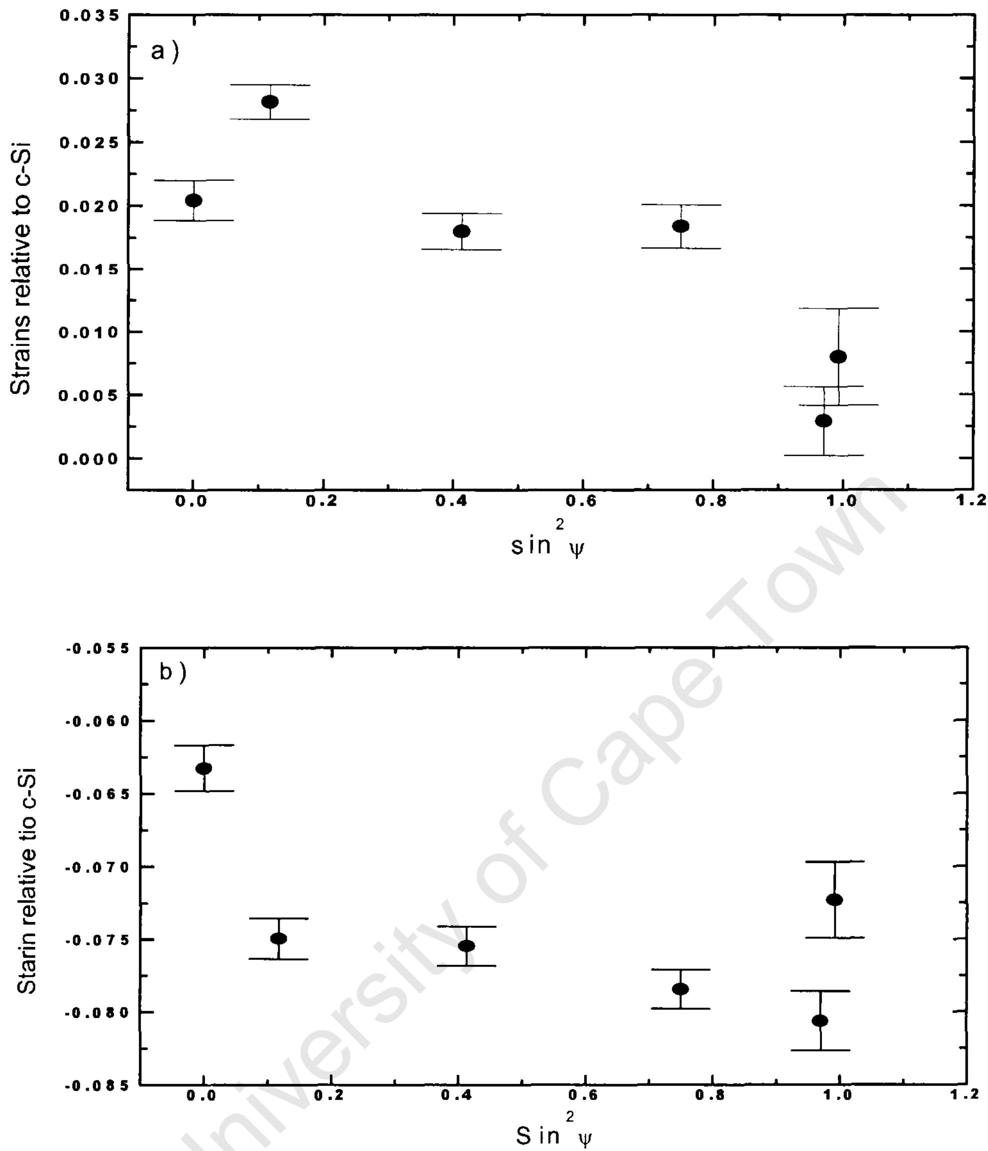

Fig. 6.9. Variation of the stain with $\sin^2\psi$ for the a-Si:H layer deposited at 500°C determined from diffraction pattern: (a) first diffraction peak corresponding to the height of the Si-Si_4 tetrahedron, equivalent to the (111) reflection in c-Si, (b) the second diffraction peak, equivalent to the (220) reflection in c-Si, corresponding to the length of side of the Si-Si_4 tetrahedron.

Similar behavior was also observed for other azimuth angles ϕ, for both samples, as can be seen in the data included in appendix B. It should be noted that there is some slight discrepancy between corresponding measurements, e.g. $\phi = 0°$ and $\phi = 180°$, but in general

University of Cape Town

these agrees to within two standard deviations using the error estimates described by Eq.5.8. There are several reasons for these differences including; inhomogeneity in layer thickness, error propagation in background subtraction, and possible misalignment of the diffractometer axes. Furthermore, the curves plotted in Fig. 6.8 and Fig. 6.9, and those included in the appendix are largely dominated by negative slopes, indicating a compressive stress. The non-linearity presumably results from the strain gradient through the thickness on *a*-Si:H layer [70], and indicates an inhomogeneous stress distribution within the layer. A similar behavior was also observed in ref [15] for a-Si:H layers deposited under similar conditions, and more recently in a work done in ref [20].

6.3.2 STRAIN DETERMINED FROM PAIR CORRELATION FUNCTION

Typical examples of bond strain plotted relative to c-Si as a function of $\sin^2\psi$ for two samples deposited at temperatures of 300 °C and 500 °C are shown in Fig. 6.10 (a) and (b). As described in section 6.3, the bond strains occur as a result of an increase and decrease of nearest neighbour and second nearest-neighbour distances. This behavior is attributed to the bonding distortion at the sites of the amorphous silicon network. This effect, as we know, may induce bond strain in the network resulting from broken Si-Si bonds, and hence the formation of dangling bonds. This is due to the atomic hydrogen that diffuses into the amorphous network and converts strained Si-Si bonds into Si-H bonds. Furthermore, for both samples, assuming a linear dependence, the slope of the $\sin^2\psi$ in Fig. 6.10 (a) and (b) indicates a change from tensile bond strain at 300 °C to compressive stress at 300 °C grouth temperature. Similar characteristics can also be noticed for other curves (see appendix C). The origin of this effect is assumed to be due to bond relaxation as the growth temperature increases.

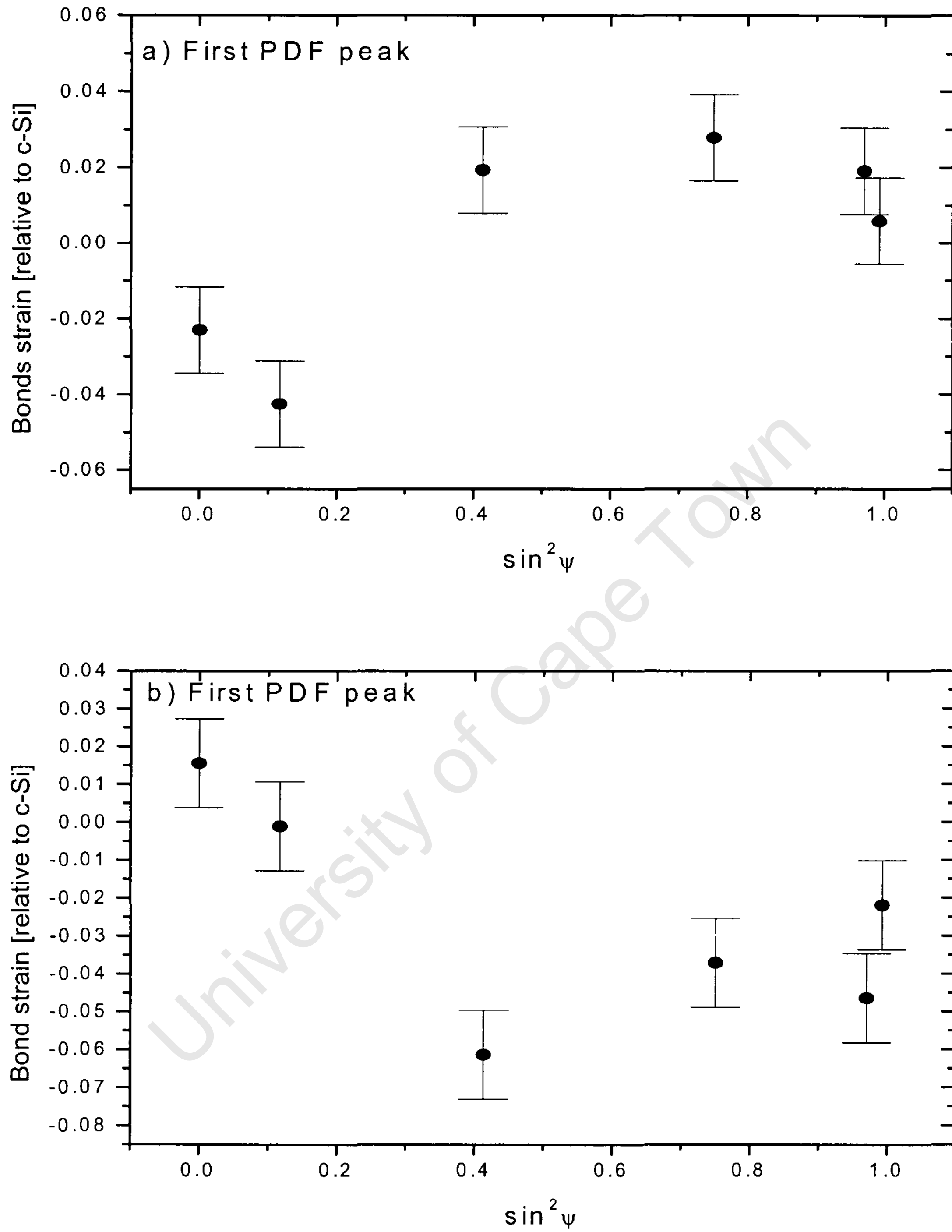

University of Cape Town

Fig. 6.10. Variation of bond strain determined from nearest neighbour separation in the pair correlation function: (a) a-Si:H layer deposited at 300°C and (b) a-Si:H layer deposited at 500°C

Similar evidence of this behavior can be seen clearly in the data in table 6.1 (see page 55) for different ψ tilts. In the case of ϕ = 0 as seen in table 6.1, the mean bond angles vary from 109.7 ± 1.1 to 125.3±0.9 degrees for the sample grown at 300 °C, and between 110.9 ± 1.0 to 128.5 ± 0.9 degree for the sample grown at 500 °C. This clearly indicates that there is a shift in the PDF peaks, as can be seen in Fig. 6.6 above. It is also interesting to note that there is a general decrease in the bond angles as the growth temperature increases. More generally, the bond strain in Fig. 6.10 reveals that the stress states in a-Si:H layers are consistent with the growth process, and deposition temperature, and that the nearest neighbour separation and bond angle strongly depend on the deposition temperature.

6.3.3 DETERMINATION OF RESIDUAL STRESS

The strain to stress convention for $\sin^2\psi$ curves obtained from both 2Θ diffraction data and pair distribution function (PDF) was achieved using the procedure outlined in Section 4.28.

The $Slope = \frac{\partial \varepsilon_{\varphi\psi}}{\partial Sin^2\psi}$, was estimated using a linear fit to the strain curve as indicated in Fig. 6.11. The detailed information from the slope estimated from the $\sin^2\psi$ curve for samples deposited at 300 °C and 500 °C are summarized in table-A and table-B (see appendix D).

University of Cape Town

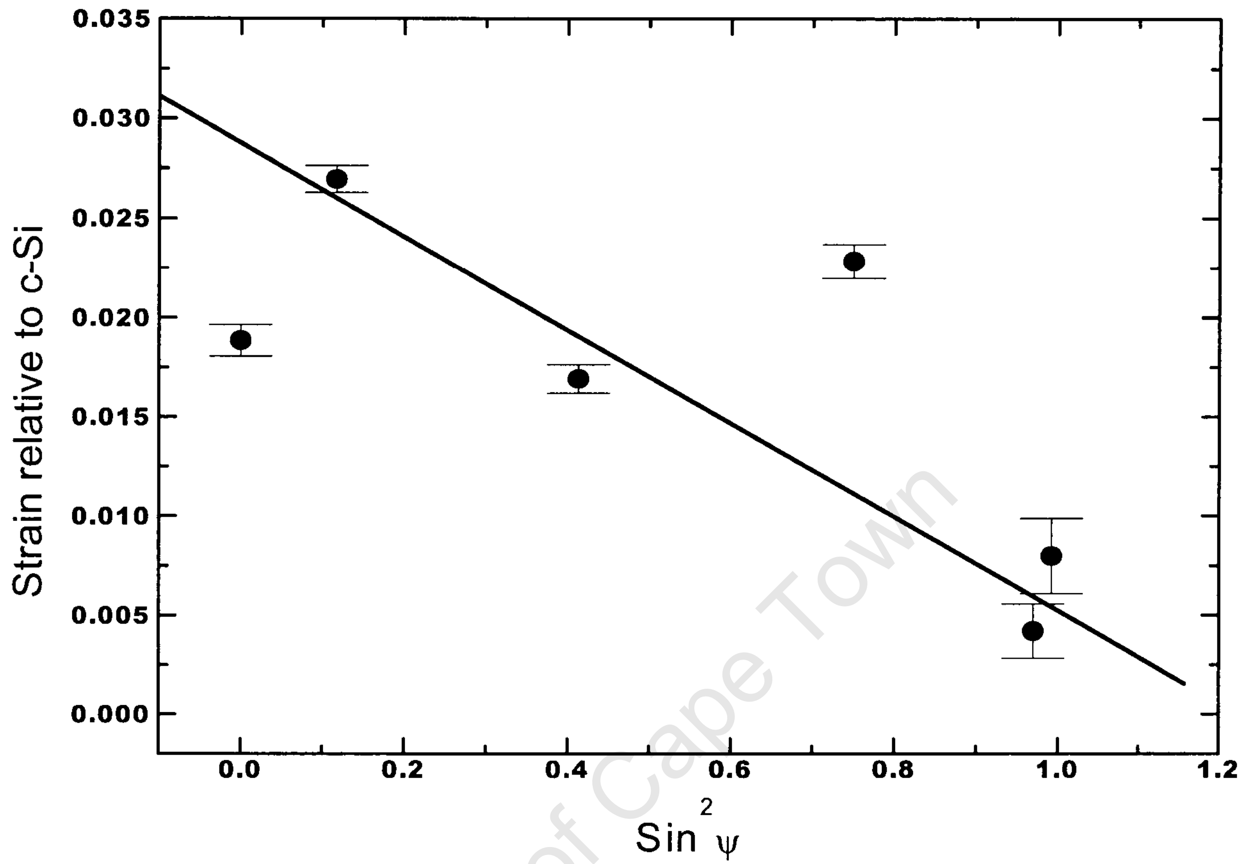

Fig. 6.11. Linear fit of strain as a function of $\sin^2\psi$ for sample 500 °C.

University of Cape Town

The residual stress and its components were estimated by equating the slope to $\frac{1}{2}S_2\sigma_\phi$, using the material constants ($E=100GPa$ and ν = 0.25GPa) expected for a-Si:H grown under similar conditions [15, 81, 82]. The resulting residual stresses in GPa for both 2Θ diffraction data and PDFs are summarized in table 6.3 and 6.4, respectively.

Table 6.3: Residual stress in *GPa* obtained from a-Si:H layer for samples deposited at 300 °C and 500 °C using direct diffraction peak shifts

Azimuth angle ϕ in degrees	Residual stress in *GPa* for sample deposited at 300 °C	
	1st diffraction peak at (111)	2nd diffraction peak at (220)
0	-0.48 ± 0.25	-0.56 ± 0.18
60	-2.10 ± 0.25	-0.30 ± 0.18
120	-1.09 ± 0.25	-0.85 ± 0.18
180	-1.40 ± 0.25	-0.89 ± 0.18
240	-1.07 ± 0.25	-1.58 ± 0.18
300	-0.46 ± 0.25	-1.06 ± 0.18

Azimuth angle ϕ in degrees	Residual stress in *GPa* for sample deposited at 500 °C	
	1st diffraction peak at (111)	2nd diffraction peak at (220)
0	-0.85 ± 0.2	-0.83 ± 0.15
60	-1.24 ± 0.2	-0.59 ± 0.15
120	-1.62 ± 0.2	-0.79 ± 0.15
180	-1.75 ± 0.2	-1.18 ± 0.15
240	-2.2 ± 0.2	-0.46 ± 0.15
300	-1.90 ± 0.2	-0.10 ± 0.15

University of Cape Town

The corresponding residual stress varies from 0.46 ± 0.25 to 2.10 ± 0.25 GPa for the first diffraction peak, and 0.3±0.18 to 1.58±0.18 GPa for the second diffraction peak at the growth temperature of 300 °C. Similarly, the residual stress for the sample grown at 500 °C varies from 0.85 ± 0.2 to 2.2 ± 0.2 GPa for the first diffraction peak, and from 0.1 ± 0.2 to 1.8 ± 0.2 GPa for the second diffraction peak. Negative values for both samples in tables 6.3, indicate that the layers are under compressive stress, and reflect the negative slope of the $\sin^2\psi$ curve. It is also noted that the stress increases with an increase in deposition temperature.

The residual stress values obtained from nearest neighbour separation PDF are summarized in table 6.4.

Table 6.4: Residual stress in *GPa* obtained from a-Si:H layer for samples deposited at 300 °C and 500 °C using direct PDF peak shifts

Azimuth angle ϕ in degrees	Residual stress in *GPa* from PDF for sample deposited at 300 °C	
	1st PDF peak at (111)	2nd PDF peak at (220)
0	3.87 ± 0.5	-0.16 ± 0.2
60	2.56 ± 0.5	-0.17 ± 0.2
120	1.55 ± 0.5	0.32 ± 0.2
180	1.25 ± 0.5	-0.472 ± 0.2
240	2.30 ± 0.5	-0.16 ± 0.2
300	0.33 ± 0.5	-0.81 ± 0.2

Azimuth angle ϕ in degrees	Residual stress in *GPa* from PDF for sample deposited at 500 °C	
	1st PDF peak at (111)	2nd PDF peak at (220)
0	-3.22 ± 0.5	-0.11 ± 0.2
60	-3.19 ± 0.5	0.04 ± 0.2
120	-2.94 ± 0.5	-0.88 ± 0.2
180	-3.70 ± 0.5	-0.73 ± 0.2
240	-0.67 ± 0.5	-1.42 ± 0.2
300	-4.34 ± 0.5	-1.15 ± 0.2

The sample deposited at 300 °C reveals two noticeable stress characteristics. Firstly, the nearest neighbor separation obtained from the PDF is under tension, with the stress varying between 0.33 ± 0.5 and 3.87 ± 0.5 GPa. Secondly, except for one value obtained at azimuth angle ϕ corresponding to 120°; the stress value for the second nearest neighbor peak is compressive. The residual stress obtained from the second peak varies between 0.16 ± 0.2 and 0.81 ± 0.2 GPa. Looking at the residual stress values obtained for the sample deposited at 500 °C, one can clearly see from the results summarized in table 6.4, that the overall residual stress for the first two pair distribution function peaks is compressive. Typical stress values obtained from the first peak range between 0.67 ± 0.5 and 4.34 ±0.5 GPa, and that obtained from the second peak varies from 0.11 ± 0.2 to 1.15 ± 0.2 GPa. As can be seen from table 6.4, the comparison between two samples shows a striking difference in their respective first PDF peaks. The observed stress values change from tensile to compressive as the temperature

University of Cape Town

increases from 300 °C to 500 °C. This argument confirms the trend observed in Fig. 6.10 above, and the same trend is noticed for all other stress curves at different azimuth angles (see appendix C). In light of this, we can conclude that the bond strain for the sample grown at 300 °C is under tension. This observation is consistent with the findings reported in [20]. Subsequently, the observed residual stress values for the second PDF peak in both samples reveal contrary features when compared to the trend observed for the first PDF peak, *i.e* the layer is under compressive stress. The latter argument may originate from distorted Si-Si bonds and possibly the stress relaxation as the temperature increases. These views are in agreement with the observations seen in table 6.3 for the results obtained from direct diffraction peaks.

Further analysis of the samples is carried out to get the biaxial stress in the a-Si:H layers. To achieve this we use the following equation: $\sigma_{\phi} = \sigma_{11}\cos^2\phi + \sigma_{12}\sin 2\phi + \sigma_{22}\sin^2\phi$. The detailed derivation of this equation is described in chapter 4. To apply this equation we use the data given in table 6.3 and 6.4, respectively. The information from this equation allows us to calculate the unknown stress components from both first and second a-Si:H peaks, namely, σ_{11}, σ_{22} and $\sigma_{12} = \sigma_{21}$. It should be noted that solving this equation for σ_{11}, σ_{12} and σ_{22} automatically defines σ_{11} as the stress determined for $\phi = 0$, and does not make full use of the data set as would be done by a non-linear fit. Tables 6.5 and 6.6 summarize the typical biaxial stress values obtained from 2Θ diffraction and pair correlation function peaks for samples deposited at 300 °C and 500 °C, respectively.

University of Cape Town

Table 6.5: Biaxial stress state in *GPa* obtained from a-Si:H layer for samples deposited at 300 °C and 500 °C obtained using 2Θ data.

	Sample deposited at 300 °C	
Biaxial state in GPa	First Peak (111)	Second peak (220)
σ_{11}	-0.48	-0.56
σ_{22}	-1.97	-0.58
$\sigma_{12} = \sigma_{21}$	-0.58	0.38

	Sample deposited at 500 °C	
Biaxial state in GPa	First Peak (111)	Second peak (220)
σ_{11}	-0.85	-0.83
σ_{22}	-1.623	-0.643
$\sigma_{12} = \sigma_{21}$	0.219	0.116

Table 6.6: Biaxial stress state in *GPa* obtained from a-Si:H layer for samples deposited at 300 °C and 500 °C obtained using pair correlation function

	Sample deposited at 300 °C	
Biaxial state in GPa	First Peak (111)	Second Peak (220)
σ_{11}	3.87	-0.16
σ_{22}	1.46	0.153
$\sigma_{12} = \sigma_{21}$	0.153	-0.279

	Sample deposited at 500 °C	
Biaxial state in GPa	First Peak (111)	Second peak (220)
σ_{11}	-3.22	-0.11
σ_{22}	-3.02	-0.523
$\sigma_{12} = \sigma_{21}$	-0.139	0.531

University of Cape Town

The stress values in the plane of the a-Si:H layer *i.e.* σ_{11} for sample deposited at 300 °C, is found to be -480 MPa and -560 MPa for the first and the second diffraction peak, respectively. However, the stress values in the plane of the layer for sample deposited at 500 °C changes from -850 MPa to -830 MPa for the first and second diffraction peaks, respectively. This indicates that the stress in the layer changes with deposition temperature, and this is a clear

indication that the microstructure in a-Si:H layer are tightly controlled by deposition processes. These findings are similar to the work published previously [23], which showed a similar relaxation of bond lengths and increase in bond angle with deposition temperature. The same authors also reported a decrease in free volume defects associated with this relaxation. However, the stress values in the plane of the a-Si:H layer obtained using pair correlation functions show a different behavior as compared to the stress values obtained from 2Θ diffraction peaks. Typical residual stress calculated for sample deposited at 300 $^{\circ}$C has a high value of 3870 MPa for the first PDF peak and this value changes rapidly to -160 MPa for the second peak. In contrast, the stress values for sample deposited at 500 $^{\circ}$C have a negative value for both the first and the second PDF peak, respectively. This behaviour is consistent with the assumption, that the strain in the bond angles dominates the overall strain, and the fact that the bond strain obtained from PDF for the sample grown at 300 $^{\circ}$C, is under tension.

University of Cape Town

7 CONCLUSION

Synchrotron diffraction techniques have been used to investigate the microstructure, and the residual stress for a-Si:H samples deposited at 300 °C and 500 °C. This work was motivated by the need to determine the structural coordination, the degree of order in the CRN, its local distribution and corresponding residual stress in hydrogenated amorphous silicon, and its correlation with physical properties.

It is well known from general diffraction theory [19] and reviews of amorphous semiconductors [1, 2, 88] that the main structural characteristic of amorphous silicon should be two broad diffuse diffraction peaks. This is consistent with the characteristics observed for the two samples under study in this work. Therefore, it can be suggested that these samples are really amorphous silicon. The relative intensities of the components in the first and second diffraction peaks vary strongly with an increase in ψ angle for both samples. We have noticed that the diffraction patterns for both samples are primarily the same with notable differences in the height, and the width of the first, and second peaks. The diffraction patterns show that there is a diffraction peak shift as the tilt angle increases. This is as a result of the strain in the material.

The information extracted from the pair correlation function, reveals that there are two broad peaks and progressively less well-defined peaks at larger distances. This character reflects a common property of amorphous materials. There is a degree of short-range order at the first and second neighbour distances, but the spatial correlations decrease rapidly (*i.e.*

University of Cape Town

the third peak disappears in the measured PDF). The absence of the third PDF peak confirms that there is no characteristic dihedral angle, *i.e.*, the angle between second neighbour bonds. Both samples have a Si-Si nearest neighbour distance of approximately 2.345 Å and the Si-Si-Si angle of about 109.5°. The observed PDF curves for both samples,reveal a notable nearest-neighbour bond distortion, and this effect is attributed to variation of bond strain. This strain appears to be carried by distortion of the bond angles, as seen from the comparison of nearest and second nearest neighbour bond strains. The layer grown at 300 °C reveals that the bond strain is under tension. However, the bond strain for the layer grown at 500 °C is largely compressive.

Further observation of the curve plotted for strains as function $\sin^2\psi$ from diffraction peaks and the corresponding tabulated results reveal that the layers are under compressive stress. Typical residual stress obtained for growth temperatures of 300 °C and 500 °C is between 100 to 2200 MPa. Though the origin of this residual stress in the layer has been suggested [53] as a result of the incorporation of hydrogen into the silicon network, the value of the stress, in this work, is to a high degree determined by the structural order of the materials.

University of Cape Town

Furthermore, the stress curves show a strong presence of the stress gradient on the layers particularly in the near surface (or in the interfaces). The existence of this behavior is as a result of the non-vanishing strain components ε_{13} or ε_{23} and the corresponding non-vanishing stress components σ_{13} or σ_{23}. However, with this study alone, it is not possible to explain the nature of this stress gradient. The study of a full profile of the penetration depth in the layer could achieve this in a future. The general conclusion that can be drawn

from the above observations is that the microstructure in the a-Si:H layer is tightly controlled by the deposition process.

University of Cape Town

REFERENCES

[1] K. Tanaka, E. Maruma, T. Shimada, and H. Okamoto, Amorphous Silicon, John Wiley & Son, England (Chichester), 1999

[2] S.R. Elliot, Physics of Amorphous Materials (2nd edition), Longman Group Limited, UK (1990)

[3] K. Morigaki, Physics of amorphous semiconductor, Imperial College Press and World Scientific Publishing Co. Pte. Ltd, UK (1999)

[4] B. Stannowski, J.K Rath, R.E.L. Schropp, Thin Solid Films 430, 220 (2003)

[5] Julio Carabe, Gert Jan Jongerden, a-SiNet: The European Network on Amorphous-Silicon Device Technology

[6] B. D. Cullity: Elements of X-ray diffraction (2nd edition), Addison-Wesley, New York (1978)

[7] R. Prieto-Alcón, E. Márquez, J.M. González-Leal, J. Optoel. Adv. Mat., Vol.2, No.2, 139 (2000)

[8] F. Badawi and P. Villain, J. Appl. Cryst. 36, 869-879 (2003)

[9] Y.C. Tsui, T.W. Clyne, Thin Solid Films 306, 23-33 (1997)

[10] K .S. Stevens and N.M. Johnson, Mater. Res. Soc. Proc. 219, 615 (1991)

[11] J .P. Harbison, A.J. Williams and D.V. Lang, J. Appl. Phys. 55, 946 (1984)

[12] P. Danesh and B. Pantchev, Semicond. Sci. Technol. 15, 971-974 (2000)

[13] Y. Hishikawa, J. Appl. Phys. 62, 3159 (1987)

[14] A. Kelly, Crystallography and Crystal Defects, Wiley & Sons Ltd, New York (2000)

[15] M. Härting, S. Woodford, D. Koensen, R. Bucher and D.T Britton, Thin Solid Films 430, 153 (2003)

[16] H.M. Branz, S.E. Asher, & B.P. Nelson, The American Physical Society, 47(12), 7061-7065 (1993)

[17] H.M. Branz, Reedy, R. Crandall, R.S. Mahan, H. Xu, Y. Nelson, J. Non-Cryst.Solids (ICAMS-19), 27-31 (2001)

[18] H.M. Branz, Phys. Rev. B. 59(8), 5498-5512 (1999)

[19] H.P Klug and L.E. Alexander, X-ray Diffraction Procedure for Polycrystalline and Amorphous Materials (2nd edition), John Wiley & Sons, New York (1974)

University of Cape Town

[20] M. Härting, D.T. Britton, E. Minani, T.P. Ntsoane, M. Topic, T. Thovhogi, O.M. Osiele, D. Knoesen, S. Harindintwari, F. Furlan, C. Giles, Thin Solid Films 501, 75-78 (2006)

[21] David W L Hukins, X-ray Diffraction by Disorder and Ordered System, Pergamon Press LTD, UK (1981)

[22] A. Menelle, A.M. Flank, P. Lagarde, and R. Bellissent, J. Physique C8, 379 (1986)

[23] M. Härting, D.T Britton, R. Bucher, E. Minani, A. Hempel, M. Hempel, T.P. Ntsoene, C. Arense, and Koensen, J. Non-Cryst. Solids. 103, 299-302 (2002)

[24] W.H. Zachariasen, The Atomic Arrangement in Glass. J. Amer. Chem. Soc.54, 3841-3850 (1932)

[25] R.L. Mozzi & B.E. Warren, J. Appl. Cryst. 2, 164-172 (1969)

[26] D.T. Britton, A. Hempel, M. Härting, G. Kogel, P. Sperr, W. Trifthäuser, C. Arense, and D. Knoesen, Phys. Rev. B 64, 075403 (2001)

[27] A.C. Wright, J. Non-Cryst. Solids, 179, 84-115 (1994)

[28] F. Yonezawa, Fundamentals of Amorphous Semiconductors, OMH Publishing Company, Tokyo, 29 (1982)

[29] J.S. Lannin. Phys. Today, 9 July 1980, 28

[30] R. Zallen, Amorphous Solids, John Wiley & Sons, New York (1983)

[31] K. Laaziri, S. Kycia, S. Roorda, M. Chicoine, J. L. Robertson, J. Wang, and S. C. Moss, Phys. Rev. Lett. 82, 3460 (1999)

[32] K. Laaziri, S. Kycia, S. Roorda, M. Chicoine, J. L. Robertson, J. Wang, and S. C. Moss, Phys. Rev. B 60, 13520 (1999)

[33] D.E. Polk, J. Dixmier, Mat. Sci. Eng. 23, 116 (1969)

[34] Richard Levinus Christopher, Computer Simulation of Amorphous Semiconductor, PhD Thesis, Utrecht University (2002)

[35] W. H. Zachariasen, J. Am. Chem. Soc.54, 3841 (1932)

[36] M.H. Brodsky, M.H. Kaplan and J.F. Ziegler, Apply. Phys. Lett.21, 305 (1972)

[37] N.F. Mott, Adv. Phys.16, 49 (1967)

[38] R. A. Street, Phys. Rev B, 43(3), 2454 (1991)

[39] R.A. Street, Phys. Rev. B 43, 2454 (1991), R.A. Street, Phys. Rev. B 44, 10610 (1991)

[40] M. Stutzmann, Philos. Mag. B 60, 531 (1989)

[41] D. Weaire, N. Higgins, P. Moore and I. Marshall, Phil. Mag. B 40, 243 (1979)

University of Cape Town

[42] A. Madan and M.P. Shaw, The Physics and Applications Semiconductors, Academic Press, San Diego (1988)

[43] P.J. Withers and H.K.D.H. Bhadeshia, Residual Stress Part1-Measurement Techniques, Materials Science and Technology Vol. 17, 363 (2001)

[44] F. Badawi and P. Villain, J. Appl. Cryst 36, 869-879 (2003)

[45] L.D. Landau and E.M. Lifshitz, Theory of elasticity Vol 7, Pergamon Press Ltd, UK (1970)

[46] www.dyu.edu.tw/~da/Teaching/MEMS/Handouts/mems-07-stress.pdf, 18-08-2005

[47] J. Matejicek, S. Sampath, Acta Mater. 49, 1993-1999 (2001)

[48] D. L. Windt, W. L. Brown, C. A. Volkert, W. K. Waskiewicz, Variation in Stress with Background Pressure in Sputtered Mo/Si Multilayer Films, AT&T Bell Laboratories

[49] X.L. Peng, Y.C. Tsui, T.W. Clyne, Diamond Relat. Mater.6, 1612-1621 (1997)

[50] F. Kroupa, Acta Technica CSAV, 42, 591 (1997)

[51] J. Matejicek, S. Sampath, Acta Materialia, 51, 863-872 (2003)

[52] T.W. Clyne, S.C. Gill, J. Therm. Spray Technol., 5(4), 1-18 (1996)

[53] B. Panchev, P. Danesh, I. Savatinova, E. Liarokapis, B. Schmidt, D. Grambole, J. Baran, Phys. D: Appl. Phys.34, 2589-2592 (2004)

[54] F. M. D'Heurle, Metal. Transitions, 1, 725-732 (1970)

[55] C.C. Fang, F. Jones, and V. Prasad, J. Appl. Phys 74, 4472-4482 (1993)

[56] S. Hara, S. Izumi, S. Sakai, Statistically Properties of Interface Stress of Amorphous Silicon, www.fml.t.u.tokyo.ac.jp/~izumi/papers/asi-ceb.pdf, 05-10-2005

[57] A.Von Keudell and J. R. Abelson, Phys. Rev B, 59(8), 5791-5798 (1999)

[58] W.B. Jackson, C.C. Tsai, Phys. Rev. B 45, 6564 (1992)

[59] I. Shimuzu, J. Non-Cryst. Solids114, 145 (1989)

[60] Deal Levi, Brent P. Nelson, Robert Reedy, Thin Solids Films 430, 20-23 (2003)

[61] A. Von Keudell and J. R. Abelson, Jpn. J. Appl. Phys. 38, 4002-4006 (1999)

[62] P. Danesh, B. Panchev, K. Antonova, E. Liarokapis, B. Schmidt, D. Grambole, J. Baran, Phys. D: Appl. Phys.37, 249-254 (2004)

[63] N. Martsinovich, M.I. Heggie, C. P. Ewels, J. Phys. Condens. Matter 15, S2815-S2824 (2003)

[64] J.F. Graczy, Phys. Stat. Sol A, 55, 231 (1979)

[65] J.W. Ager III, M.D. Drory, Phys. Rev. B 48, 2601 (1993)

University of Cape Town

[66] Grant S Henderson, The Application of Synchrotron Radiation to the Study of Amorphous materials 30, 159-178 (2002)
[67] Shuji tiara, X-ray Studies on Mechanical Behavior of Materials, The society of materials science, Japan, 1974
[68] E.W. Nuffield, X-ray Diffraction Methods, John Wiley & Sons, New York (1966)
[69] V. Petkov, J. Appl. Cryst. 22, 387-389 (1989)
[70] M. Härting, Acta Mater. 46, 1427-1436 (1998)
[71] U. Welzel, J. Ligot, P. Lamparter, A.C. Vermeulen and E. J. Mittemeijera, J. Appl. Cryst. 38, 1-29 (2005)
[72] I.C. Noyan, J.B. Cohen, Residual Stress Analysis, Springer-Verlag, New York (1987)
[73] E. Hurto´s and J. Rodrı´guez-Viejoa, J. Appl. Phys. 87, No.4, (2000)
[74] T. Lorentzen and T. Leffers: in 'Measurement of Residual and applied Stress using Neutron Diffraction', Vol. 216, NATO ASI Series E (ed. M. T. Hutchings and A. D. Krawitz), 253-261, 1992, Dordrecht, Kluwer
[75] M. Franxois, J. M. Sprauel, C. F. Dehan, M. R. James, F. Convert, J. Lu, J. L. Lebrun, N. Ji, R. W. Hendricks: Handbook of Measurement of Residual Stresses, ed. J. Lu, 71-131, 1996, Lilburn, Ga. Society for Experimental Mechanics.
[76] S. A. Martinez, S. Sathish, M.P. Blodgett and M.J. Shepard, Society for Experimental Mechanics, 141 (2003)
[77] H. Windischmann, Crit. Rev. Solid State Mater. Sci. 17, 547-596 (1992)
[78] Thomas Keller, Nikolaus Margadant , Thilo Pirling , Mar´ıa J. Riegert-Escribano , Werner Wagner , Materials Science and Engineering A 373, 33-44 (2004)
[79] K.F. Badawi, P. Villain, P.H. Goudeau, and P.O. Renault, Appl.Phys. Lett. 80, 25 (2002)
[80] T.P. Ntsoane, Residual stress in Pt Coatings under Thermal Influence, M.Sc Thesis, University of Cape Town
[81] V. Hauk, Structural and Residual Stress Analysis by Nondestructive Methods, Elsevier, Amsterdam, 139-152 (1997)
[82] K.S. Stevens, N.M. Johnson, J. Appl. Phys. 71 (1992)
[83] Z. Várallyay, S. Kugler, J. Non-Cryst. Solids 299, 265-268 (2002)
[84] M Härting and G Fritsch, J. Phys. D Appl. Phys. 26, 1814 (1993)
[85] Paul S. Prevéy, XRD Residual Stress Techniques, Lambda Research

University of Cape Town

[86] H .V. Nguyen, I. An, R.W. Collins, Y. Lu, M. Wakagi and C.R.Wronski, Appl. Phys. Lett. 65, 3335 (1994)

[87] J.J. Boland and G.N. Parsons, Science 256, 1304 (1992)

[88] R. A. Street, Hydrogenated amorphous Silicon, Cambridge University Press, Cambridge (1991)

[89] I.K. Jeong, F. Mohiuddin-Jacob, V. Pepkov and S.J.L. Billinge, arXv: Cond-mat/0008079 v1, 4 August 20004

University of Cape Town

APPENDIX

A). COMPLETE SET OF INFORMATION FOR NEAREST-NEIGHBOUR DISTANCE IN Å, AND BOND ANGLE OBTAINED FROM PDF FIRST AND SECOND PEAKS AT $\phi = 0^0, 60^0, 120^0, 180^0, 240^0 and 300^0$, FOR DEPOSITION TEMPERATURES OF 300 °C AND 500 °C

	Deposition temperature 300 °C			Deposition temperature 500 °C		
ψ - tilt	$r_1(Å)$	$r_2(Å)$	$\alpha(°)$	$r_1(Å)$	$r_2(Å)$	$\alpha(°)$
0 °	2.36 ± 0.01	3.88 ± 0.02	110.30 ± 1.0	2.40 ± 0.03	3.91 ± 0.02	109.35 ± 0.01
20 °	2.13 ± 0.01	3.98 ± 0.02	138.30 ± 0.9	2.32 ± 0.03	3.86 ± 0.02	113.08 ± 0.01
40 °	2.34 ± 0.02	3.88 ± 0.01	112.14 ± 0.8	2.17 ± 0.03	3.96 ± 0.02	131.66 ± 0.01
60 °	2.35 ± 0.01	3.92 ± 0.03	113.07 ± 1.1	2.27 ± 0.03	3.85 ± 0.02	115.79 ± 0.02
80 °	2.30 ± 0.02	3.91 ± 0.02	116.20 ± 1.0	2.31 ± 0.03	3.90 ± 0.02	114.99 ± 0.01
85 °	2.35 ± 0.01	3.92 ± 0.02	113.09 ± 0.9	2.23 ± 0.03	3.85 ± 0.02	119.88 ± 0.02

	Deposition temperature 300 °C			Deposition temperature 500 °C		
ψ - tilt	$r_1(Å)$	$r_2(Å)$	$\alpha(°)$	$r_1(Å)$	$r_2(Å)$	$\alpha(°)$
0 °	2.35 ± 0.03	3.87 ± 0.01	110.7 ± 1.0	2.43 ± 0.1	3.90 ± 0.03	106.6 ± 0.8
20 °	2.29 ± 0.02	3.96 ± 0.08	119.8 ± 0.9	2.44 ± 0.1	3.96 ± 0.02	108.5 ± 0.8
40 °	2.34 ± 0.06	3.84 ± 0.01	110.3 ± 0.8	2.32 ± 0.1	3.98 ± 0.06	118.2 ± 1.0
60 °	2.19 ± 0.03	3.93 ± 0.03	127.5 ± 0.7	2.30 ± 0.1	3.97 ± 0.02	119.1 ± 0.9
80 °	2.36 ± 0.07	3.90 ± 0.02	111.6 ± 1.0	2.34 ± 0.1	3.92 ± 0.02	113.8 ± 0.7
85 °	2.28 ± 0.02	3.88 ± 0.01	116.1 ± 0.8	2.29 ± 0.2	3.86 ± 0.01	115.2 ± 0.5

	Deposition temperature 300 °C			Deposition temperature 500 °C		
ψ - tilt	$r_1(Å)$	$r_2(Å)$	$\alpha(°)$	$r_1(Å)$	$r_2(Å)$	$\alpha(°)$
0 °	2.35 ± 0.03	3.87 ± 0.01	110.5 ± 1.0	2.43 ± 0.1	3.90 ± 0.03	106.6 ± 0.8
20 °	2.29 ± 0.02	3.96 ± 0.08	119.8 ± 0.9	2.44 ± 0.1	3.96 ± 0.02	108.5 ± 0.8
40 °	2.34 ± 0.06	3.84 ± 0.01	110.3 ± 0.8	2.32 ± 0.1	3.98 ± 0.06	118.2 ± 1.0
60 °	2.19 ± 0.03	3.93 ± 0.03	127.5 ± 0.7	2.30 ± 0.1	3.97 ± 0.02	119.1 ± 0.9
80 °	2.36 ± 0.07	3.90 ± 0.02	111.6 ± 1.0	2.34 ± 0.1	3.92 ± 0.02	113.8 ± 0.7
85 °	2.28 ± 0.02	3.88 ± 0.01	116.1 ± 0.8	2.29 ± 0.2	3.86 ± 0.01	115.2 ± 0.5

	Deposition temperature 300 °C			Deposition temperature 500 °C		
ψ - tilt	$r_1(Å)$	$r_2(Å)$	$\alpha(°)$	$r_1(Å)$	$r_2(Å)$	$\alpha(°)$
0 °	2.23 ± 0.02	3.83 ± 0.03	118.25 ± 1.0	2.46 ± 0.03	3.95 ± 0.02	106.68 ± 0.01
20 °	2.30 ± 0.02	4.00 ± 0.03	120.95 ± 0.9	2.33 ± 0.03	3.97 ± 0.02	117.43 ± 0.01
40 °	2.31 ± 0.02	3.89 ± 0.03	114.97 ± 0.8	2.30 ± 0.03	3.85 ± 0.02	114.03 ± 0.01
60 °	2.27 ± 0.02	3.98 ± 0.03	122.73 ± 0.7	2.29 ± 0.03	3.91 ± 0.02	117.39 ± 0.02
80 °	2.37 ± 0.02	3.84 ± 0.03	108.12 ± 1.0	2.35 ± 0.03	3.87 ± 0.02	111.11 ± 0.01
85 °	2.31 ± 0.02	3.89 ± 0.03	114.78 ± 0.8	2.31 ± 0.03	3.89 ± 0.02	114.78 ± 0.02

	Deposition temperature 300 °C			Deposition temperature 500 °C		
ψ - tilt	$r_1(\AA)$	$r_2(\AA)$	$\alpha(°)$	$r_1(\AA)$	$r_2(\AA)$	$\alpha(°)$
0 °	2.35 ± 0.02	3.91 ± 0.02	112.79 ± 1.0	2.44 ± 0.03	3.98 ± 0.02	106.6 ± 0.8
20 °	2.25 ± 0.02	3.93 ± 0.02	121.94 ± 0.9	2.39 ± 0.03	3.90 ± 0.02	108.5 ± 0.8
40 °	2.24 ± 0.02	3.87 ± 0.02	119.32 ± 0.8	2.26 ± 0.03	3.93 ± 0.02	118.2 ± 1.0
60 °	2.29 ± 0.02	3.99 ± 0.02	121.86 ± 0.7	2.31 ± 0.03	3.95 ± 0.02	119.1 ± 0.9
80 °	2.31 ± 0.02	3.89 ± 0.02	114.40 ± 1.0	2.30 ± 0.03	3.89 ± 0.02	113.8 ± 0.7
85 °	2.30 ± 0.02	3.87 ± 0.02	114.60 ± 0.8	2.26 ± 0.03	3.86 ± 0.02	115.2 ± 0.5

B). PEAK PARAMETERS AND STRAIN DETERMINED FROM *2θ* DIFFRACTION PATTERN AND PLOTTED AS A FUNCTION OF $Sin^2\Psi$

Strain for a-Si:H deposited at 300 °C determined from diffraction patterns					
First diffraction peak *(111)*			Second diffraction peak *(220)*		
2θ [°]	*FWHM*	Integral intensity	2θ [°]	FWHM	Integral intensity
20.442	6.6393	3655.8	36.789	6.6965	1515.3
20.041	3.8698	2006.5	36.876	3.8804	938.95
20.173	2.7648	1169.5	36.844	6.4735	1535.7
19.607	3.87	1465.2	37.151	4.4215	918.64
20.549	3.2533	756.12	37.342	4.9472	604.93
20.269	3.4633	496.97	37.078	5.1882	504.56

University of Cape Town

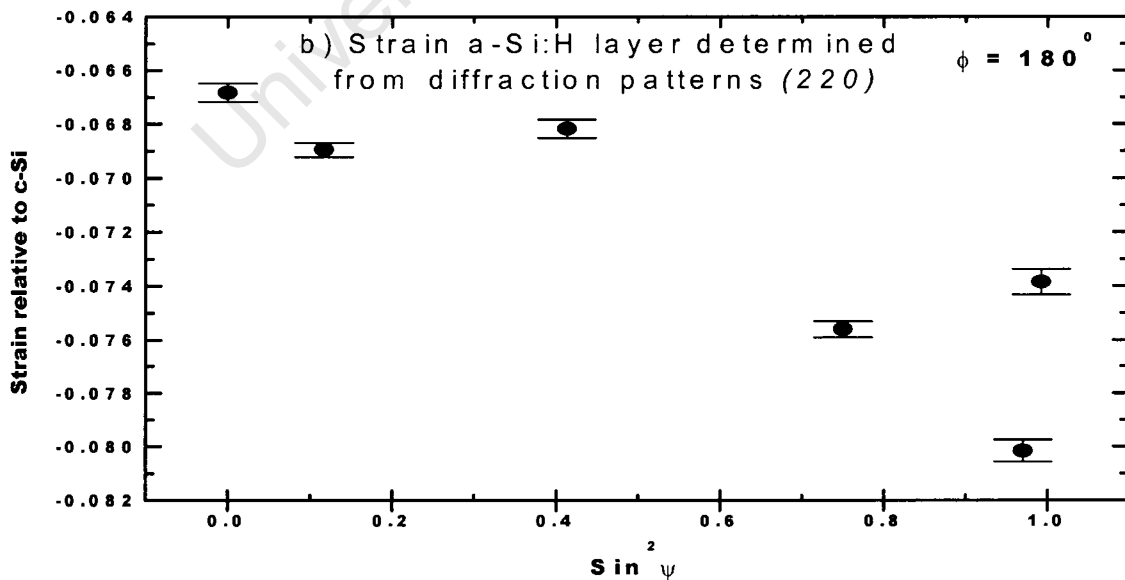

Strain for a-Si:H deposited at 300 °C determined from diffraction patterns					
First diffraction peak *(111)*			Second diffraction peak *(220)*		
2θ [°]	*FWHM*	Integral intensity	2θ [°]	FWHM	Integral intensity
20.457	3.7941	1418.5	36.49	5.7639	832.96
19.69	2.9104	1349.1	36.47	8.5434	2224
20.238	2.8386	1234.5	36.921	5.5501	1051.5
20.067	3.5112	1625.7	37.128	5.2077	1072
20.531	3.4948	832.93	37.184	5.1427	715.81
20.203	3.1297	490.13	37.269	4.8737	453.6

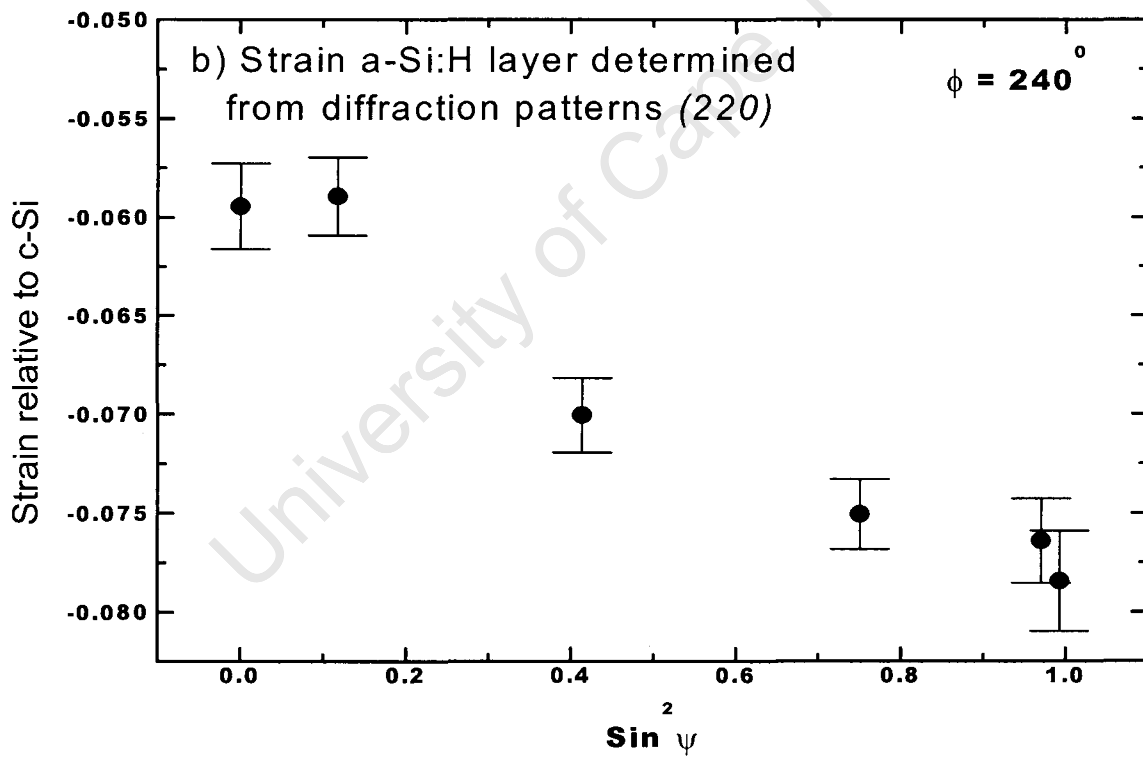

University of Cape Town

Strain for a-Si:H deposited at 300 °C determined from diffraction patterns					
First diffraction peak *(111)*			Second diffraction peak *(220)*		
2θ [°]	*FWHM*	Integral intensity	2θ [°]	FWHM	Integral intensity
20.457	3.7941	1418.5	36.516	10.084	2955.8
19.69	2.9104	1349.1	36.839	4.5309	716.11
20.238	2.8386	1234.5	37.214	5.4672	1363.3
20.067	3.5112	1625.7	37.025	3.987	751.55
20.531	3.4948	832.93	37.277	5.559	671.25
20.203	3.1297	490.13	37.226	5.3871	488.97

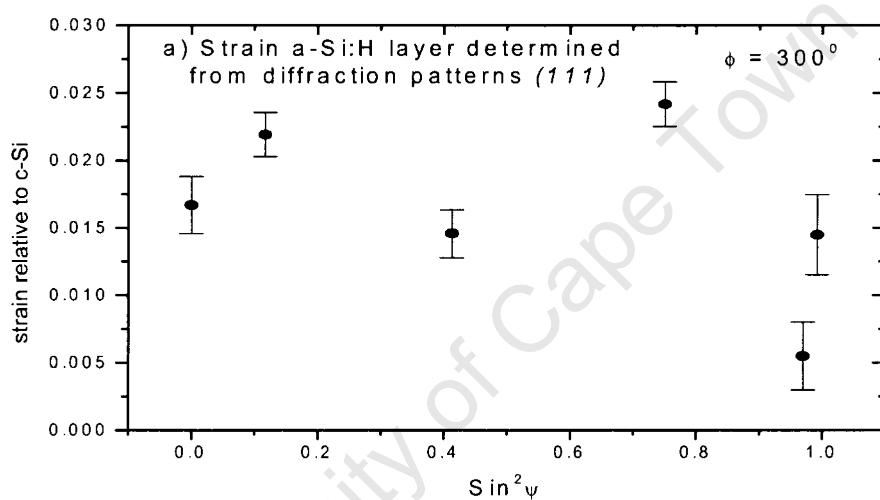

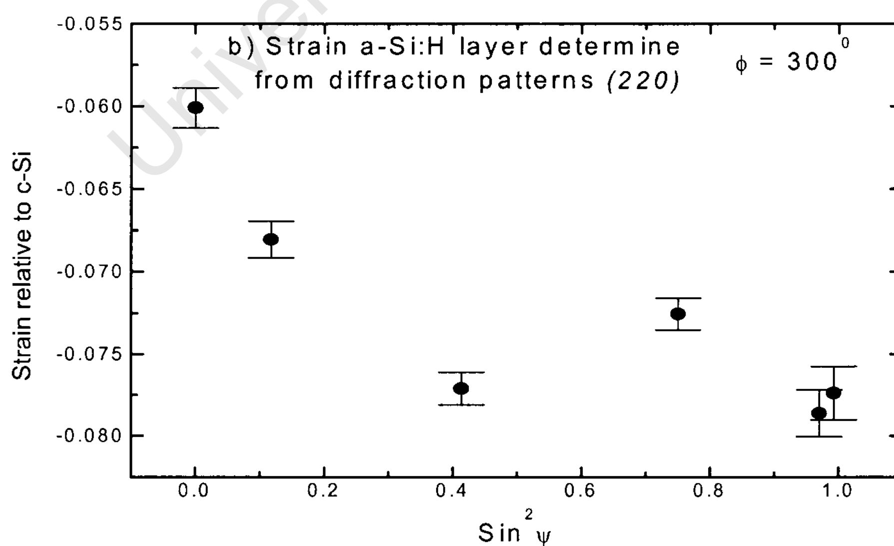

University of Cape Town

Strain for a-Si:H deposited at 500 °C determined from diffraction patterns					
First diffraction peak *(111)*			Second diffraction peak *(220)*		
2θ [°]	*FWHM*	Integral intensity	2θ [°]	FWHM	Integral intensity
20.21	4.0202	1611.4	36.835	4.7188	879.67
20.116	3.4639	1637.9	36.549	10.57	2706.8
20.129	2.640	1235.1	36.941	7.8079	2191.8
20.274	1.9311	626.76	36.996	7.071	1686.1
20.711	3.1323	515.32	36.85	8.0865	1109.7
20.321	2.6433	504.89	37.268	6.5883	459.57

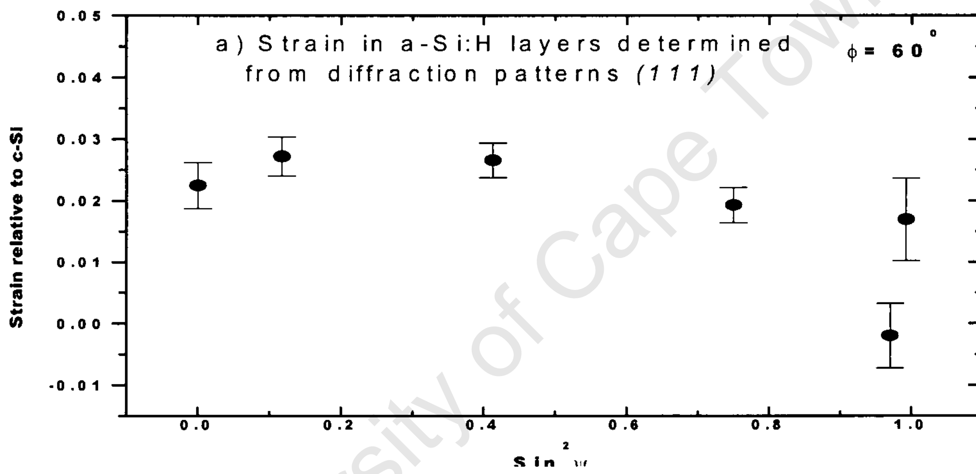

University of Cape Town

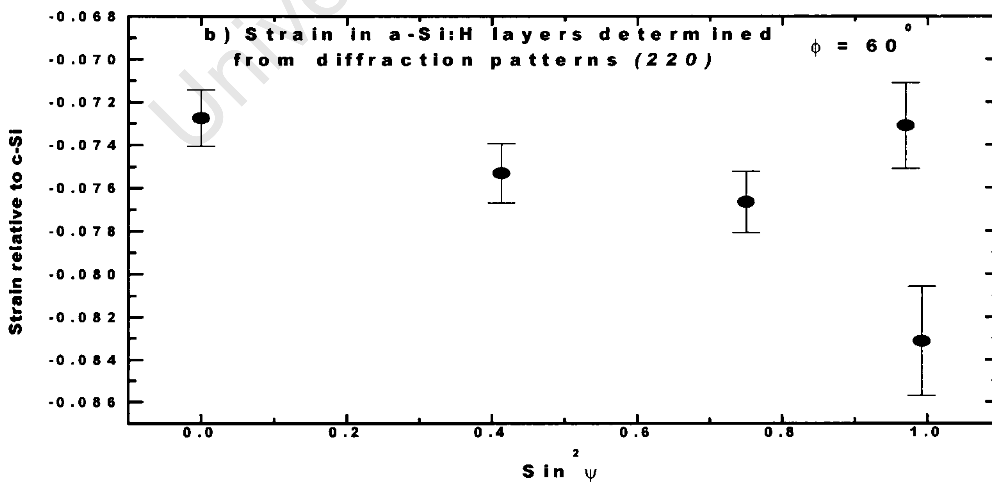

Strain for a-Si:H deposited at 500 °C determined from diffraction patterns					
First diffraction peak *(111)*			Second diffraction peak *(220)*		
2θ [°]	*FWHM*	Integral intensity	2θ [°]	FWHM	Integral intensity
20.131	3.6439	1707.9	36.351	4.8593	929.1
20.07	3.0813	1766.4	37.034	5.8101	1316.4
20.31	3.3627	1528	37.416	3.8653	932.41
20.253	2.9704	999.47	36.712	6.848	1312.9
20.659	3.3103	536.5	37.206	6.5845	802.51
20.481	3.5877	351.03	36.921	6.0565	407.86

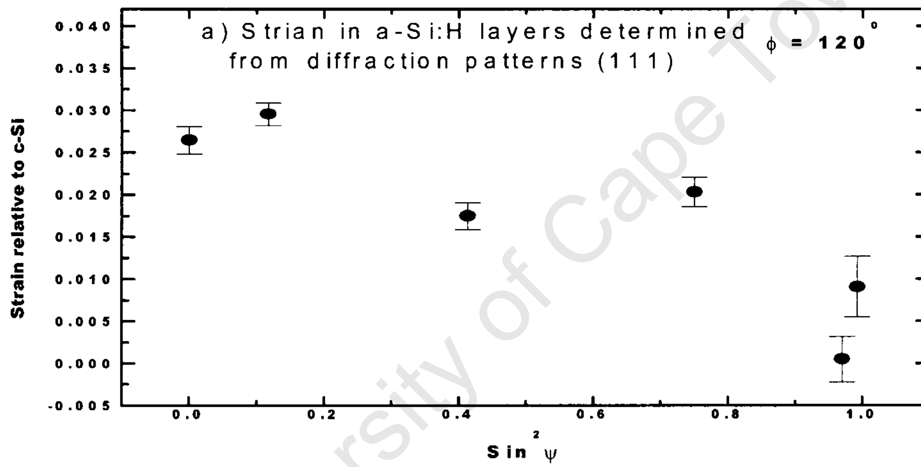

University of Cape Town

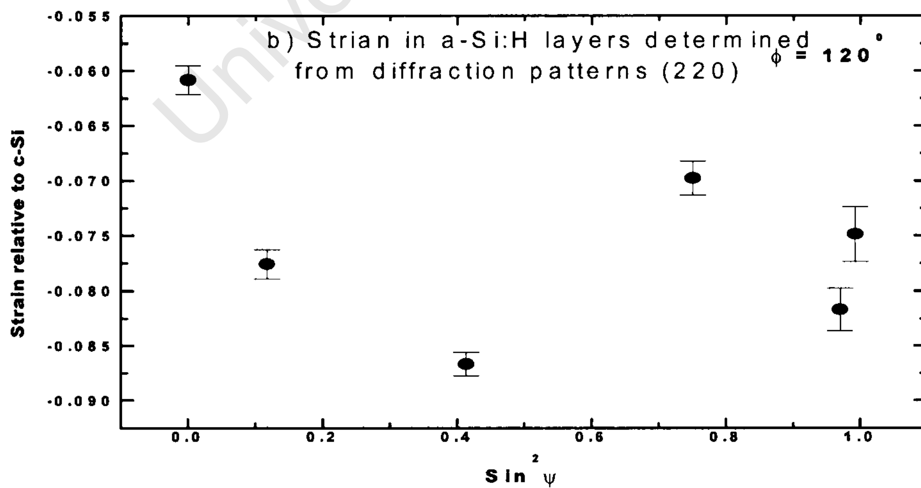

Strain for a-Si:H deposited at 500 °C determined from diffraction patterns					
First diffraction peak *(111)*			Second diffraction peak *(220)*		
2θ [°]	*FWHM*	Integral intensity	2θ [°]	FWHM	Integral intensity
20.15	4.4559	2796.5	36.573	7.15	1432.2
19.85	4.0257	2716.4	36.227	11.019	4537.8
20.26	4.1765	3035.3	36.427	6.6989	1688.3
20.201	3.4754	1447.2	36.918	6.3764	1602
20.672	3.4093	708.64	36.75	6.408	748.08
20.218	3.7641	474.19	37.00	7.0069	671.49

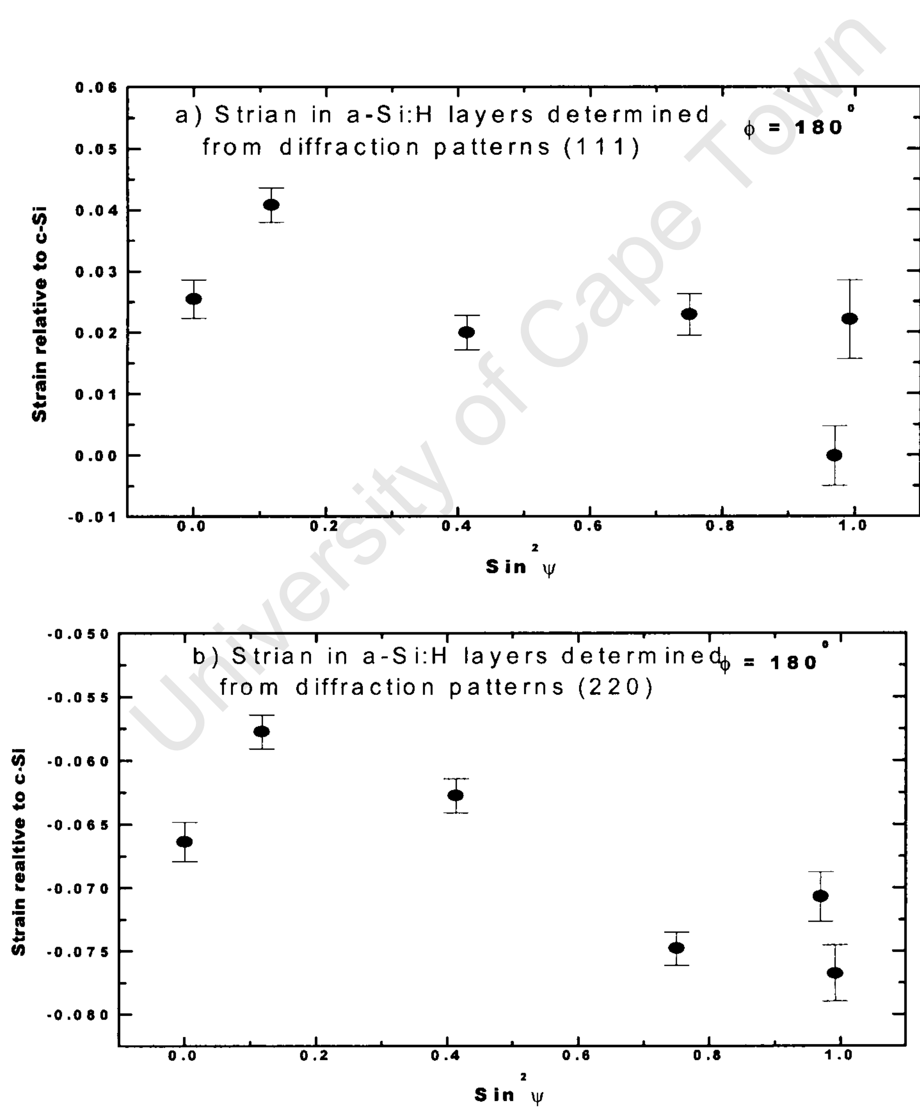

University of Cape Town

Strain for a-Si:H deposited at 500 °C determined from diffraction patterns					
First diffraction peak *(111)*			Second diffraction peak *(220)*		
2θ[°]	*FWHM*	Integral intensity	2θ [°]	FWHM	Integral intensity
20.114	3.8236	2413.8	36.428	5.1894	901.29
19.878	3.3743	2593.1	37.368	3.5772	790.46
20.045	3.711	2383.7	36.751	5.9196	1558.9
20.362	2.822	1072.7	36.929	6.9601	1840.3
20.674	3.0135	562.52	36.923	6.4221	898.75
20.350	3.3217	440.68	36.813	4.9602	365.88

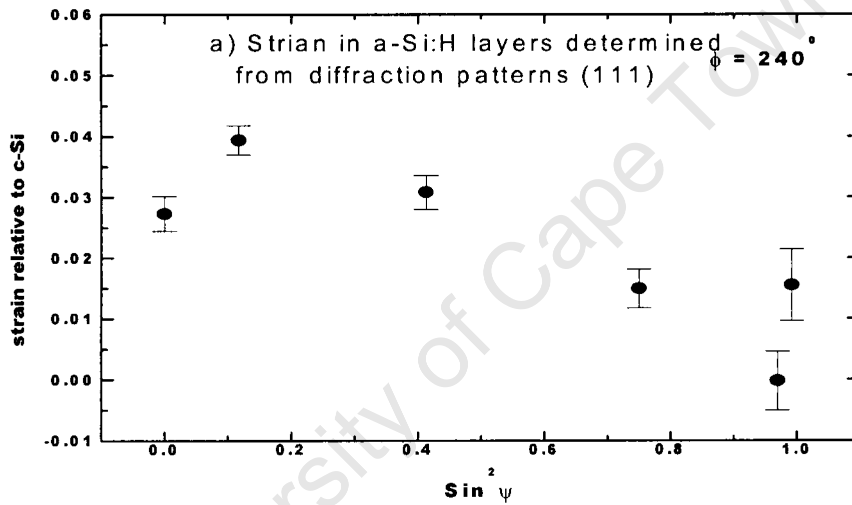

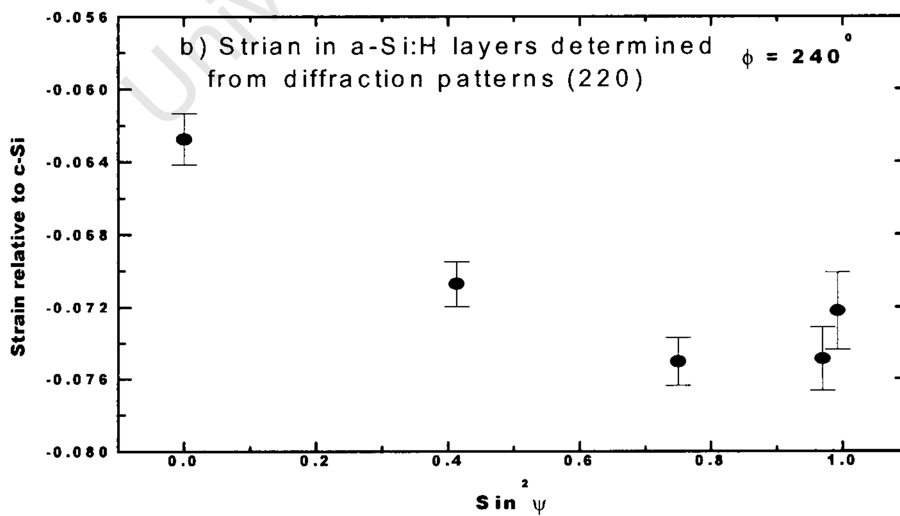

University of Cape Town

University of Cape Town

Strain for a-Si:H deposited at 500 °C determined from diffraction patterns					
First diffraction peak *(111)*			Second diffraction peak *(220)*		
2θ [°]	*FWHM*	Integral intensity	2θ [°]	FWHM	Integral intensity
20.114	3.8236	2413.8	36.428	5.1894	901.29
19.878	3.3743	2593.1	37.368	3.5772	790.46
20.045	3.711	2383.7	36.751	5.9196	1558.9
20.362	2.822	1072.7	36.929	6.9601	1840.3
20.674	3.0135	562.52	36.923	6.4221	898.75
20.350	3.3217	440.68	36.813	4.9602	365.88

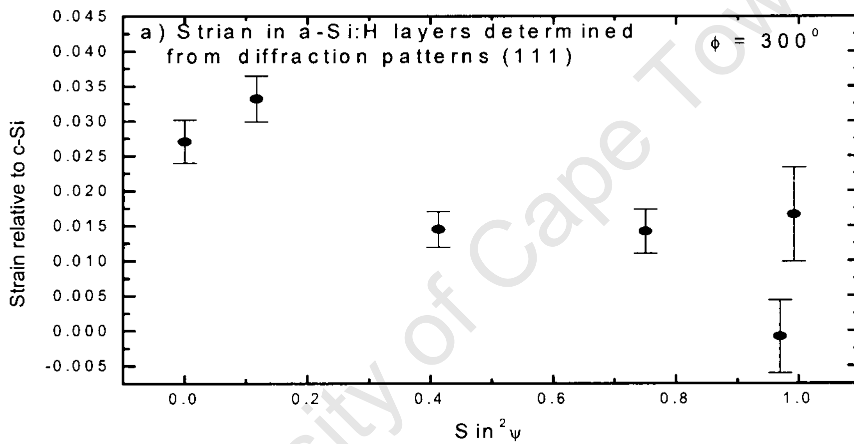

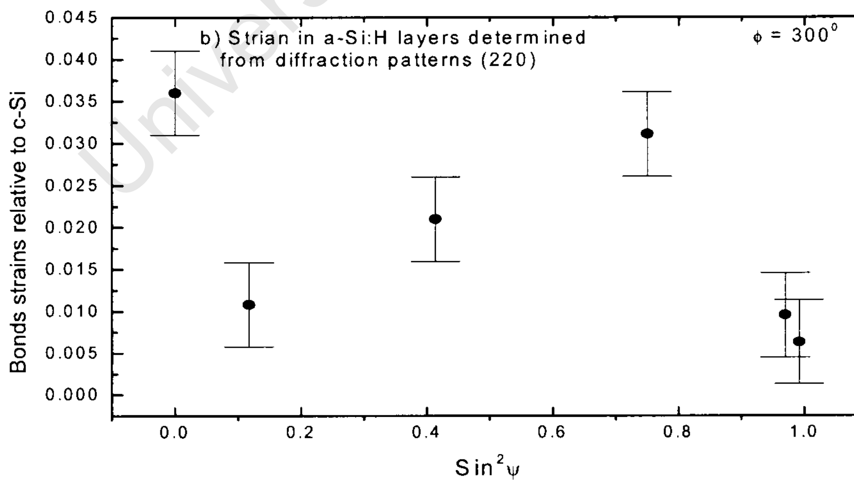

University of Cape Town

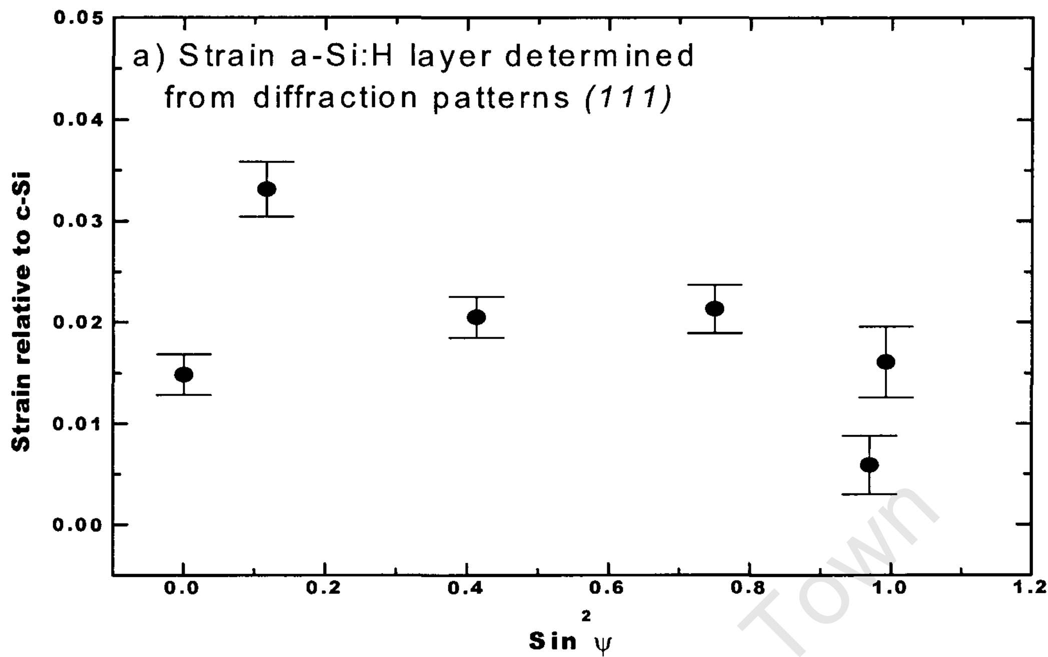

Fig.6.6. Variation of the linear $Sin^2\psi$ obtain in a-Si:H layer at 300°C determined from diffraction pattern (a) first diffraction peak corresponding to the height of the *Si-Si$_4$* tetrahedron, is equivalent to the *(111)* reflection in c-Si

University of Cape Town

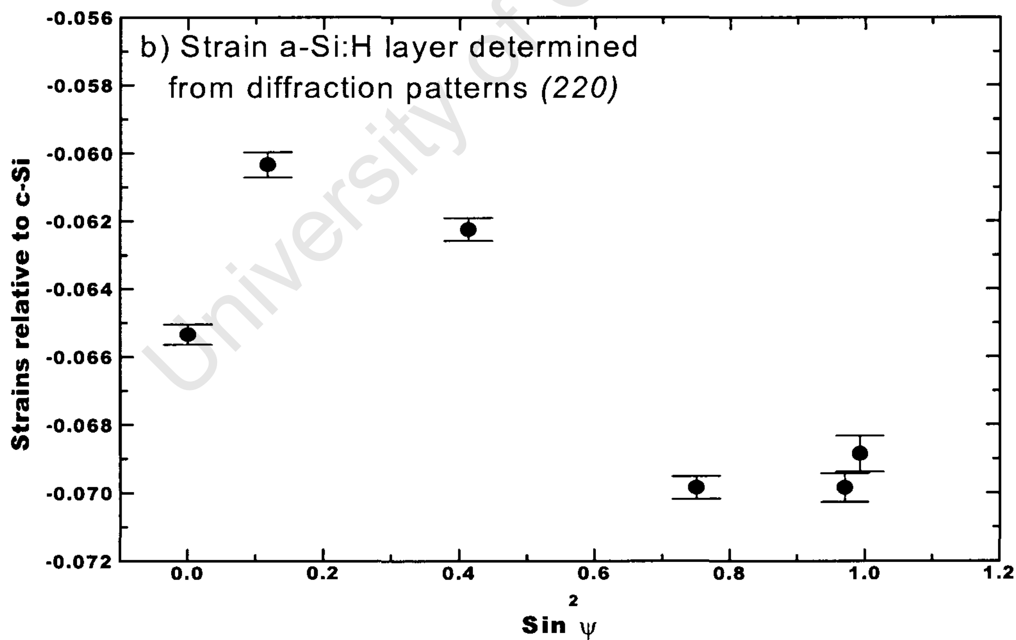

Fig.6.6(b). Variation of the linear $Sin^2\psi$ obtain in a-Si:H layer at 300°C determined from diffraction pattern (b) the second diffraction peak, is equivalent to the *(220)* reflection in c-Si, and corresponding to the length of side of the *Si-Si$_4$* tetrahedron

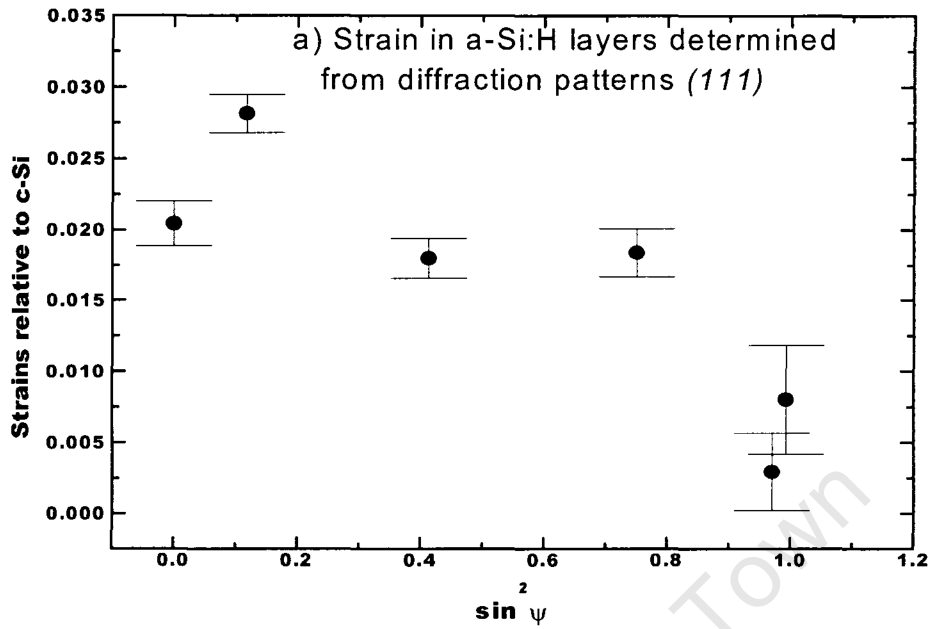

Fig.6.7(a). Variation of the linear $Sin^2\psi$ obtain in a-Si:H layer at 500°C determined from diffraction pattern (a) first diffraction peak corresponding to the height of the *Si-Si*$_4$ tetrahedron, is equivalent to the *(111)* reflection in c-Si

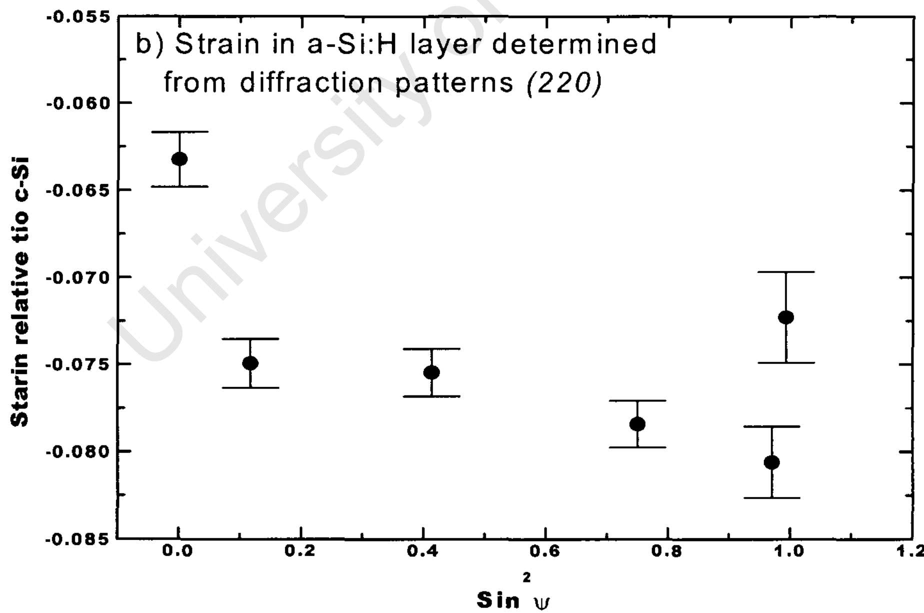

Fig.6.7 (b). Variation of the linear $Sin^2\psi$ obtain in a-Si:H layer at 500°C determined from diffraction pattern (b) the second diffraction peak, is equivalent to the *(220)* reflection in c-Si, and corresponding to the length of side of the *Si-Si*$_4$ tetrahedron

University of Cape Town

C). PAIR DISTRIBUTION FUNCTION AND CORRESPONDING BONDS STRAIN AS FUNCTION OF $Sin^2\Psi$ DETERMINED FROM PDF FOR SAMPLE S DEPOSITED AT 300 °C AND 500 °C

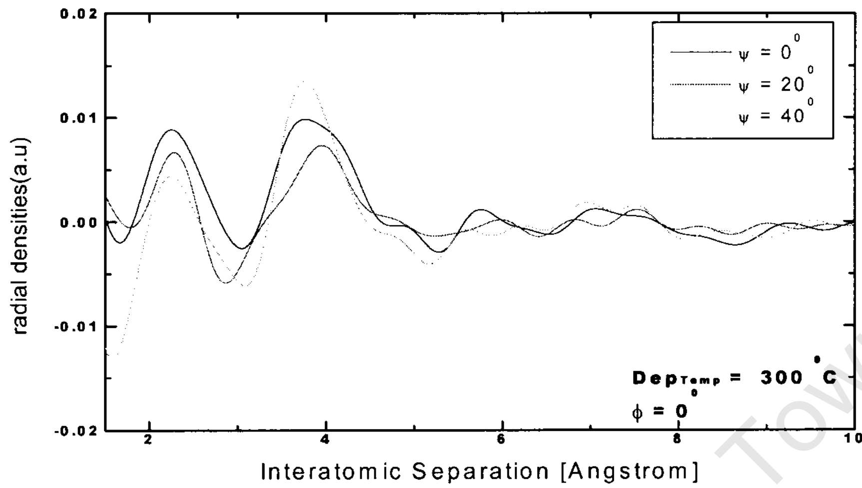

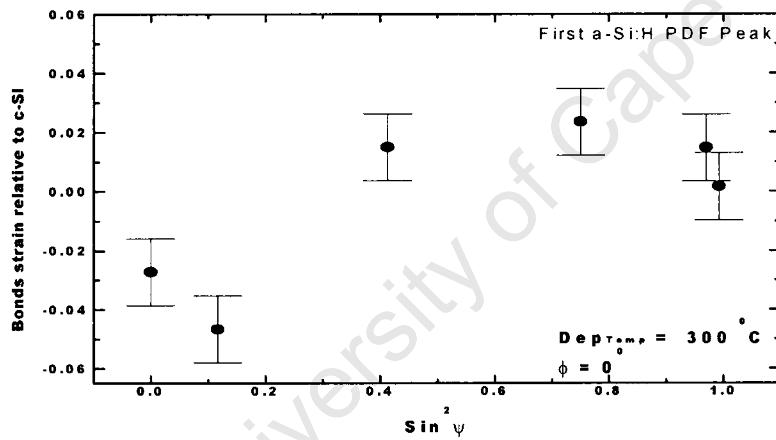

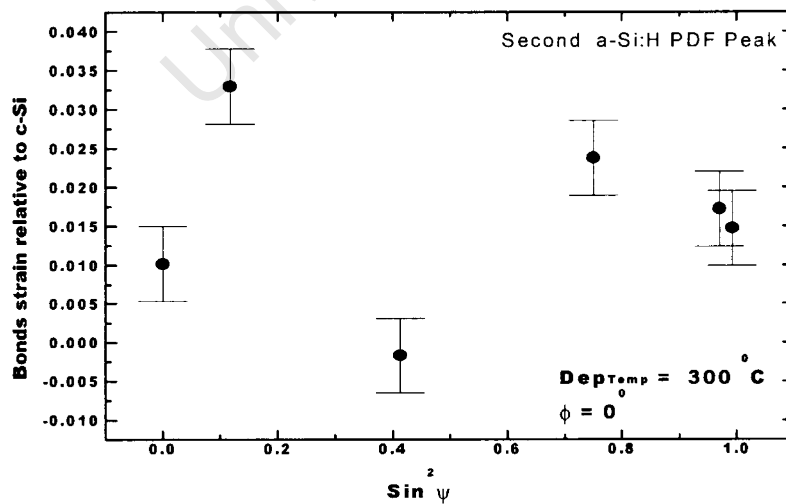

University of Cape Town

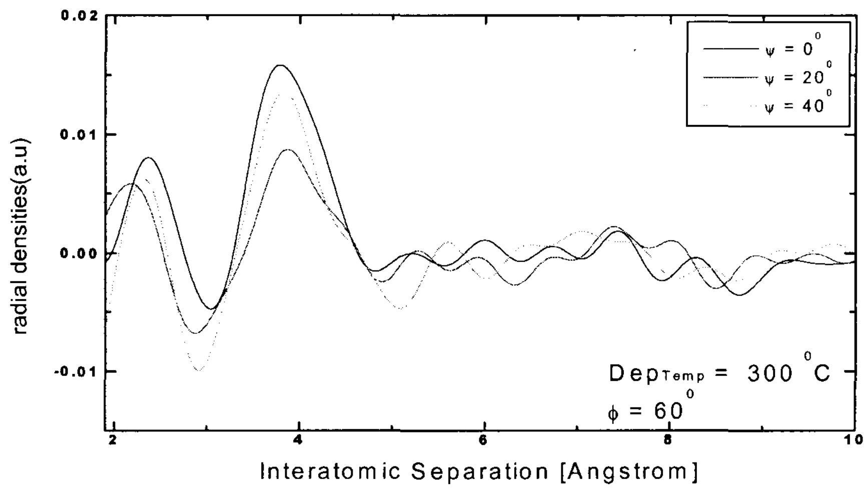

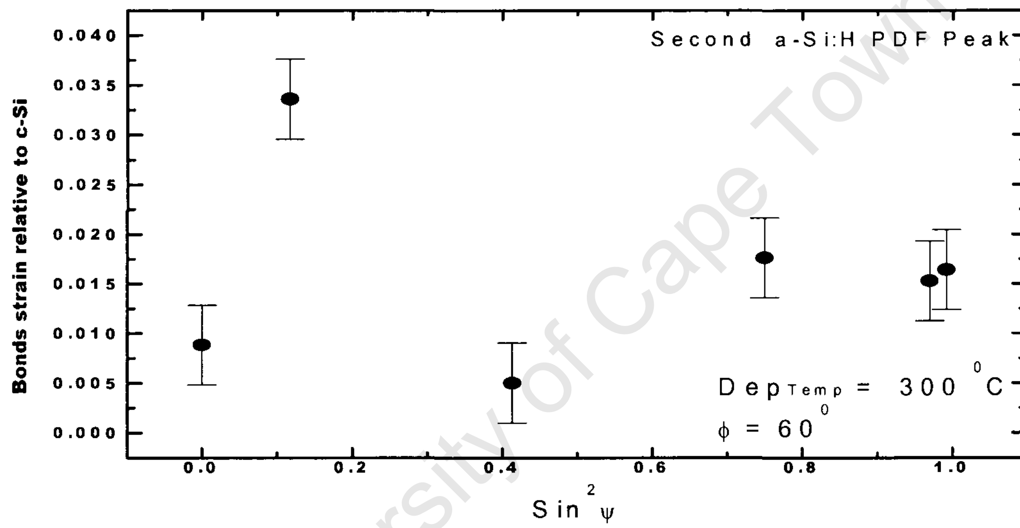

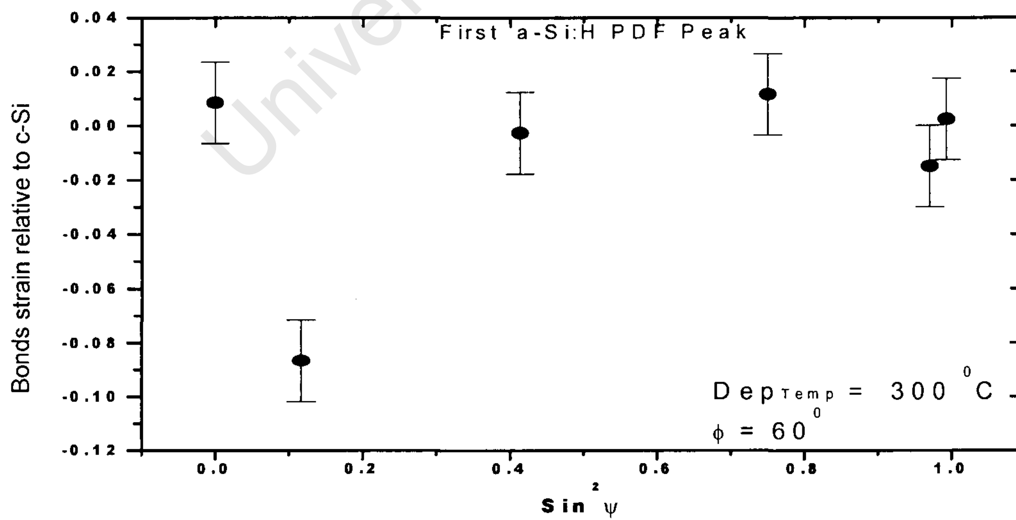

University of Cape Town

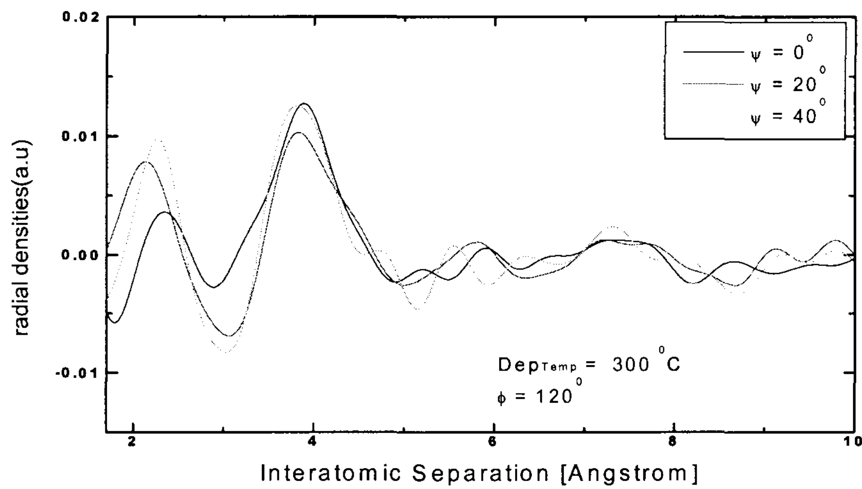

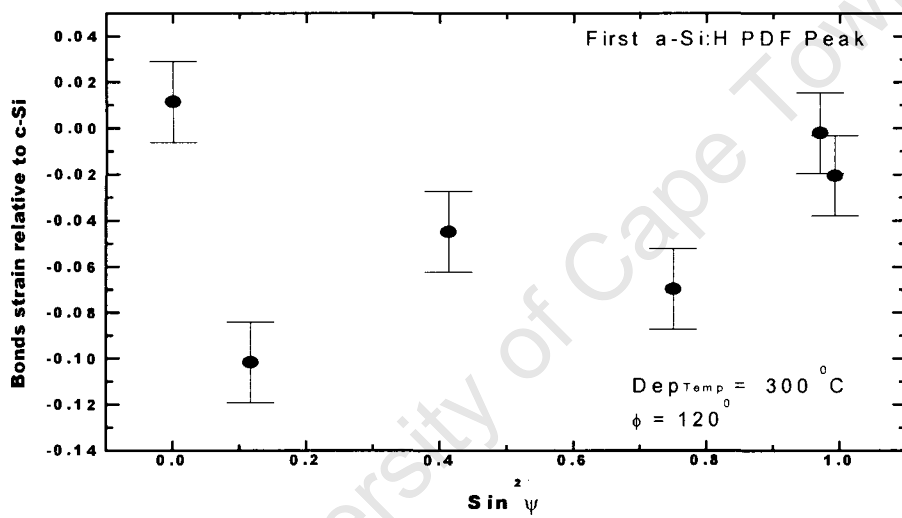

University of Cape Town

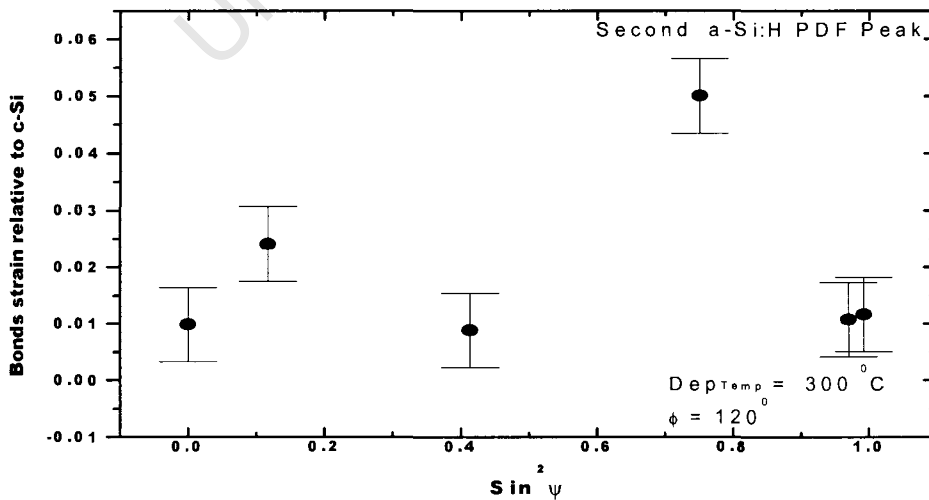

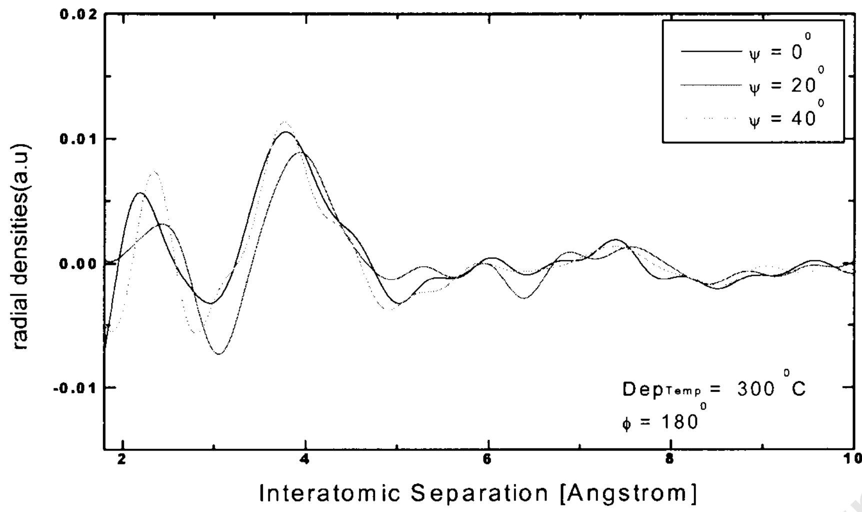

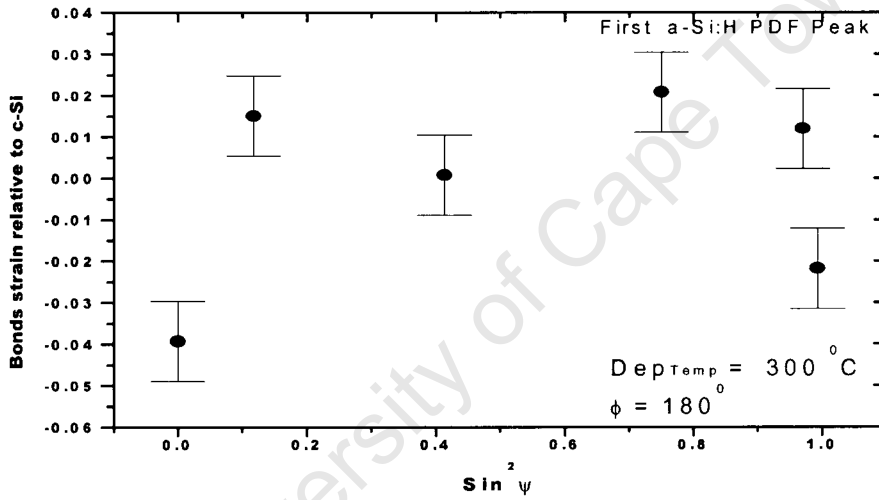

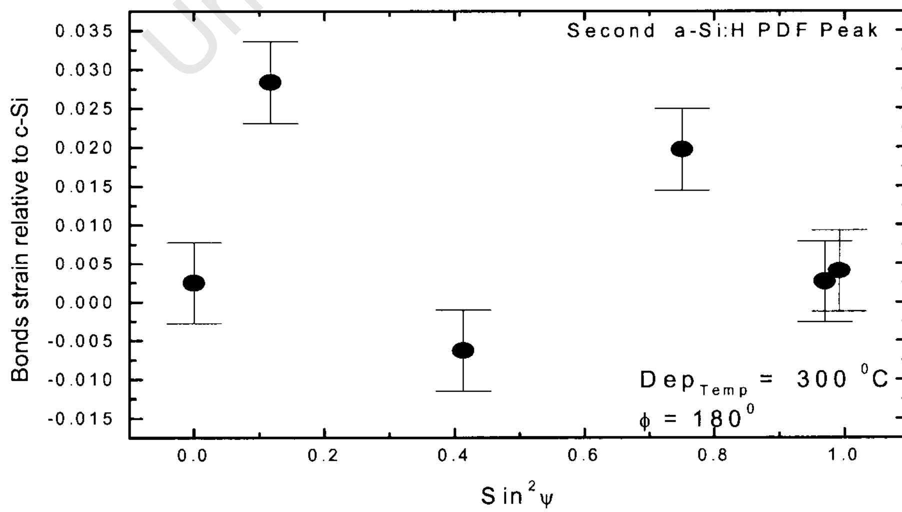

University of Cape Town

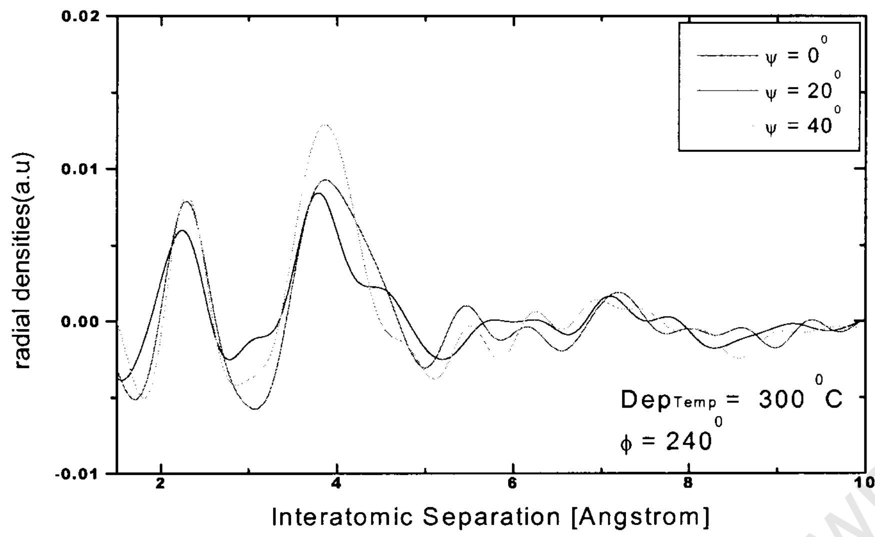

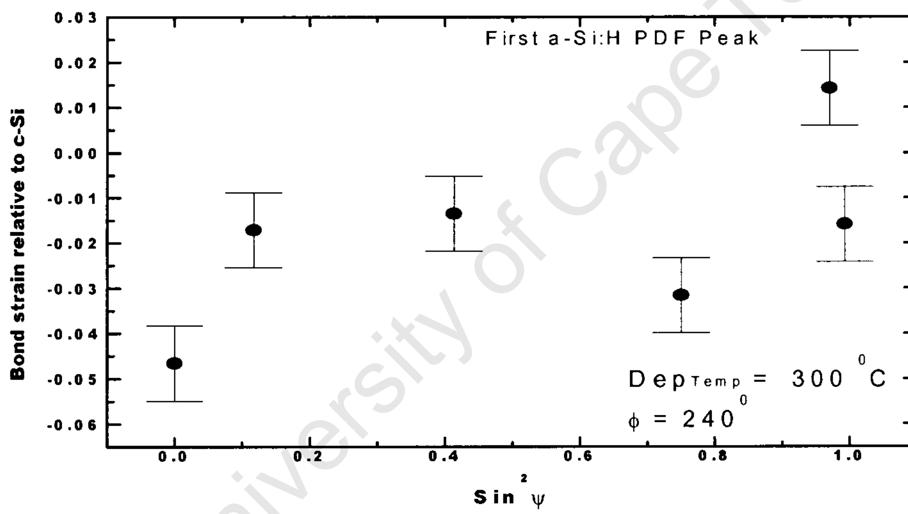

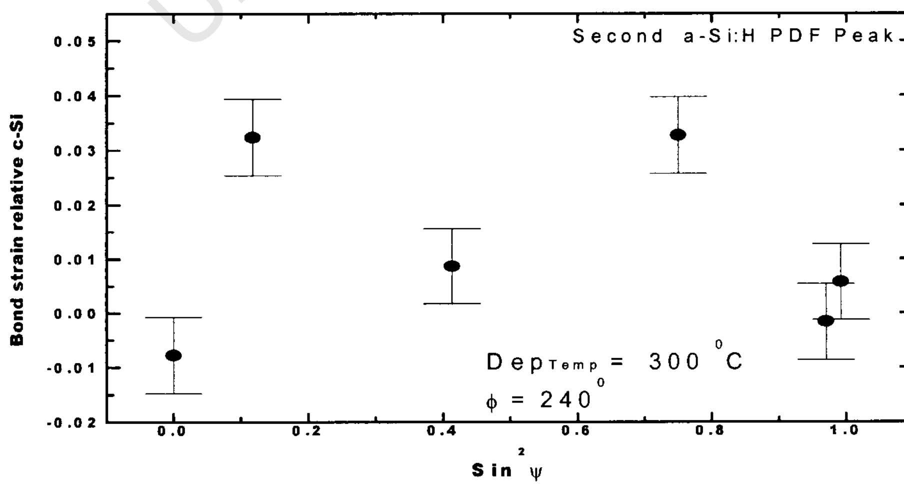

University of Cape Town

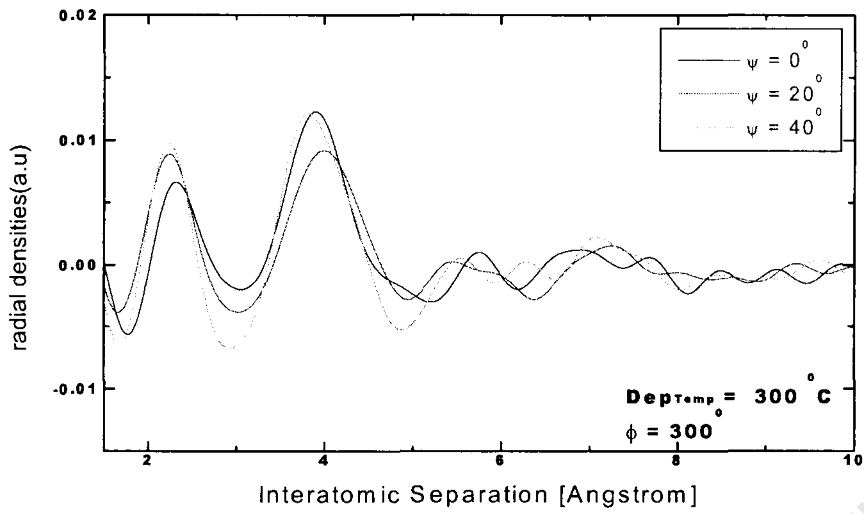

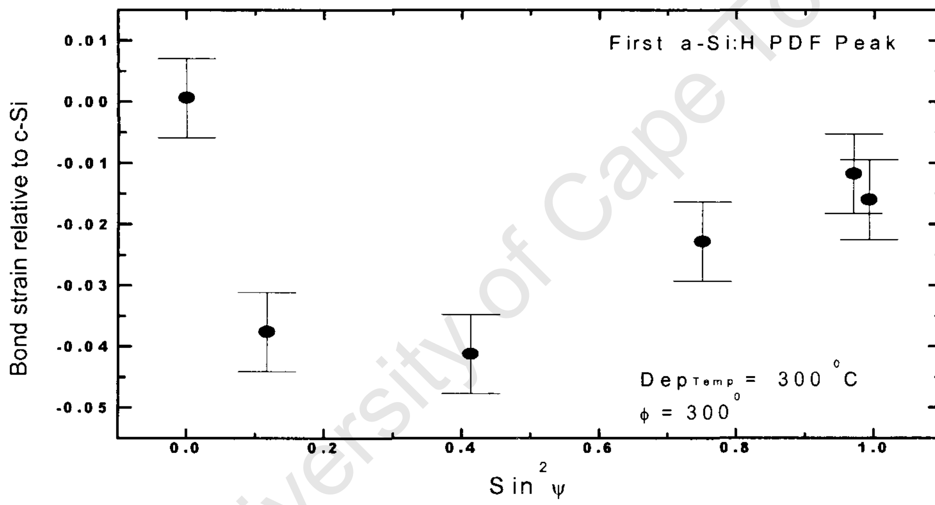

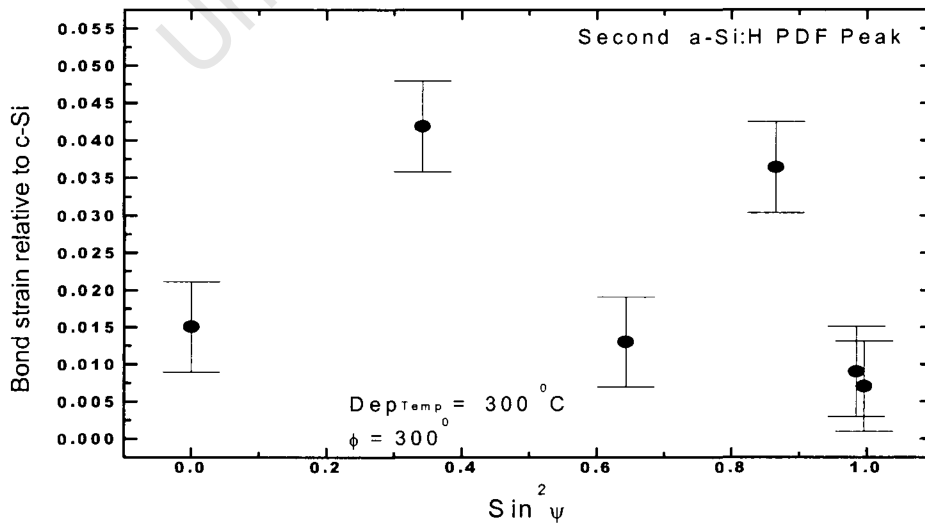

University of Cape Town

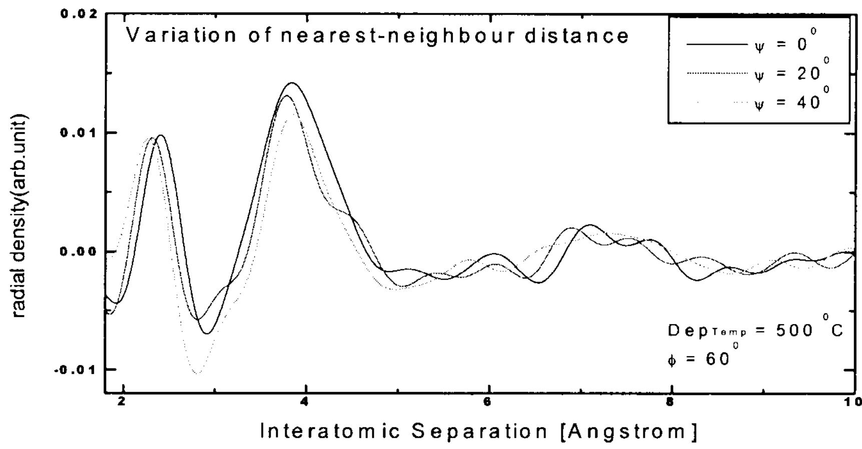

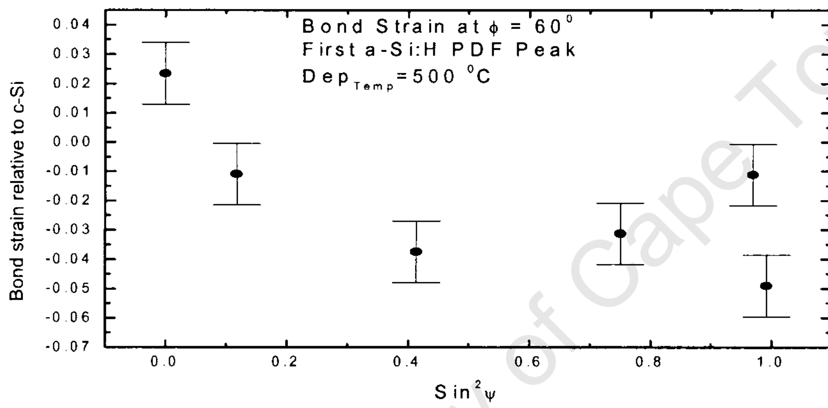

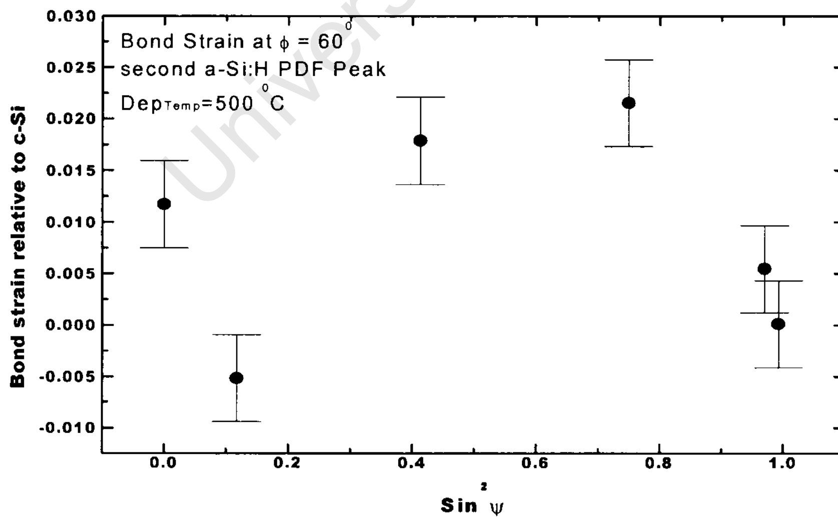

University of Cape Town

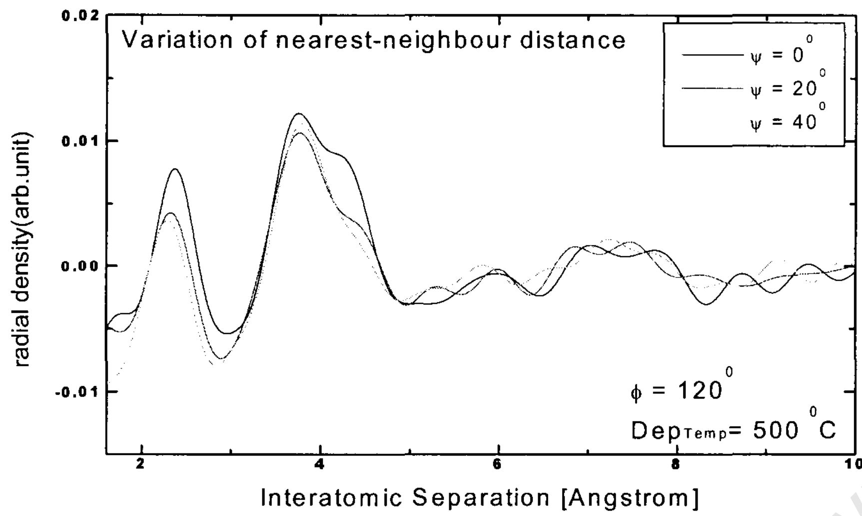

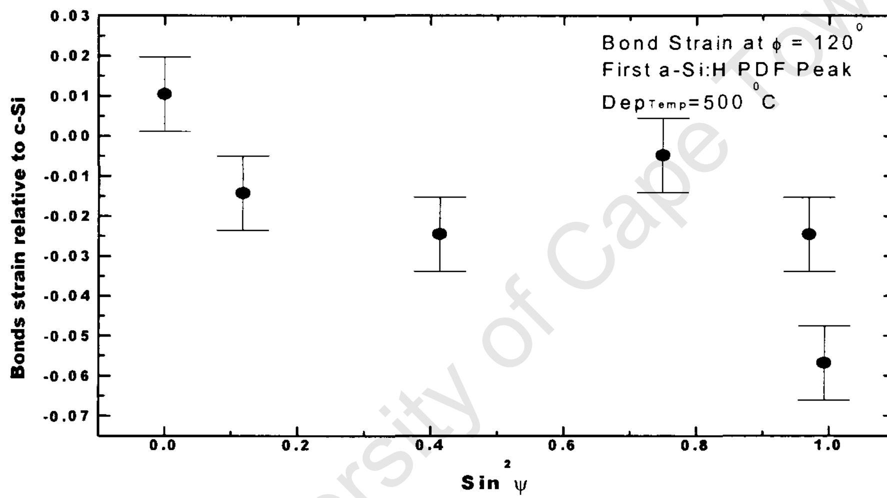

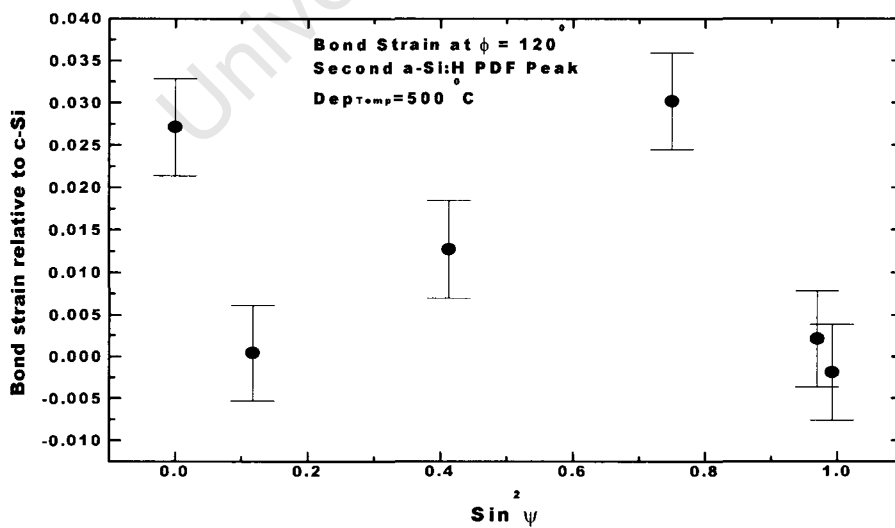

University of Cape Town

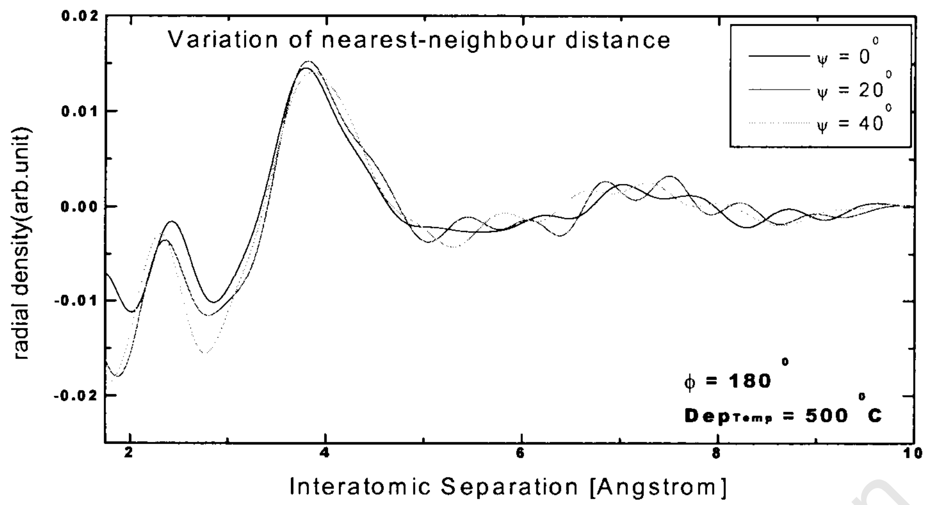

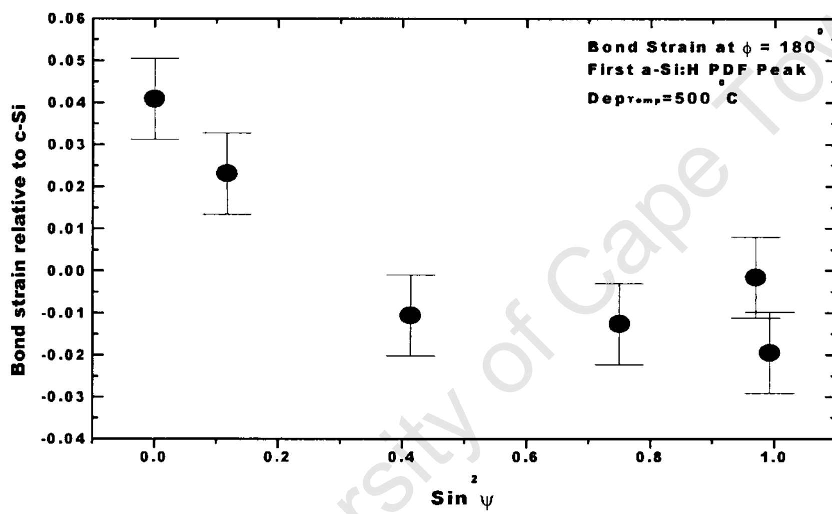

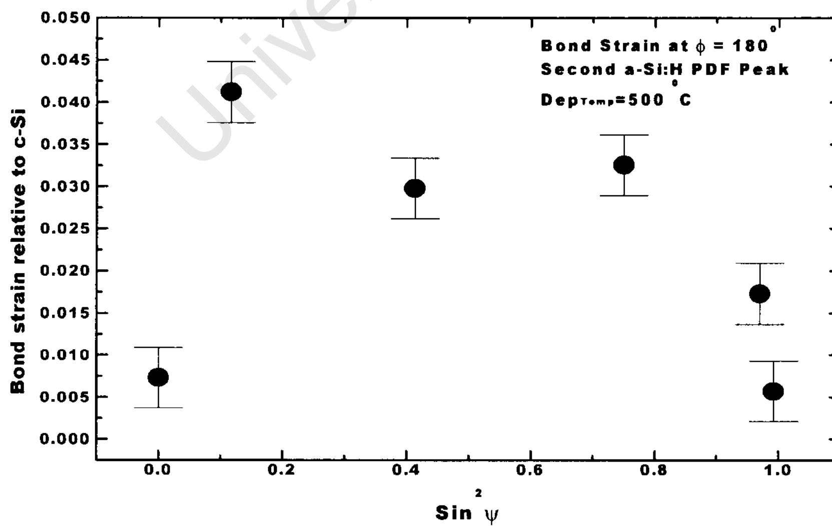

University of Cape Town

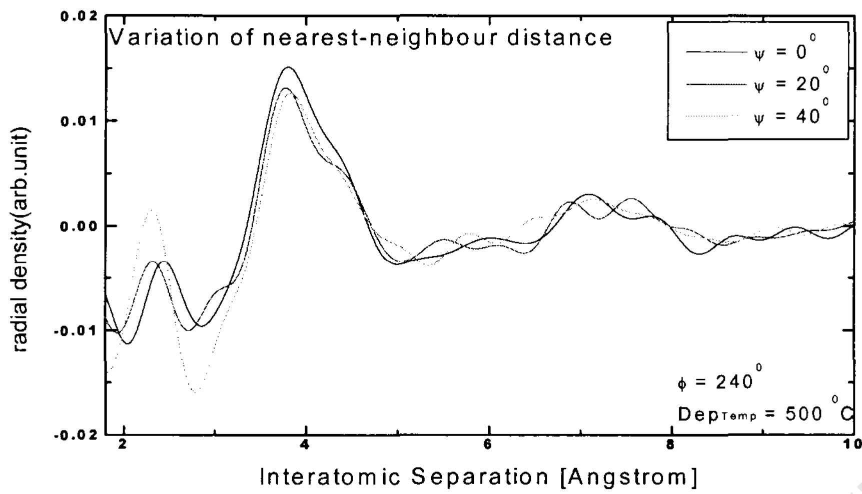

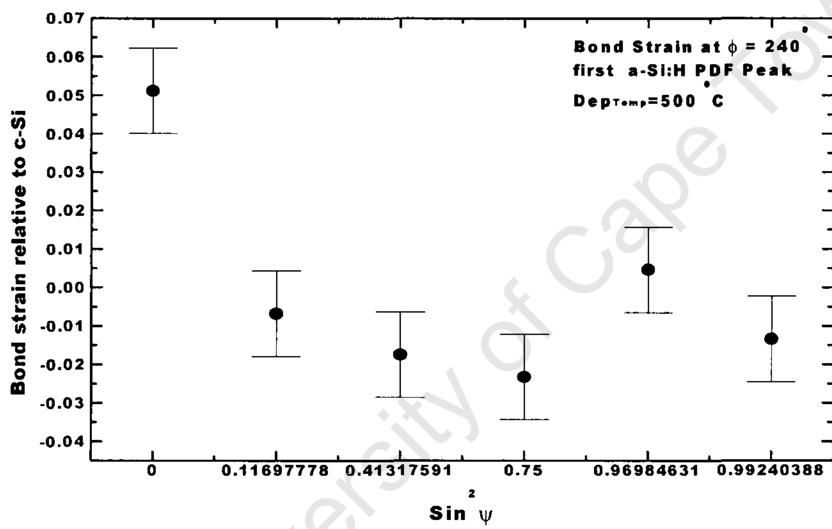

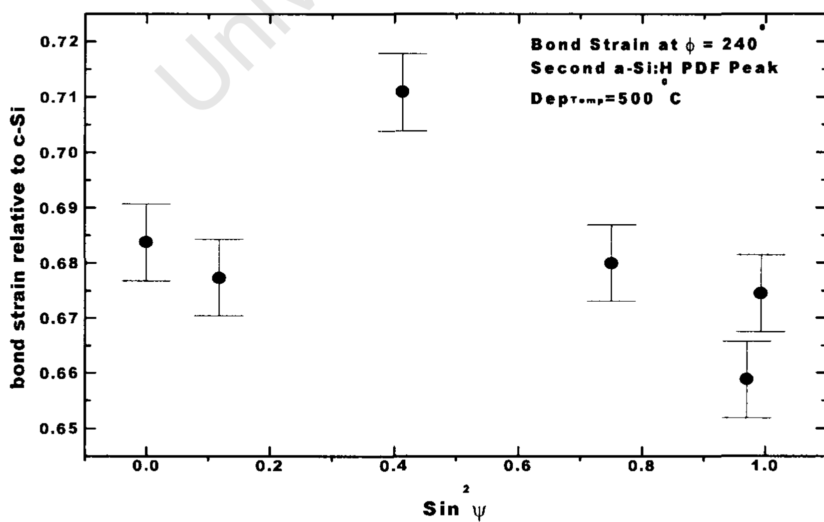

University of Cape Town

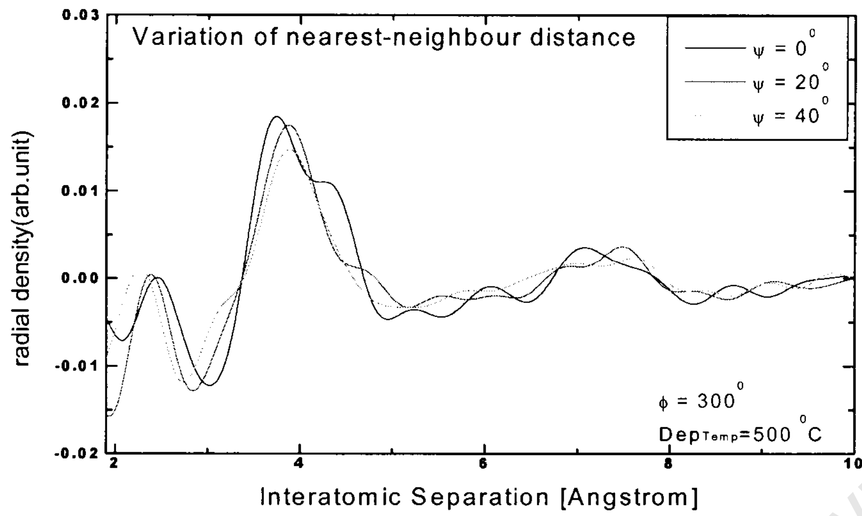

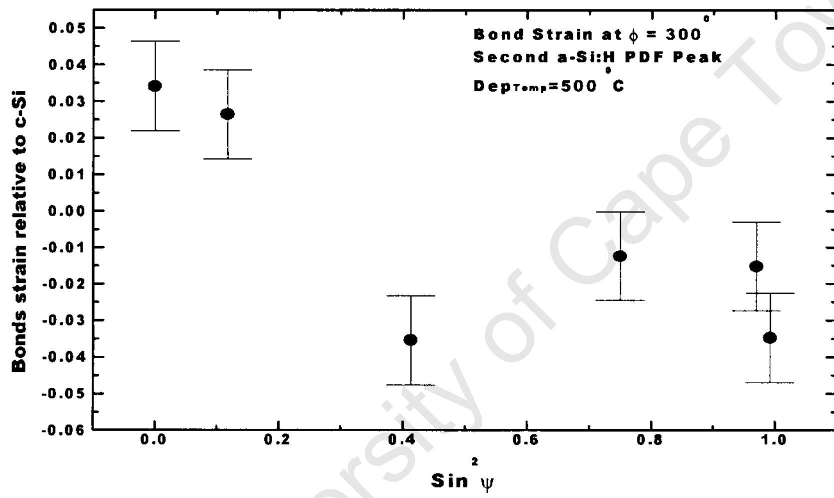

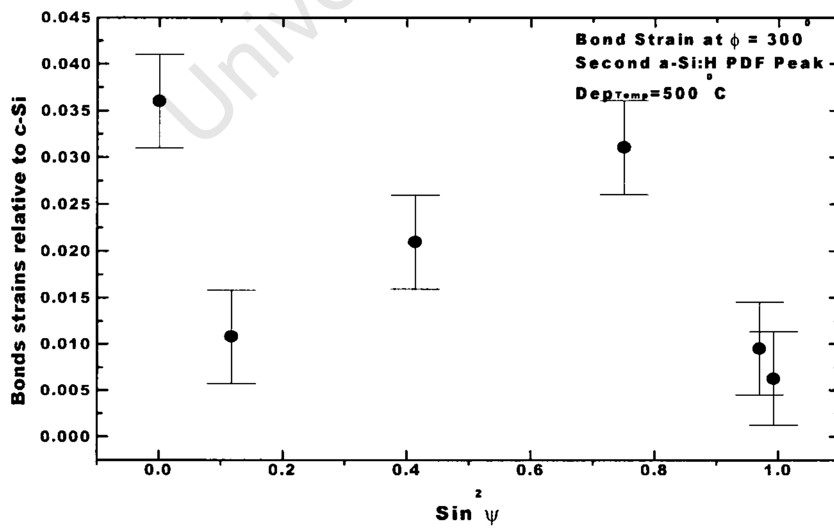

University of Cape Town

D) Information from the slope of $\varepsilon_{\varphi\psi}$ as function of of $sin^2\psi$ *for a*-Si:H layer for samples deposited at 300 °C and 500 °C from 2Θ diffraction peak position and PDF

Table -A: Information obtained from the slope in a-Si:H layer for samples deposited at 300 °C and 500 °C using direct diffraction peak shifts

Azimuth angle ϕ	Slope of $\varepsilon_{\varphi\psi}$ - $Sin^2\psi$ for sample deposited at 300°C	
	1st diffraction peak at (111)	2nd diffraction peak at (220)
0°	-0.0060 ± 0.0080	-0.0070 ± 0.0033
60°	-0.0263 ± 0.0319	-0.0038 ± 0.0070
120°	-0.0136 ± 0.0147	-0.0106 ± 0.0027
180°	-0.0175 ± 0.0123	-0.0111 ± 0.0049
240°	-0.0134 ± 0.0196	-0.0198 ± 0.0025
300°	-0.0058 ± 0.0280	-0.0132 ± 0.0056

Azimuth angle ϕ	Slope of $\varepsilon_{\varphi\psi}$ - $Sin^2\psi$ for sample deposited at 500°C	
	1st diffraction peak at (111)	2nd diffraction peak at (220)
0°	-0.0106 ± 0.0079	-0.0104 ± 0.0044
60°	-0.0155 ± 0.0084	-0.0074 ± 0.0045
120°	-0.0203 ± 0.0064	-0.0099 ± 0.0131
180°	-0.0219 ± 0.0119	-0.0147 ± 0.0058
240°	-0.0275 ± 0.0098	-0.0057 ± 0.0054
300°	-0.0238 ± 0.0078	-0.0012 ± 0.0022

Table -B: Information obtained from the slope in a-Si:H layer for samples deposited at 300 °C and 500 °C using direct PDF peak position

Azimuth angle ϕ	Slope of $\varepsilon_{\varphi\psi}$ - $Sin^2\psi$ from PDF for sample deposited at 300°C	
	1st PDF peak at (111)	2nd PDF peak at (220)
0°	0.0484 ±0.0215	-0.0002 ±0.0138
60°	0.0320 ± 0.0399	-0.0021 ± 0.0114
120°	0.0194 ±0.0489	0.0040 ± 0.0187
180°	0.0156 ±0.0264	-0.0059 ± 0.0147
240°	0.0288 ±0.0188	-0.0020 ±0.0199
300°	0.0041 ±0.0184	-0.0101 ±0.0180

Azimuth angle ϕ	Slope of $\varepsilon_{\varphi\psi}$ - $Sin^2\psi$ from PDF for sample deposited at 500°C	
	1st PDF peak at (111)	2nd PDF peak at (220)
0°	-0.0402 ±0.0274	-0.0014 ±0.0094
60°	-0.0399 ±0.0224	0.0005 ±0.0121
120°	-0.0367 ±0.0191	-0.011 ±0.0154
180°	-0.0463 ±0.0149	-0.0091 ±0.0162
240°	-0.0084 ±0.0059	-0.0178 ± 0.0177
300°	-0.0543 ±0.0219	-0.0144 ± 0.0124

University of Cape Town

University of Cape Town